ABSTRACT

Title of Dissertation: THE ULTRAFAST NONLINEAR RESPONSE OF AIR MOLECULES AND ITS EFFECT ON FEMTOSECOND LASER PLASMA FILAMENTS IN ATMOSPHERE

Yu-hsin Chen, Doctor of Philosophy, 2011

Directed by: Professor Howard M. Milchberg
Department of Electrical and Computer Engineering

The nonlinear propagation of an intense ultrafast laser pulse in atmosphere or other gas media leads to filamentation, a phenomenon useful for applications such as remote sensing, spectral broadening and shaping of ultrashort laser pulses, terahertz generation, and guiding of electrical discharges. Axially extended optical filaments result from the dynamic balance between nonlinear self-focusing in the gas and refraction from the free electron distribution generated by laser ionization.

In the air, self-focusing is caused by two nonlinear optical processes: (1) the nearly-instantaneous, electronic response owing to the distortion of electron orbitals, and (2) the delayed, orientational effect due to the torque applied by the laser field on the molecules with anisotropic polarizability. To study their roles in filamentary propagation as well as influences on plasma generation in atmosphere, these effects were experimentally examined by a sensitive, space- and time-resolved technique based on single-shot supercontinuum spectral interferometry (SSSI), which is capable of measuring ultrafast refractive index shift in the optical medium.

A proof-of-principle experiment was first performed in optical glass and argon gas, showing good agreement between the laser pulse shape and the refractive index temporal evolution owing to pure instantaneous n_2 effect. Then the delayed occurrence of the molecular alignment in the temporal vicinity of the femtosecond laser pulse, as well as the subsequent periodic "alignment revivals" due to the coherently excited rotational wavepacket were measured in various linear gas molecules, and the results agreed well with quantum perturbation theory. It was found that the magnitude of orientational response is much higher than the electronic response in N_2 and O_2, which implies that the molecular alignment is the dominant nonlinear effect in atmospheric propagation when the pulse duration is longer than $\sim$ 40 fs, the rotational response timescale of air molecules.

Realizing the possibility of manipulating plasma generation by aligning air molecules, the molecular orientational effect was further investigated by a technique developed to directly measure, for the first time, the radial and axial plasma density in a meter-long filament. The experiment was performed using both $\sim$ 40 fs and $\sim$ 120 fs laser pulse durations while keeping the peak power fixed under various focusing conditions, and the alignment-assisted filamenation with $\sim$ 2–3 times plasma density and much longer axial length was consistently observed with the longer pulse, which experienced larger refractive index shift and thus stronger self-focusing. Simulations reproduced the axial electron density measurements well for both long and short pulse durations, when using a peak magnitude of instantaneous response as $< 15\%$ of the rotational response.

THE ULTRAFAST NONLINEAR RESPONSE OF AIR MOLECULES AND ITS EFFECT ON FEMTOSECOND LASER PLASMA FILAMENTS IN ATMOSPHERE

by

Yu-hsin Chen

Dissertation submitted to the Faculty of the Graduate School of the
University of Maryland, College Park in partial fulfillment
of the requirements for the degree of
Doctor of Philosophy
2011

Advisory Committee:
Professor Howard M. Milchberg, Chair
Professor Thomas M. Antonsen
Professor Thomas E. Murphy
Professor Ki-Yong Kim
Professor Rajarshi Roy

Acknowledgments

I feel privileged that I can work with many brilliant people in such challenging and fascinating field. First of all I would like to thank my advisor, Prof. Howard Milchberg, for his mentorship and for providing a wonderful research environment. I have to express my gratitude to Sanjay Varma, who collaborated closely with me on many projects, in which overnight, exhausting, and seemingly endless running of experiments is usually involved. I also must thank Prof. Thomas Antonsen, for his help on performing simulations presented in this Dissertation.

I am grateful to Dr. Andrew York and Brian Layer, who have also been my colleagues for years. They love to share their interesting and brilliant ideas with me and are always supportive. I am indebted to Arman Fallahkhair and Yu-Hsiang Cheng, for their technical assistance on my experiments. I also have to acknowledge Jennifer Elle, Andrew Goers, Colin Kennedy, Hyun Kim, Eric Rosenthal, Dr. Jared Wahlstrand, and Sung Jun Yoon. It is a great pleasure to work with them.

Finally I would like to thank my parents, my sister, and especially my wife, Teresa. This work would not have been possible without their love and support, and I dedicate this Dissertation to them.

Table of Contents

List of Tables v

List of Figures vi

1 Introduction 1
- 1.1 Linear optics 2
- 1.2 Nonlinear optics 8
- 1.3 Second- and third-order nonlinearities 13
- 1.4 Resonant nonlinearities 16
- 1.5 Self- and cross-phase modulation 18
- 1.6 Self-focusing and filamentation 21
- 1.7 Plasma and laser-induced ionization 24
- 1.8 Nonlinear propagation 28
- 1.9 Outline of the Dissertation 29

2 Ultrafast measurement of transient refractive index shifts 31
- 2.1 Introduction 31
- 2.2 Single-shot supercontinuum spectral interferometry 35
- 2.3 Experimental setup 42
- 2.4 Results 46
- 2.5 Conclusion 52

3 Laser alignment of linear molecules 54
- 3.1 Introduction 54
- 3.2 Transient refractive index arises from molecular alignment 60
- 3.3 Quantum rigid rotor 63
- 3.4 Density matrix formalism 64
- 3.5 Partition function and consideration of symmetry 69
- 3.6 Perturbation theory 73
- 3.7 Discussion 78

4 Measurement of rotational wave packet revivals of linear gas molecules 86
- 4.1 Introduction 86
- 4.2 Experimental setup and noise reduction technique 89
- 4.3 Rotational inertia effect: delayed initial alignment by the laser field 92
- 4.4 Quantum echoes of refractive index due to rephasing of the rotational wave packet 97
- 4.5 Conclusion 111

5 Direct measurement of the electron density of femtosecond laser pulse-induced filament in air 112
- 5.1 Introduction 112
- 5.2 Experimental setup 117

5.3 Results 122
5.4 Simulation 131
5.5 Conclusion 135

6 Conclusions and future directions 136
6.1 Optical nonlinearities of linear gas molecules 136
6.2 Laser filamentation in atmosphere 137

A List of publications by the Candidate 139

Bibliography 140

List of Tables

3.1 Selected linear molecular parameters $\Delta\alpha$ and rotational constant B from Ref. [109]. T_{rev} is calculated from $(2cB)^{-1}$. 85

List of Figures

1.1 Energy level diagrams of (a) Stokes, and (b) anti-Stokes Raman scattering. 17

1.2 Energy level diagram showing some $j \to j \pm 2$ transitions in the rotational Raman process. 17

1.3 (a) The time-dependent frequency sweep $\Delta\omega(t)$ (top panel) experienced by a Gaussian laser pulse $I(t)$ with $1/e$ full width 2τ (bottom panel) during self-phase modulation. (b) The spectrum of a transform-limited Gaussian laser pulse with 100 fs full-width-at-half-maximum (FWHM) duration. (c) A calculated self-phase-modulated spectrum, using (b) as the input and assuming the nonlinear medium is dispersionless. 20

1.4 Schematic of laser filamentation. 23

1.5 (a) Tunneling ionization, and (b) multiphoton ionization. 27

2.1 Schematics of spectral interferometry, after Ref. [72]. 37

2.2 Experimental setup. BS1: beamsplitter, XGC: xenon gas cell, MI: Michelson interferometer, P: 500 μm pinhole, SF4: 2.5-cm thick SF4 glass as dispersive material, HWP: half waveplate, M: zero degree Ti:Sapphire dielectric mirror, BS2: beamsplitter for combining pump and SC pulses. The pump beam energy can be tuned by another set of half waveplate and polarizer, which is not shown in this figure. . . 43

2.3 Spectral interferograms showing laser-induced, wavelength-dependent fringe shift in argon at (a) 7.8 atm and $I_{\text{peak}} = 4.1 \times 10^{13}$ W/cm^2 and (b) 4.4 atm and $I_{\text{peak}} = 7.7 \times 10^{13}$ W/cm^2, where plasma is observed as a long tail extending to the short wavelength edge on the interferogram. Note that the SC probe and reference pulses are positively chirped, thus a shorter wavelength on the interferogram means a later time. The 1D space and time variations of the effective argon nonlinear refractive index change Δn extracted from (a) and (b) are shown in (c) and (d), respectively. The positive index shift is due to instantaneous electronic nonlinearity, which follows the pump pulse temporal profile. The plasma-induced negative index shift is seen in (d) following the pump pulse. The baseline noise in extracted $\Delta n(x,t)$ plots is determined by the CCD camera pixel size, which sets the minimum resolvable fringe shift in (a) and (b). 47

2.4 250 shot average (solid line) and a single shot trace (circles) of refractive index transient $\Delta n(x=0,t)$ (and extracted phase $\Delta\Phi(x=0,t)$) along the beam axis for 6.4 atm nitrogen. The results agree well, confirming good shot-to-shot stability. The pump energy was 60 μJ, corresponding to $I_{\text{peak}} = 4.1 \times 10^{13}$ W/cm^2, below the threshold for nitrogen ionization. 49

2.5 (a) A sample single-shot spectral interferogram taken in 5.1 atm N_2O with 1.4×10^{13} W/cm^2 pump intensity. (b) Averaged spectral interferogram image over 300 laser shots, taken in the same condition as (a). The close resemblance between single-shot and multi-shot-averaged spectra indicates good stability in SC generation. 50
2.6 Induced nonlinear refractive index shift $\Delta n(x,t)$ from a 200 μm-thick BK7 window with 5 μJ pump pulse energy and 3.4×10^{12} W/cm^2 peak intensity. The inset is the probe phase shift $\Delta\Phi(x=0,t)$ with corresponding $\Delta n(x=0,t)$ (solid line). The temporal phase evolution profile from 7.8 atm argon (Fig. 2.3(a)), normalized to the same peak phase value, is shown here for comparison (circles). 51
2.7 Measured nonlinear refractive index shift $\Delta n(x,t)$ in Ar, N_2, and N_2O. For the linear molecules N_2 and N_2O, part of the nonlinearity is contributed by the inertia of molecular rotation, which causes a delayed response which does not follow the pump pulse shape. 52

3.1 (a) The classical "dumbbell" model of a diatomic molecule having anisotropic polarizabilities $\alpha_\parallel$ and $\alpha_\perp$, with molecule-fixed and space-fixed coordinates labelled. (b) A linearly-polarized electric field induces a net dipole moment which is generally not in the same direction as the field. The molecule then experiences a torque from the electric field and tends to line up along the field direction. 56
3.2 Calculated molecular alignment at $T = 300$ K excited by a delta-function laser pulse with 1 J/cm^2 fluence and successive quarter-, half-, and full-revivals in (a) N_2 and (c) O_2. The full-revival periods are $T_{\mathrm{rev,N_2}} = 8.33$ ps for N_2 and $T_{\mathrm{rev,O_2}} = 11.59$ ps for O_2, respectively. Panels (b) and (d) are details of (a) and (c) from 0 to 800 fs. 81
3.3 Thermal populations of the rotational states $\rho_j = (2j+1)\rho_j^m$ at $T =$ 300 K in (a) N_2 and (b) O_2, with corresponding ρ_j^m shown in the insets, and calculated spectral amplitudes for each $\omega_{j,j-2}$ contributing to the molecular alignment in (c) N_2 and (d) O_2, excited by the same 1 J/cm^2 delta-function pulse as in Fig. 3.2. 84

4.1 Experimental setup. HWP: half waveplate, BS: beamsplitter for combining pump and SC pulses, M: zero degree Ti:Sapphire dielectric mirror. The inset shows interferograms in 3 temporal windows, corresponding to laser field alignment (0 ps), quarter revival ($\sim$ 3 ps), and half revival ($\sim$ 6 ps) of the rotational wavepacket in 5.1 atm O_2. 90
4.2 Sample interferogram images (a) from a single laser shot, and (b) after averaging over 300 shots. 91

4.3 Normalized transient shift of refractive index Δn from measurements (open circles) and calculations (solid line) for (a) N_2 and (b) N_2O. For comparison, a Gaussian function centered at $t = 0$ with 110 fs FWHM duration is shown on each figure (dashed line) to represent the pump pulse envelope. Un-normalized Δn traces of (a) and (b), along with instantaneous electronic nonlinear response in Ar, are shown in (c), under the experiment conditions of 110 fs pump pulse duration with 95 μJ (6.7×10^{13} W/cm^2), 60 μJ (4.2×10^{13} W/cm^2), and 20 μJ (1.4×10^{13} W/cm^2) pulse energy (peak intensity), in 4.4 atm Ar, N_2, and N_2O, respectively. 95

4.4 Measured N_2 alignment up to $t = 1.25\ T_{\text{rev}}$ for 6.4 atm gas pressure and 4.1×10^{13} W/cm^2 pump peak intensity: (a) probe beam central lineout, and (b) corresponding 2-D space- and time-resolved image across the probe beam. Calculated alignment is shown in (c), assuming two different excitation pulse shapes: delta function (dashed curve) and $\cos^2$ function with 110 fs FWHM (solid curve). For N_2, $T_{\text{rev}} = 8.3$ ps, and the collisional dephasing of wavepacket is not included in this calculation. 98

4.5 Measured O_2 alignment up to $t = 1.25\ T_{\text{rev}}$, where $T_{\text{rev}} = 11.6$ ps for O_2, for 5.1 atm gas pressure and 2.7×10^{13} W/cm^2 pump peak intensity: (a) probe beam central lineout, and (b) corresponding 2-D space- and time-resolved image across the probe beam. The dephasing time constant $1/\gamma = 23.2$ ps was obtained by fitting the peak amplitudes of (a) to an exponential. Calculated alignment is shown in (c), including dephasing by using the extracted value of γ, and assuming two different excitation pulse shapes: delta function (dashed curve) and $\cos^2$ function with 110 fs FWHM (solid curve). 100

4.6 Measured N_2O alignment up to $t = T_{\text{rev}}$, where $T_{\text{rev}} = 40.5$ ps for N_2O, for 2.4 atm gas pressure and 1.4×10^{13} W/cm^2 pump peak intensity: (a) probe beam central lineout, and (b) corresponding 2-D space- and time-resolved image across the probe beam. Note that the 1/4 and 3/4 revivals are not present due to the axial asymmetry of the N_2O molecule. The dephasing time constant $1/\gamma = 23.8$ ps was obtained by fitting the peak amplitudes of (a) to an exponential. Calculated alignment is shown in (c), using the extracted dephasing rate γ and assuming two different excitation pulse shapes: delta function (dashed curve) and $\cos^2$ function with 110 fs FWHM (solid curve). . . 102

4.7 (a) Pump beam center lineout and (b) corresponding x-t perspective plot of measured D_2 molecule alignment recurrences excited by 65 μJ pump energy (4.4×10^{13} W/cm^2 peak intensity), with 7.8 atm gas pressure. (c) Fourier transform of the signal representing rotational wavepacket revivals after the pump pulse in (a). The peak frequency is identified as $\omega_{2,0} \sim 3.4 \times 10^{13}$ s^{-1}, giving the rotational constant $B_{\mathrm{D}_2} = 30.4$ cm^{-1}. (d) Calculated alignment with delta function (dashed curve) and 110 fs cos^2 function (solid curve), using B_{D_2} obtained in (c). 104

4.8 (a) Thermal rotational population ρ_j and ρ_j^m, and (b) calculated amplitude of frequency components $\omega_{j,j-2}$ contributing to molecular alignment of D_2 at $T = 300$ K. The pump pulse shapes are assumed to be delta function and Gaussian, with fluence (peak intensity) matching the experimental parameters used in Fig. 4.7. 105

4.9 (a) Pump beam center lineout and (b) corresponding x-t perspective plot of H_2 alignment recurrences, measured in the same experiment conditions as in Fig. 4.7. (c) $\omega_{2,0} \sim 7 \times 10^{13}$ s^{-1} is observed by Fourier transformation of recurrence signal (neglecting the first peak) in (a), which gives the rotational constant $B_{\mathrm{H}_2} = 61.8$ cm^{-1}. (d) Calculated alignment with delta function (dashed line) and 110-fs cos^2 function (solid line), with rotational constant given from (c). The calculated cos^2 pulse response is shown again in (e), with proper scaling revealing the small wiggles of revivals. 107

4.10 (a) Thermal rotational population ρ_j and ρ_j^m, and (b) calculated amplitude of frequency components $\omega_{j,j-2}$ contributing to molecular alignment of H_2 at $T = 300$ K. The pump pulse shapes are assumed to be delta function and Gaussian, with fluence (peak intensity) matching the experimental parameters used in Fig. 4.9. 108

4.11 Transient refractive indices of 5.1 atm O_2 near 3/4-revival of the rotational wavepacket for the pump polarization parallel (solid curve) and perpendicular (dashed curve) to the probe beam. The pump pulse energy and peak intensity is 40 μJ and 2.7×10^{13} W/cm^2. . . . 110

4.12 (a) Measured 1/2-revivals of N_2O alignment at pressures of 2.4, 3.7, 5.1, and 6.4 atm, normalized to the peak alignment amplitude near $t = 0$. (b) Dephasing rate γ versus N_2O pressure (squares) with a linear fit (solid line). The dephasing rate per unit pressure is 1.46×10^{10} s^{-1} atm^{-1}. The laser pulse energy is 20 μJ, corresponding to 1.4×10^{13} W/cm^2 peak intensity. 110

5.1 A simplified pictorial illustration of the moving-focus model, after Ref. [130]. 115

5.2 (a) Measured nitrogen fluorescence originates from a long-range femtosecond laser filament in air (from Ref. [129]), (b) the transverse beam profiles near the end of the filament in air at various laser pulse energies (peak powers), showing the onset of the filament core when $P > P_{\mathrm{cr}} \sim 10$ GW, with the surrounding background reservoir (from Ref. [112]). 116

5.3 Experimental interferometry setup, showing imaging lenses (L) and the microscope objective (O). The inset shows the filament width d and probe crossing angle θ. 119

5.4 (a) A sample interferogram of a single filament, and (b) the retrieved phase. 121

5.5 (a) Spatial sequence of bow-tie phase images showing filament collapse, for a 2.85 mJ, 72 fs pulse focused at $f_{\#} = 345$. The frames show a sequence of 1-cm-spaced axial positions of the interferometer object plane, (i) $z = -39$ cm through (vi) $z = -34$ cm, (b) two filaments are generated and recorded at the same time, showing the capability of spatially-resolved measurement. 124

5.6 On-axis plasma density decay (squares) in a filament at the axial distance $z = -3.5$ cm to the focus, for pulse duration $\tau = 40$ fs, peak power $P = 19$ GW, lens focal length $f = 95$ cm, and $f_{\#} = 240$. An exponential decay time constant 244 ps is obtained by fitting the measured density vs probe delay (solid curve). 125

5.7 200-shot-averaged radial electron density profiles vs axial distance for (a) lens focal length $f = 95$ cm, $f_{\#} = 240$, laser peak power $P = 17$ GW, $\tau_{\mathrm{long}} = 120$ fs (upper panel), and $\tau_{\mathrm{short}} = 40$ fs (lower panel) and (b) $f = 306$ cm, $f_{\#} = 505$, $P = 19$ GW, $\tau_{\mathrm{long}} = 132$ fs (upper panel), and $\tau_{\mathrm{short}} = 44$ fs (lower panel). 127

5.8 On-axis electron density and filament FWHM vs axial distance acquired from Fig. 5.7, for (a) lens focal length $f = 95$ cm, $f_{\#} = 240$, laser peak power $P = 17$ GW, $\tau_{\mathrm{short}} = 40$ fs (red circles), and $\tau_{\mathrm{long}} = 120$ fs (black squares) and (b) $f = 306$ cm, $f_{\#} = 505$, $P = 19$ GW, $\tau_{\mathrm{short}} = 44$ fs (red circles), and $\tau_{\mathrm{long}} = 132$ fs (black squares). Each point is a 200-shot average. The inset in (b) shows a sample electron density profile from $z = -75$ cm. Peak values shown have $\sim 20\%$ uncertainty near the collapse point and $\sim 10\%$ over the rest of the filament. 129

5.9 On-axis filament spectra corresponding to the conditions of Fig. 5.8, with (i) $f_{\#} = 240$ and (ii) $f_{\#} = 505$. Also shown are the input spectra. The insets in (ii) show the filament spots on a far field screen for τ_{short} and τ_{long}. 130

5.10 Simulation results for the conditions of Fig. 5.8 (solid lines). Additional runs have been performed at 20% higher power (dashed lines). Red, short pulse; black, long pulse. 133

Chapter 1

Introduction

Filamentation is a nonlinear optical phenomenon in which the self-focusing of an intense laser pulse is dynamically balanced by optical ionization and plasma refraction when propagating in the medium, resulting in a transversely confined (~ 100 μm), weakly ionized channel which can be maintained over a long propagation range. Filamentary propagation in gases, especially in atmosphere, is of great interest due to the capability of the long-range, high-intensity ($\sim 10^{13}$ W/cm^2) delivery of optical energies, which has many potential applications such as remote sensing, spectral broadening and shaping of ultrashort laser pulses, terahertz generation, and guiding of electrical discharges.

In the monatomic gas, self-focusing is caused by the nearly-instantaneous, electronic nonlinear optical response. For linear gas molecules such as N_2 and O_2, an extra component of optical nonlinearity due to the delayed orientational effect of the molecules, or rotational Raman process, is also present. Previous studies have shown that the latter may affect the filamentary propagation of the femtosecond laser pulse in air. However, due to the fact that there are no reliable and conclusive measurements to (1) determine the magnitude and temporal evolution of refractive index shift contributed by both instantaneous and delayed nonlinearity, and (2) resolve the electron density radially and axially in the extended laser filament, the molecular orientational effect on atmospheric filamentation is yet systematically and quantitatively studied.

This Dissertation will address to these two issues and allow better understanding of the physics in laser filamentation. Furthermore, the investigation on the molecular alignment-assisted filamentation suggests a new way to control the filamentary propagation as well as the plasma generation in atmosphere.

1.1 Linear optics

The interaction between electromagnetic fields and matter is governed by the macroscopic Maxwell equations:

$$\nabla \cdot \mathbf{D} = 4\pi\rho, \tag{1.1a}$$

$$\nabla \cdot \mathbf{B} = 0, \tag{1.1b}$$

$$\nabla \times \mathbf{E} = -\frac{1}{c}\frac{\partial \mathbf{B}}{\partial t}, \tag{1.1c}$$

$$\nabla \times \mathbf{H} = \frac{1}{c}\frac{\partial \mathbf{D}}{\partial t} + \frac{4\pi}{c}\mathbf{j}, \tag{1.1d}$$

as well as the Lorentz force:

$$\mathbf{F} = q\left(\mathbf{E} + \frac{\mathbf{v}}{c} \times \mathbf{B}\right), \tag{1.2}$$

with $\mathbf{D} = \mathbf{E} + 4\pi\mathbf{P}$ and $\mathbf{B} = \mathbf{H} + 4\pi\mathbf{M}$, where $\mathbf{P}$ and $\mathbf{M}$ are electric polarization and magnetization, and where ρ and $\mathbf{j}$ refer to the free charge and current densities, respectively. For dielectric materials without field ionization there are no free electrons, therefore the source terms ρ and $\mathbf{j}$ can be omitted. For the static field, if the amplitude is weak compared with the material atomic (bound) electron field strength, there is a linear relationship between $\mathbf{P}$ and $\mathbf{E}$ expressed as $\mathbf{P} = \chi\mathbf{E}$ with $\epsilon = 1 + 4\pi\chi$ so that $\mathbf{D} = \epsilon\mathbf{E}$, where we assume here isotropic material response. Also we assume non-magnetic material so that $\mathbf{M} = 0$ and $\mathbf{B} = \mathbf{H}$.

The material response to the time-varying electromagnetic field becomes frequency dependent. From the microscopic point of view the electric polarization comes from the displacement of bound electrons of the atoms under the influence of the external field. The Lorentz-Drude model treats the atom as a classical harmonic oscillator, in which a single orbiting electron and the nucleus are attached to each end of a spring satisfying Hooke's law. The impinging electromagnetic wave serves as the driving source, which gives

$$m_e\left(\ddot{\mathbf{x}} + \Gamma\dot{\mathbf{x}} + \Omega^2\mathbf{x}\right) = -e\mathbf{E}(t), \tag{1.3}$$

where $\mathbf{x}$ is the electron displacement vector, m_e is the mass of the electron, Γ is the phenomenological damping constant, and Ω is the resonant frequency given by the "spring constant" $m_e\Omega^2$. The nucleus can be considered stationary because it is much heavier than the electron, and the effect of magnetic field can be ignored when $|\dot{\mathbf{x}}/c| \ll 1$, which is the case when the laser strength parameter (amplitude of normalized vector potential) $a_0 \ll 1$, where

$$a_0 = \sqrt{\frac{2e^2\lambda^2 I}{\pi m_e^2 c^5}} \tag{1.4}$$

for linear polarization, or intensity $I \ll 2.2\times 10^{18}$ W/cm^2 at the wavelength $\lambda = 800$ nm. Assuming the incident wave is monochromatic at frequency ω in the complex time-harmonic field (phasor) notation $\mathbf{E}(t) = \widetilde{\mathbf{E}}_\omega e^{-i\omega t}$, also assuming there are Z electrons per atom with f_j electrons having resonant frequency Ω_j and damping constant Γ_j, the steady-state solution of Eq. 1.3 gives the complex linear atomic polarizability $\alpha(\omega)$ as well as susceptibility $\chi(\omega) \equiv N\alpha(\omega)$ in the gas atoms:

$$\mathrm{Re}\,(\chi(\omega)) = \frac{Ne^2}{m_e}\sum_j f_j \frac{\Omega_j^2 - \omega^2}{\left(\Omega_j^2 - \omega^2\right)^2 + \Gamma_j^2\omega^2}, \tag{1.5a}$$

$$\mathrm{Im}\,(\chi(\omega)) = \frac{Ne^2}{m_e}\sum_j f_j \frac{\Gamma_j\omega}{\left(\Omega_j^2 - \omega^2\right)^2 + \Gamma_j^2\omega^2}, \tag{1.5b}$$

with $\widetilde{\mathbf{P}}_\omega = \chi(\omega)\widetilde{\mathbf{E}}_\omega$, where N is the number density of the atoms, f_j is the classical oscillator strength with $\sum_j f_j = Z$. This can be generalized to polychromatic waves, giving $\widetilde{\mathbf{P}}(\omega) = \chi(\omega)\widetilde{\mathbf{E}}(\omega)$, where $\widetilde{\mathbf{P}}(\omega)$ and $\widetilde{\mathbf{E}}(\omega)$ are Fourier transforms of $\mathbf{P}(t)$ and $\mathbf{E}(t)$, respectively. Note that in the solid the induced atomic dipole moment can interact with the nearby atoms, therefore the correction $\chi = N\alpha/(1 - 4\pi N\alpha/3)$ must be made [1]. Also note that the quantum mechanical derivation gives almost the same result as Eq. 1.5, except that a different definition of f_j (quantum oscillator strength) is employed, and that Ω_j is defined by the photon energy $\hbar\Omega_j$ involved in the transition between two energy levels, assuming the external field is very weak so that the electron orbitals are not distorted [2].

The time domain representation of the linear polarization is

$$\mathbf{P}(t) = \int_{-\infty}^{\infty} d\tau R(\tau)\mathbf{E}(t-\tau), \tag{1.6}$$

where the Fourier transform of $R(t)$ gives $\chi(\omega)$. Simplification can be made at the adiabatic limit, i.e., the incident field envelope varies much slower than the response of the bound electron. In fused silica (SiO_2), for example, the UV absorption edge is at $\lambda_{\text{abs}} \sim 150$ nm [3], and the electron response timescale τ to optical frequencies can be estimated by $2\pi/\Omega_{\text{abs}} = \lambda_{\text{abs}}/c \sim 0.5$ fs. In the adiabatic limit, the incident wave usually satisfies two criteria: (1) all of the constituent frequency components are far away from any resonant frequency Ω_j, and (2) the bandwidth is narrow. The slowly varying envelope approximation (SVEA) now can be used for time-domain representation of the electric field

$$\mathbf{E}(t) = \frac{1}{2}\left[\mathbf{E}_{\omega_0}(t)e^{-i\omega_0 t} + \text{c.c.}\right], \tag{1.7}$$

where ω_0 is the carrier frequency, and $E_{\omega_0}(t)$ is the envelope with the bandwidth $\Delta\omega \ll \omega_0$. If ω_0 is far away from any Ω_j, $\text{Im}(\chi(\omega)) \approx 0$ and $\chi(\omega) \approx \text{Re}(\chi(\omega))$, so there is nearly no absorption. Also in the range of $\omega_0 \pm \Delta\omega_0$ the variation of $\chi(\omega)$ is negligible, which validates the quasi-monochromatic approximation

$$\mathbf{P}(t) = \chi(\omega_0)\mathbf{E}(t). \tag{1.8}$$

A more quantitative criterion to determine the adiabatic limit is given by [2]

$$\left| \frac{\frac{d}{d\omega}\chi(\omega)\big|_{\omega_0}}{\chi(\omega_0)} \frac{\frac{d}{dt}E(t)}{E(t)} \right| \ll 1. \tag{1.9}$$

Now we examine the solutions of the Maxwell equations leading to the propagating electromagnetic wave. For the uniform, isotropic, and linear medium without free charge or current, a wave equation can be obtained from Eq. 1.1c and Eq. 1.1d, assuming $\mathbf{M} = 0$:

$$\nabla^2 \mathbf{E} - \frac{1}{c^2} \frac{\partial^2 \mathbf{E}}{\partial t^2} = \frac{4\pi}{c^2} \frac{\partial^2 \mathbf{P}}{\partial t^2}, \tag{1.10}$$

and the simplest solution is the monochromatic plane wave $E_{\omega_0} \cos(k_0 z - \omega_0 t)$, where ω_0 is the frequency, $k_0 = n_0 \omega_0 / c$ is the wavenumber in the medium, $n_0 = \sqrt{\epsilon(\omega_0)}$ is the index of refraction, and for monochromatic solutions it is legitimate to use Eq. 1.8. The propagation speed of a monochromatic wave at the frequency ω_0 is determined by the phase velocity $v_p = \omega_0 / k_0 = c/n_0$.

However the plane wave solution is not realistic because it transversely extends to infinity with non-vanishing amplitude. Instead, in many occasions it is preferable to use the Gaussian beam solution $E(r, z, t) = E_{\omega_0}(r, z) e^{-i\omega_0 t}$ obtained from the paraxial approximation of Eq. 1.10, with

$$E_{\omega_0}(r, z) = \frac{E_0}{w(z)} \exp\left(-\frac{r^2}{w^2(z)}\right) \exp\left(i \frac{k_0 r^2}{2R(z)}\right) \exp\left(i\left[k_0 z - \phi(z)\right]\right), \tag{1.11}$$

where

$$w(z) = w_0^2 \left(1 + \left(\frac{\lambda_0 z}{n_0 \pi w_0^2}\right)^2\right), \tag{1.12}$$

$$\frac{1}{R(z)} = \frac{z}{z^2 + \left(n_0 \pi w_0^2/\lambda_0\right)^2}, \tag{1.13}$$

$$\tan\phi(z) = \frac{z}{n_0 \pi w_0^2/\lambda_0}, \tag{1.14}$$

and $\lambda_0 = 2\pi c/\omega_0$ is the vacuum wavelength. The Rayleigh range $z_\mathrm{R} = n_0 \pi w_0^2/\lambda_0$ is defined so that when $z = z_\mathrm{R}$, the beam radius $w = \sqrt{2} w_0$. For the quasi-monochromatic solutions we can replace E_{ω_0} by $E_{\omega_0}(t)$ for the plane wave and $E_{\omega_0}(r, z)$ by $E_{\omega_0}(r, z, t)$ for the Gaussian wave, assuming the condition of Eq. 1.9 is met.

For a multi-coloured wave, such as a femtosecond laser pulse, propagating in a medium where Eq. 1.9 is no longer valid, i.e., the dispersion is not negligible, each frequency component experiences different $\epsilon(\omega)$ and thus has different v_p, therefore it is useful to define the group velocity

$$v_g = \left(\frac{dk(\omega)}{d\omega}\right)^{-1}, \tag{1.15}$$

which is the propagation speed of the envelope (overall shape) of the field in the medium. Assume that the propagating wave is in the form

$$E(\mathbf{r}, t) = \frac{1}{2}\left(E_0(\mathbf{r}, t) e^{i(k_0 z - \omega_0 t)} + \text{c.c.}\right) \tag{1.16}$$

under the slowly-varying envelope approximation, where $\omega_0 \ll \Delta\omega$ and $k_0 = k(\omega_0) =$

$n_0\omega_0/c$. By expanding the dispersion relation $k(\omega)$ around the carrier frequency ω_0, $k(\omega) = k(\omega_0) + (\omega - \omega_0)(dk/d\omega)|_{\omega_0} + \frac{1}{2}(\omega - \omega_0)^2(d^2k/d\omega^2)|_{\omega_0} + \cdots$, and keeping the terms up to the second order, from Eq. 1.10 one may obtain the paraxial wave equation for the envelope in the linear medium:

$$\frac{1}{2ik_0}\nabla_\perp^2 E_0 + \frac{\partial E_0}{\partial z} + \left(\frac{dk}{d\omega}\right)\bigg|_{\omega_0}\frac{\partial E_0}{\partial t} + \frac{i}{2}\left(\frac{d^2k}{d\omega^2}\right)\bigg|_{\omega_0}\frac{\partial^2 E_0}{\partial t^2} = 0, \tag{1.17}$$

where $(dk/d\omega)|_{\omega_0} = [v_g(\omega_0)]^{-1}$, and $(d^2k/d\omega^2)|_{\omega_0}$ is the group velocity dispersion (GVD). Equation 1.17 takes account of the distortion of the wave envelope when propagating in the dispersive medium with nonzero GVD. Higher order dispersion terms such as $d^3k/d\omega^3$, $d^4k/d\omega^4$,... can be also incorporated into Eq. 1.17 when dealing with highly dispersive media.

1.2 Nonlinear optics

Equation 1.3 assumes a parabolic potential, which is equivalent to a linear restoring force, experienced by the bound electron. It is only true when the amplitude of the electron oscillation is small compared with the Bohr radius of the atom in the external time-varying field. Under the strong driving field the spring force will develop nonlinear corrections, leading to

$$m_e\left(\ddot{\mathbf{x}} + \Gamma\dot{\mathbf{x}} + \Omega^2\mathbf{x} + \mathbf{f}_{\mathrm{NL}}(\mathbf{x})\right) = -e\mathbf{E}(t), \tag{1.18}$$

where $\mathbf{f}_{\mathrm{NL}}(\mathbf{x})$ is the nonlinear restoring force, and the solution gives the nonlinear polarization per electron (dipole moment) $\mathbf{p}_e(t) = -e\mathbf{x}(t)$. If $|\mathbf{f}_{\mathrm{NL}}(\mathbf{x})| \ll |\Omega^2\mathbf{x}|$, one can use the series expansion $f_{\mathrm{NL}}(x) = a_2x^2 + a_3x^3 + a_4x^4 + \cdots$ and use perturbation methods to solve Eq. 1.18. Consider the case that the only nonzero expansion coefficient is a_2, and assume $x = x^{(1)} + x^{(2)}$ where $x^{(1)}$ is the linear solution of Eq. 1.3 and $x^{(2)}$ is the next order correction when the nonlinear force term a_2x^2 is present. It can then be shown that [4]

$$\ddot{x}^{(2)} + \Gamma\dot{x}^{(2)} + \Omega^2x^{(2)} + a_2\left(x^{(1)}\right)^2 = 0. \tag{1.19}$$

If the driving field is composed of two frequencies ω_1 and ω_2:

$$E(t) = \frac{1}{2}\left[E_{\omega_1}e^{-i\omega_1 t} + E_{\omega_2}e^{-i\omega_2 t} + \text{c.c.}\right], \tag{1.20}$$

then the second-order nonlinear polarization $P^{(2)} = -Nex^{(2)}$ has frequency components (i) $|\omega_1 \pm \omega_2|$, (ii) $2\omega_1$ and $2\omega_2$, and (iii) $\omega_1 - \omega_1 = \omega_2 - \omega_2 = 0$. Similarly, if $f_{\mathrm{NL}} = a^3x^3$ and the driving wave has three colors ω_1, ω_2, and ω_3, then one can get the third-order nonlinear polarization $P^{(3)}$ with frequencies ω_1, ω_2, ω_3, and the combinations $\omega = |\pm n_1\omega_1 \pm n_2\omega_2 \pm n_3\omega_3|$, where integers $n_1, n_2, n_3 \geq 0$ and $n_1 + n_2 + n_3 = 3$.

The quantum mechanical derivation of induced polarization starts from formulating the total Hamiltonian operator $H = H_0 + h_E + H_R$, where H_0 is the atomic Hamiltonian, $h_E(t) = e\mathbf{E}(t) \cdot \mathbf{r}$ is the potential of the electric dipole moment, and

H_R is the relaxation processes causing energy loss. The next step is to solve the equation

$$\frac{d\rho}{dt} = -\frac{i}{h}\left[H, \rho\right], \tag{1.21}$$

where [ ] denotes the commutator, and ρ is the density operator

$$\rho = \sum_q P_q \left|\Psi_q\right\rangle \left\langle\Psi_q\right|, \tag{1.22}$$

where P_q is the classical probability for finding a specific state labeled by q:

$$\left|\Psi_q\right\rangle = \sum_k a_{q,k} \left|k\right\rangle, \tag{1.23}$$

in an ensemble of identical atoms with $\sum_q P_q = 1$, and $|k\rangle$ is the eigenstate of the electron orbitals. Finally the averaged atomic polarization is $\mathbf{p}(t) = -e \cdot \mathrm{Tr}(\rho\mathbf{r})$ where Tr denotes the trace operation. The method outlined above is the most general approach, which can be used for the highly nonlinear electronic response when h_E is comparable with H_0.

If $h_E \ll H_0$ then the quantum perturbation theory can be employed. The density operator can be expanded in a series of smaller and smaller corrections $\rho(t) = \rho^{(0)} + \rho^{(1)}(t) + \rho^{(2)}(t) + \cdots$, where $\rho^{(0)}$ is the unperturbed density matrix at thermal equilibrium, and $\rho^{(n)}$ denote the successive corrections. It can then be shown that the temporal evolution of $\rho^{(n)}$ is [2]

$$i\hbar\frac{d}{dt}\rho^{(n)}(t) = \left[H_0, \rho^{(n)}(t)\right] + \left[h_E(t), \rho^{(n-1)}(t)\right], \tag{1.24}$$

with the solution

$$\begin{aligned}\rho^{(n)}(t) = \left(\frac{-i}{\hbar}\right)^n U_0(t) \int_{-\infty}^{t} d\tau_1 \int_{-\infty}^{t_1} d\tau_2 \cdots \int_{-\infty}^{t_{n-1}} d\tau_n \\ \times \left[h'_E(\tau_1), \left[h'_E(\tau_2), \cdots \left[h'_E(\tau_n), \rho^{(0)}\right] \cdots\right]\right] U_0(-t),\end{aligned} \tag{1.25}$$

where $U_0(t) = \exp(-iH_0t/\hbar)$, and $h'_E(t) = U_0(-t)h_E(t)U_0(t)$. The relaxation process H_R is not included in Eq. 1.24 and Eq. 1.25, and it can be introduced using the model

$$\left(\frac{d}{dt}\rho_{ij}\right)_R = -\gamma_{ij}\left(\rho - \rho^{(0)}\right)_{ij}, \tag{1.26}$$

where i, j are the indices labeling the matrix element. Equation 1.26 means exponential decay of a state i when $i = j$, and it means dephasing between states i and j when $i \neq j$.

Note that Eq. 1.25 can be interpreted as expressing that there are 1, 2,..., n photons with energies $\hbar\omega_1$, $\hbar\omega_2$,..., $\hbar\omega_n$ involved in the processes $\rho^{(1)}$, $\rho^{(2)}$,..., $\rho^{(n)}$, corresponding to the linear susceptibility $\chi^{(1)}$ (i.e., χ in Sec. 1.1), and nonlinear susceptibilities $\chi^{(2)}$, $\chi^{(3)}$,..., $\chi^{(n)}$, respectively. Also note that the nonlinear susceptibilities are tensors, because the medium is no longer isotropic under the influence of the intense polarized field. For example, assuming the electric field is in the form of Eq. 1.20 with $\omega_1 > \omega_2$, the nonlinear polarization representing sum- and difference-frequency generation has the form

$$\left(P^{(2)}_{\omega_1+\omega_2}\right)_\mu = \sum_{\alpha,\beta} K(\omega_1+\omega_2)\chi^{(2)}_{\mu\alpha\beta}(\omega_1+\omega_2)\left(E_{\omega_1}\right)_\alpha \left(E_{\omega_2}\right)_\beta\,, \tag{1.27a}$$

$$\left(P^{(2)}_{\omega_1-\omega_2}\right)_\mu = \sum_{\alpha,\beta} K(\omega_1-\omega_2)\chi^{(2)}_{\mu\alpha\beta}(\omega_1-\omega_2)\left(E_{\omega_1}\right)_\alpha \left(E^*_{\omega_2}\right)_\beta\,, \tag{1.27b}$$

where K is the permutation factor, and $\mu, \alpha, \beta \in \{1, 2, 3\}$ are indices of the spatial coordinates.

Similar to Sec. 1.1, for quasi-monochromatic waves it is possible to find a time-domain representation of nonlinear polarization, under the adiabatic limit:

$$\begin{aligned}(P^{(n)}_{\omega_\sigma}(t))_\mu = \sum_\alpha \sum_\omega & K(-\omega_\sigma;\omega_1,\ldots,\omega_n)\chi^{(n)}_{\mu\alpha_1\ldots\alpha_n}(-\omega_\sigma;\omega_1,\ldots,\omega_n) \\ & \times (E_{\omega_1}(t))_{\alpha_1}\ldots(E_{\omega_n}(t))_{\alpha_n},\end{aligned} \tag{1.28}$$

with $\omega_\sigma = \omega_1 + \ldots + \omega_n$, where

$$\mathbf{P}^{(n)}(t) = \frac{1}{2}\sum_{\omega''\geq 0}\left[\mathbf{P}^{(n)}_{\omega''}(t)e^{-i\omega'' t} + \mathbf{P}^{(n)}_{-\omega''}(t)e^{i\omega'' t}\right], \tag{1.29}$$

and

$$\mathbf{E}(t) = \frac{1}{2}\sum_{\omega'\geq 0}\left[\mathbf{E}_{\omega'}(t)e^{-i\omega' t} + \mathbf{E}_{-\omega'}(t)e^{i\omega' t}\right]. \tag{1.30}$$

For each carrier frequency ω', the electric field has slowly-varying envelope $E_{\omega'}(t)$ with bandwidth $\Delta\omega' \ll \omega'$, and also $\chi^{(n)}$ is nearly constant over the range $\omega' \pm \Delta\omega'$. This general form emphasizes the fact that multiple combinations of frequencies contribute to a nonlinear process. Note that because real-valued electric field in time domain is decomposed into complex fields at both $\pm\omega$, frequencies $\omega_1, \ldots, \omega_n$ can be either positive or negative in Eq. 1.28.

1.3 Second- and third-order nonlinearities

The nonlinear polarization becomes significant when the magnitude of the optical field is comparable with the Coulumb field that the orbiting electron experiences in the atom. Using the Bohr radius of the hydrogen atom $a_0 = \hbar^2/m_e e^2$ (in cgs), the atomic field is roughly estimated to be 5.1×10^{11} V/m. The optical intensity required to reach this upper limit is 3.5×10^{16} W/cm^2. It was not until 1960 that the invention of laser [5] made the observation of nonlinear effects in the optical regime possible. With the aid of the ruby laser, capable of $\sim 10^{11}$ W/cm^2 (focused) intensity, second harmonic generation [6] and two-photon absorption [7] were first reported in 1961. This triggered systematic studies in both theory [8] and experiment, and is thus considered as the onset of modern nonlinear optics. The most commonly observed nonlinear effects belong to second- and third-order nonlinearity. Higher order perturbative nonlinearities by bound electrons such as $\chi^{(5)}$ [9] also exist but are relatively poorly explored, due to the extremely weak effect and the complexity of mathematical analysis.

The second-order nonlinear effect usually involves generation of new frequencies. Examples are second harmonic generation ($\omega_\sigma = \omega + \omega$), frequency mixing ($\omega_\sigma = \omega_1 \pm \omega_2$, sum- and difference-frequency generation), optical parametric oscillation (OPO) [10] and amplification (OPA) [11]. These provide a convenient way to tune the laser wavelength for various applications. Moreover, parametric frequency down-conversion [12], where one higher-energy photon converts into two lower energy ones in the nonlinear medium, can produce entangled photon pairs [13] useful for the study of quantum optics and quantum computation. Optical rectification [14], on the other hand, is the extreme case of the difference frequency generation ($\omega_\sigma = \omega - \omega = 0$), where the two input frequencies are equal. This is useful when the input is a femtosecond laser pulse, because the generation of quasi-DC polarization follows the laser pulse envelope and thus emits radiation in the terahertz frequency range [15]. The field-induced birefringence, or Pockels effect [4], can be also explained as an extreme case of sum frequency generation by a DC electric field and an optical field ($\omega_\sigma = 0 + \omega$). The resulting optical field keeps its original frequency but the polarization is rotated.

Second-order nonlinearity yields significant radiation mainly at the surface or in some anisotropic lattice structures, where the spatial symmetry is broken. The third-order nonlinearity does not have this restriction and thus should be observable virtually in any optical material. Third harmonic generation and four-wave mixing [16] are the principle frequency mixing processes associated with $\chi^{(3)}$. Degenerate four-wave mixing also leads to optical phase conjugation [17], which reverses the wavefront evolution and is useful for correction of phase distortion induced by optical systems.

The nonlinear susceptibility tensor $\chi^{(3)}(-\omega; \omega, -\omega, \omega)$ has an interesting property: it modifies the refractive index of the medium according to the optical intensity. Assuming the field is linearly polarized along x direction, the total complex polarization

$$P_\omega^{(1)}(t) + P_\omega^{(3)}(t) = \chi^{(1)}(-\omega;\omega)E_\omega(t) + \frac{3}{4}\chi^{(3)}_{xxxx}(-\omega;\omega,-\omega,\omega)\left|E_\omega(t)\right|^2 E_\omega(t) \quad (1.31)$$

gives an effective refractive index

$$n_{\text{eff}}(t) = n_0\left(1 + \frac{3\pi\chi^{(3)}_{xxxx}}{2n_0^2}\left|E_\omega(t)\right|^2\right) \equiv n_0 + n_2 I(t), \quad (1.32)$$

where $n_0 = \sqrt{1 + 4\pi\chi^{(1)}}$ is the linear index of refraction, $n_2 = 12\pi^2\chi^{(3)}_{xxxx}(n_0^2 c)^{-1}$ is called nonlinear refractive index, $I = n_0 c|E|^2/8\pi$ is the optical intensity, and with the assumption $n_0 \gg n_2 I$. The factor 3/4 in the $P^{(3)}$ term of Eq. 1.31 originates from permutation. This nonlinear process produces a transient shift of refractive index which has the same temporal evolution as the intensity. Note that this is based on the assumption that the bound electron reacts much faster than the time scale of the field envelope. Comparing with commercially available ultrafast lasers with sub-100 fs pulse duration, the electronic response time in, for instance, optical glass, is usually < 1 fs as estimated in Sec. 1.1 and can be considered as instantaneous. The nonlinear refractive index n_2 is related to several effects, such as self-phase modulation, cross-phase modulation, self-focusing, and optical filamentation, which will be discussed later in this Chapter.

1.4 Resonant nonlinearities

Most of the optical nonlinearities mentioned in Sec. 1.3 are non-resonant effects. In a resonant nonlinear process, the overall bandwidth of at least two of the interacting fields overlaps an energy level separation in the atoms/molecules of the medium. The transition can be electronic between atomic or molecular orbitals, or vibrational as well as rotational in the molecule. An example of resonant nonlinearity is two-photon absorption, in which a transition $|g\rangle \rightarrow |f\rangle$ with energy absorption $\hbar\Omega_{fg}$ is excited by two photons ω_1 and ω_2 with $\omega_1 + \omega_2 = \Omega_{fg}$.

Another important type of two-photon resonant nonlinearity is Raman scattering. The Raman process can be viewed as inelastic scattering of the photon, which gains or loses energy with the coupling of a state transition. As shown in Fig. 1.1, the pump photon with frequency ω_p has two possible interaction paths through an intermediate "virtual state": (a) $|g\rangle \rightarrow |i\rangle$ then $|i\rangle \rightarrow |f\rangle$ with emission of a "Stokes" photon $\omega_S = \omega_p - \Omega_{fg}$ and (b) $|f\rangle \rightarrow |i\rangle$ then $|i\rangle \rightarrow |g\rangle$ with emission of an "anti-Stokes" photon $\omega_A = \omega_p + \Omega_{fg}$. Raman spectroscopy and Raman lasers are important tools in chemistry, biology and medical research, and Raman amplifiers are widely used in optical communication.

The rotational Raman process has some interesting properties. For non-polar molecules, it arises from the interaction between the laser field and an ensemble of randomly oriented molecules with anisotropic molecular polarizability. The laser electric field toques the molecular axes with highest polarizabity toward the field polarization direction, giving some time-varying "degree" of averaged alignment,

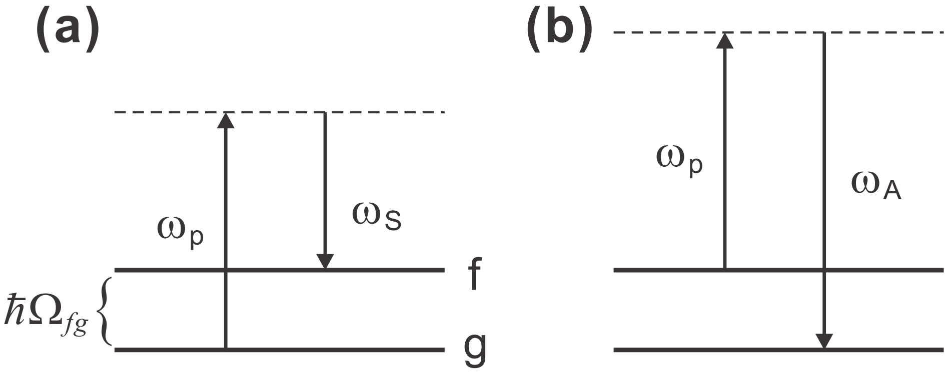

Figure 1.1: Energy level diagrams of (a) Stokes, and (b) anti-Stokes Raman scattering.

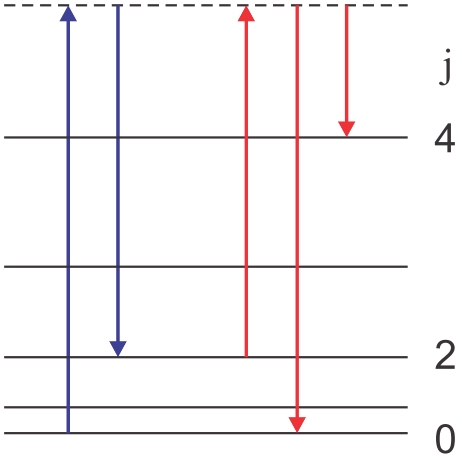

Figure 1.2: Energy level diagram showing some $j \rightarrow j \pm 2$ transitions in the rotational Raman process.

and it can keep evolving even after the laser field is turned off. In the language of quantum mechanics, a laser pulse can induce coherence between rotational states $|j\rangle$ and $|j \pm 2\rangle$ and thus excites a rotational wavepacket. The energy level diagram of such a process is shown in Fig. 1.2.

The temporal evolution of the rotational wavepacket can be observed via the transient shift of the refractive index in the ensemble of molecules, which is in proportional to the average degree of the alignment. When the laser pulse duration is shorter than a characteristic response time due to the rotational inertia of the molecule, the transient refractive index will have a delayed response with respect to the laser pulse. In other words, the adiabatic approximation is no longer valid, and the induced refractive index shift, to the zeroth order approximation (which will be explained in Chapter 4), is contributed by two parts:

$$\Delta n(t) = \Delta n_{\rm inst}(t) + \Delta n_{\rm rot}(t) = n_{2,\rm inst} I(t) + \int_{-\infty}^{\infty} n_{2,\rm rot}(t-\tau) I(\tau) d\tau. \qquad (1.33)$$

where $n_2 = n_{2,\rm inst}$ is the instantaneous, electronic response, and $n_{2,\rm rot}$ is the delayed molecular rotational response. Therefore, when studying the ultrashort pulse propagation in a molecular gas such as air, the effect of molecular alignment should be considered. As $\Delta n_{\rm rot}$ is proportional to peak laser intensity, it is sometimes also considered to be a $\chi^{(3)}$-related process in some literatures. A detailed discussion on both physics and applications of laser alignment of molecules will be given in Chapter 3, with both non-perturbative and perturbative treatments using quantum mechanics, similar to the derivation of nonlinear polarization outlined in Sec. 1.2.

1.5 Self- and cross-phase modulation

The nonlinear refractive index n_2 adds nonlinear temporal phase to the propagating light and generates new frequencies through self-phase modulation (SPM). Consider a laser pulse with a Gaussian intensity profile $I(t) = I_0 \exp(-t^2/\tau^2)$ propagating in a nonlinear and dispersionless medium for a distance L, and assume only instantaneous nonlinear refractive index $n_{2,\rm inst} = n_2$ exists. The accumulated nonlinear phase is $\phi_{NL}(t) = k_0 L n_2 I_0 \exp(-t^2/\tau^2)$, where t is the time coordinate in the moving frame of the pulse. The nonlinear temporal phase is equivalent to a time-dependent frequency shift

$$\Delta\omega(t) = -\frac{d\phi_{NL}}{dt} = \frac{4\pi L n_2 I_0}{\lambda\tau^2} t e^{-t^2/\tau^2}, \tag{1.34}$$

and is plotted in Fig. 1.3(a), along with $I(t)$. Figure 1.3(b) shows the spectrum of a transform-limited 100 fs laser pulse, and a typical spectrum of the same pulse after experiencing self-phase modulation is shown in Fig. 1.3(c), with significantly broadened bandwidth and spectral beating between newly-generated frequencies.

Cross-phase modulation (XPM) is similar to SPM but has two or more laser pulses with different polarizations or carrier frequencies involved. For example, consider the following processes:

$$\left(P^{(3)}_{\omega_2}(t)\right)_x = \frac{3}{2}\chi^{(3)}_{xxxx}(-\omega_2;\omega_1,-\omega_1,\omega_2)\left|(E_{\omega_1}(t))_x\right|^2 (E_{\omega_2}(t))_x\,, \tag{1.35}$$

and

$$\left(P^{(3)}_{\omega_2}(t)\right)_y = \frac{3}{2}\chi^{(3)}_{yxxy}(-\omega_2;\omega_1,-\omega_1,\omega_2)\left|(E_{\omega_1}(t))_x\right|^2 (E_{\omega_2}(t))_y\,. \tag{1.36}$$

One can clearly see that one wave can alter the phase of another wave, and this is especially useful for pump-probe type experiments studying the nonlinear optical properties of materials, in which the refractive index in the medium is altered by an intense pump beam and then is recorded as the nonlinear phase shift on a weak probe beam. This is the fundamental principal of the ultrafast refractive index measurement technique presented in Chapter 2. Note that for electronic nonlinearity, the permutation factor of XPM in both Eq. 1.35 and Eq. 1.36 is 3/2, which is twice

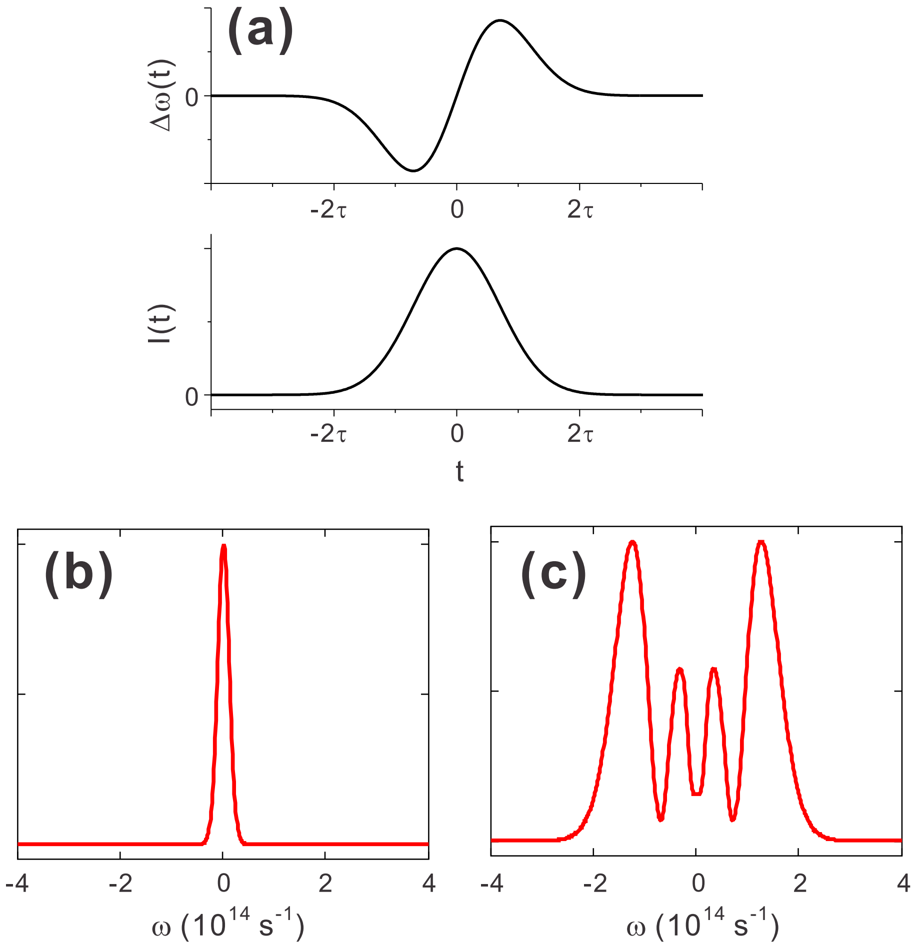

Figure 1.3: (a) The time-dependent frequency sweep $\Delta\omega(t)$ (top panel) experienced by a Gaussian laser pulse $I(t)$ with $1/e$ full width 2τ (bottom panel) during self-phase modulation. (b) The spectrum of a transform-limited Gaussian laser pulse with 100 fs full-width-at-half-maximum (FWHM) duration. (c) A calculated self-phase-modulated spectrum, using (b) as the input and assuming the nonlinear medium is dispersionless.

than the value in SPM process in Eq. 1.31.

1.6 Self-focusing and filamentation

The nonlinear susceptibility $\chi^{(3)}$ introduces not only a temporal but also a spatial effect. For a Gaussian beam $I(r) = I_0 \exp(-2r^2/w_0^2)$, the center of the beam experiences more phase shift than the edge does in the nonlinear medium. The laser beam then undergoes self-focusing because the medium acts like a lens. The effective focal length can be determined by the n_2-induced wavefront curvature. One of the applications is Kerr lens mode locking of Ti:Sapphire laser [18], which uses self-focusing in the gain medium to favor short pulse operation rather than continuous wave (CW) lasing in the cavity.

Self-focusing can balance diffraction when the laser power reaches a certain threshold, leading to the laser beam maintaining its size over a distance much longer than the Rayleigh range z_{R}. To show this, consider a linearly polarized Gaussian beam from vacuum ($z < 0$ plane) entering a dielectric material with linear refractive index n_0 ($z \geq 0$ plane) at normal incidence, and the beam waist w_0 is at the interface $z = 0$. The electric field for $z > 0$ is represented by Eq. 1.11.

For a infinitesimal propagation distance Δz into the dielectric material, diffraction changes the phase front curvature, and the corresponding phase shift is

$$\Delta\phi_{\mathrm{diff}}(r, \Delta z) = \frac{n_0 k_0 r^2}{2R(\Delta z)} \approx \frac{\pi \lambda r^2 \Delta z}{n_0 \left(\pi w_0^2\right)^2}. \qquad (1.37)$$

On the other hand, with the presence of n_2, the Gaussian beam also produces a radially-varying wavevector

$$k_{\mathrm{sf}}(r) = k_0 \left(n_0 + n_2 I_0 \exp\left(-\frac{2r^2}{w_0^2} \right) \right) \approx k_0 \left(n_0 + n_2 I_0 \left(1 - \frac{2r^2}{w_0^2} \right) \right), \tag{1.38}$$

and the phase difference is

$$\Delta\phi_{\mathrm{sf}}(r, \Delta z) = \Delta k_{sf} \Delta z = -\frac{4\pi n_2 I_0}{\lambda} \frac{r^2}{w_0^2} \Delta z. \tag{1.39}$$

Substituting $I = 2P/\pi w_0^2$, and requiring that $\Delta\phi_{\mathrm{diff}} = -\Delta\phi_{\mathrm{sf}}$, one obtains the critical power for self-focusing

$$P_{\mathrm{cr}} = \frac{\lambda^2}{8\pi n_0 n_2}. \tag{1.40}$$

Note that this threshold depends on power instead of intensity. Moreover, P_{cr} depends strongly on the beam profile. The critical power given by various prior works are in the form $\alpha\lambda^2/n_0 n_2$ and only differ by a multiplicative factor α. In particular, a popular value $P_{\mathrm{cr}} = 3.77\lambda^2/8\pi n_0 n_2$ is given by Ref. [19], and this will be used throughout this Dissertation.

Such self-sustained, transversely confined nonlinear propagation at the critical power was first theoretically discussed in 1964 [20], and was later observed in a solid [21] and a liquid [22], in which the laser beam collapsed into a “filament” with a typical diameter of sub-100 μm. In 1995 long-range filamentation of a femtosecond laser pulse accompanied by weak ionization in atmosphere was first reported, and it was suspected that the plasma also plays a critical role in the extended high

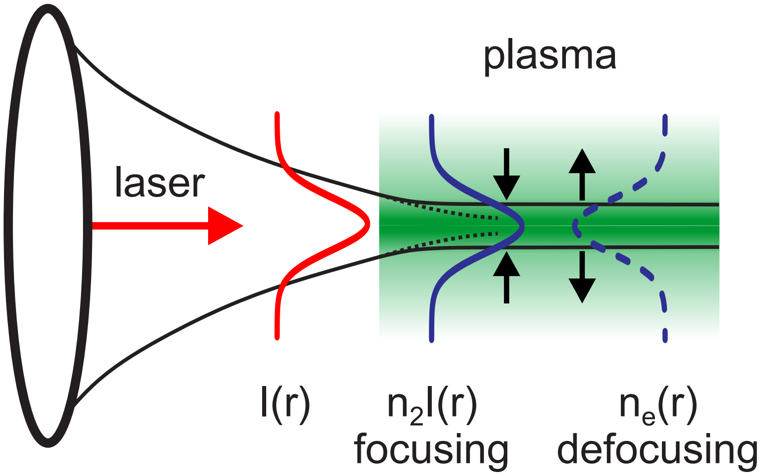

Figure 1.4: Schematic of laser filamentation.

intensity filamentary propagation [23]. To show this, consider an ideal Gaussian beam undergoing self-focusing in a gas. The intensity will eventually exceed the ionization threshold of the gas atoms. As will be seen later, laser ionization rate is intensity dependent, so the center of the beam generates more plasma than the edge, where the index of refraction in the plasma is

$$n(\omega) = \sqrt{1 - \frac{\omega_p^2}{\omega^2}}, \tag{1.41}$$

with the plasma frequency

$$\omega_p = \sqrt{\frac{4\pi n_e e^2}{m_e}}, \tag{1.42}$$

where n_e is the electron density. The plasma acts like a negative lens as illustrated in Fig. 1.4, which counteracts the self-focusing effect during the propagation.

1.7 Plasma and laser-induced ionization

Plasma is the gas composed of ions and free electrons, and the charged particles interact via Coulomb forces. The plasma response to the electromagnetic wave can be obtained from a special case of Lorentz-Drude model Eq. 1.3 by letting $\Omega = 0$, i.e., the electron is no longer bounded to the atom. Again the nucleus (ion) is assumed stationary, and the electric susceptibility becomes

$$\chi = -\frac{n_e e^2}{m_e} \frac{1}{\omega^2 + i\omega\nu}, \tag{1.43}$$

where n_e is the electron density, and the damping rate Γ is replaced by the collision frequency ν. Equation 1.43 is valid when there is only electron-ion elastic collisions without resonance, and also under the assumption that there is no magnetic field. If there is no collision then $\nu = 0$, and by using the relation $n = \sqrt{1 + 4\pi\chi}$ one obtains Eq. 1.41. Moreover, the electron quiver velocity in the laser field is $-v_{os} \sin \omega t$, where $v_{os} = eE/m_e\omega$ assuming a $E \cos \omega t$ driving field. The relativistic correction must be considered under an intense driving field, and the electron peak quiver velocity becomes $v_{os} = eE/(m_e\omega\sqrt{1 + a_0^2})$, where $a_0 = \gamma v_{os}/c = eE/m_e\omega c$ is the laser strength parameter (amplitude of normalized vector potential) introduced in Eq. 1.4, and $\gamma = 1/\sqrt{1 - v_{os}^2/c^2}$ is the Lorentz factor. The electron quiver motion becomes anharmonic and also shows “figure-eight” trajectories owing to the non-negligible effect of the magnetic field. In the relativistic regime, the plasma frequency becomes

$$\omega_p = \sqrt{\frac{4\pi n_e e^2}{\gamma m_e}}. \tag{1.44}$$

For the optical phenomena studied in this Dissertation, the intensities are in the regime of $a_0 \ll 1$.

To study laser-plasma interactions such as optical filamentation, it is crucial to understand the physics of laser ionization. Other effects in which laser ionization plays an important role include high-harmonic generation [24], cluster explosion [25], optically-pumped X-ray lasers [26, 27, 28], ionization blue-shift [29] and steepening [30] of the laser pulse. For a short laser pulse, plasma generation is mainly contributed by field ionization. For longer pulse duration the ionization process is more complicated. The leading edge of the laser pulse first weakly field-ionizes the atoms, and the free electrons continue wiggling under the influence of the laser field and produce more plasma through collisional ionization. The criterion that distinguishes between the two mechanisms is the electron-ion collision given by [31]

$$\nu_{ei} = \frac{4\sqrt{2\pi} Z^2 e^4 N_i \ln \Lambda_{ei}}{3 m_e^{1/2}} \left(\frac{1}{k_B T_e + 2U_p/3} \right)^{3/2}, \tag{1.45}$$

where N_i is the ion density, $\ln \Lambda_{ei}$ is the Coulomb logarithm for electron-ion collision, T_e is the electron temperature, and $U_p = e^2|E|^2/4m_e\omega^2 \approx 9.3 \times 10^{-14} I(\mathrm{W/cm^2})$ $[\lambda(\mu\mathrm{m})]^2$ eV is the electron ponderomotive quiver energy. For low electron temperature or high laser intensity $U_p \gg k_B T_e$, the temperature term can be omitted. For a typical filament in air, $Z = 1$, $N_i \sim 10^{16}$ cm^{-3}, $I \sim 5 \times 10^{13}$ W/cm^2, and $\ln \Lambda_{ei} \sim 13$

[32]. At the laser wavelength $\lambda = 0.8\ \mu$m, the characteristic collision interval is then $1/\nu_{ei} \sim 7$ ps and is much longer than the pulse duration (sub-100 fs) of a typical Ti:Sapphire laser, and in this case the collisional ionization is not important.

There are two different regimes in field ionization when the electron ionization potential is greater than energy of a photon $U_i > \hbar\omega$, which is usually true for the dielectric material at optical frequencies. Multiphoton ionization takes place when an electron absorbs multiple photons until the ionization threshold is reached. Tunneling ionization occurs when a laser field substantially distorts the Coulomb potential of the atom so that the electron can tunnel through the potential barrier. The schemes of both tunneling and multiphoton ionization are depicted in Figs. 1.5(a) and 1.5(b), respectively. These two different mechanisms in fact describe the same physics in the two extreme limits. When the laser period is longer than the time that the electron takes to tunnel through the barrier, it is in the regime of tunneling ionization. This condition can be met when the laser frequency is low or the field strength is high. On the other hand when the laser frequency is high or the field is weak, the electron is not able to tunnel through the barrier within a single optical cycle, and this is in the regime of multiphoton ionization. The Keldysh parameter γ_K [33] is used to determine which ionization model is more appropriate under the given conditions:

$$\gamma_K = \frac{\omega\sqrt{2m_e U_i}}{eE}, \tag{1.46}$$

where U_i is the ionization potential and E is the laser electric field. Tunneling ionization dominates when $\gamma_K < 1$, otherwise multiphoton ionization plays the

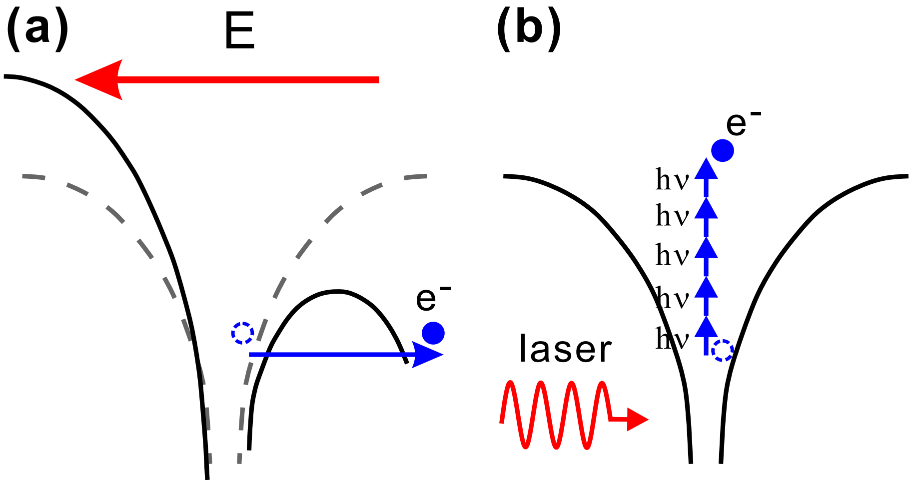

Figure 1.5: (a) Tunneling ionization, and (b) multiphoton ionization.

major role when $\gamma_K > 1$. The ionization potential of N_2 is 15.576 eV [34], and for typical laser intensity in the atmospheric filament $I \sim 5 \times 10^{13}$ W/cm^2 and $\lambda = 800$ nm, $\gamma_K = 1.6$, and thus multiphoton ionization is dominant over the tunneling ionization.

The rate of tunneling ionization is estimated by the Ammosov-Delone-Krainov (ADK) model [35] and then many other variants later on. The rate shown here is given by Ref. [36]:

$$
\begin{aligned}
w = \frac{\omega_{\mathrm{at}}}{2} C_{n^*}^2 \left(\frac{U_i}{U_h}\right) \frac{(2l+1)\,(l+|m|)!}{2^{|m|}\,(|m|)!\,(l-|m|)!} \\
\times \left[2\left(\frac{U_i}{U_h}\right)^{3/2} \frac{E_{\mathrm{at}}}{E}\right]^{2n^*-|m|-1} \exp\left[-\frac{2}{3}\left(\frac{U_i}{U_h}\right)^{3/2} \frac{E_{\mathrm{at}}}{E}\right],
\end{aligned}
\tag{1.47}
$$

where U_i is the ionization potential of the ion of interest, U_h is the hydrogen ionization potential, $\omega_{\mathrm{at}} = me^4/\hbar^3$ and $E_{\mathrm{at}} = m_e^2 e^5/\hbar^4$ are frequency and electric field in atomic units, $C_{n^*} = (2\varepsilon/n^*)^{n^*}(2\pi n^*)^{-1/2}$, $\varepsilon = 2.71828$ is the base of natural logarithm, and $n^* = Z(U_h/U_i)^{1/2}$ is the effective principle quantum number.

The multiphoton ionization rate is modeled by [37, 38]

$$w = \sigma^{(N)}(\omega) I^N(\mathbf{r}, \omega, t), \tag{1.48}$$

where I is the laser intensity, N is the minimum number of photons required to reach the ionization threshold, namely, $N = \lfloor U_i/\hbar\omega \rfloor + 1$ with $\lfloor \ \rfloor$ representing the floor function, and $\sigma^{(N)}(\omega)$ is the frequency-dependent cross section for N-photon ionization.

1.8 Nonlinear propagation

The general nonlinear propagation problem can be described by using $\mathbf{P}(t) = \mathbf{P}^{(1)}(t) + \mathbf{P}_{\mathrm{NL}}(t)$ in Eq. 1.10, where $\mathbf{P}_{\mathrm{NL}}$ is the nonlinear polarization. Wave propagation in the presence of $\chi^{(3)}(-\omega; \omega, -\omega, \omega)$, which is the origin of self-phase modulation and self-focusing described in Sec. 1.5 and Sec. 1.6, is of particular interest. In this case, adapting the paraxial wave equation Eq. 1.17 and assuming the adiabatic approximation is valid for $\chi^{(3)}$ over the laser pulse spectral range ($\omega_0 \pm \Delta\omega$), one gets

$$\frac{1}{2ik_0}\nabla_\perp^2 E + \frac{\partial E}{\partial z} + \left(\frac{dk}{d\omega}\right)\bigg|_{\omega_0} \frac{\partial E}{\partial t} + \frac{i}{2}\left(\frac{d^2k}{d\omega^2}\right)\bigg|_{\omega_0} \frac{\partial^2 E}{\partial t^2} = \frac{i\omega_0}{8\pi} n_0 n_2 \left|E\right|^2 E. \tag{1.49}$$

To deal with nonlinear propagation in the partially ionized medium, one may include the plasma susceptibility $\chi(\omega) = -n_e e^2/m_e\omega^2$ from Eq. 1.43, and the result is adding a term $(4\pi n_e(\mathbf{r}, t)e^2/m_e)E$ on the right hand side of Eq. 1.49. Moreover, for propagation in atmosphere, the refractive index contributed by molecular orientational effect $\Delta n_{\mathrm{rot}}(t) = \int_{-\infty}^{\infty} n_{2,\mathrm{rot}}(t-\tau) I(\tau) d\tau$ should be also considered, and Eq. 1.49 becomes

$$\begin{aligned} &\frac{1}{2ik_0}\nabla_\perp^2 E + \frac{\partial E}{\partial z} + \frac{1}{v_g}\frac{\partial E}{\partial t} + \frac{i}{2}\left(\frac{d^2 k}{d\omega^2}\right)\bigg|_{\omega_0} \frac{\partial^2 E}{\partial t^2} \\ &= \frac{4\pi n_e e^2}{m_e} E + \frac{i\omega_0}{8\pi} n_0 \left(n_{2,\mathrm{inst}} \left|E\right|^2 + n_{2,\mathrm{rot}} \otimes \left|E\right|^2\right) E, \end{aligned} \tag{1.50}$$

where $\otimes$ denotes convolution, and the molecular impulse response $n_{2,\mathrm{rot}}(t)$ will be derived in Chapter 3. To numerically solve this equation, it is more convenient to first transform the coordinate to the moving frame at group velocity v_g with local time axis $\tau = t - z/v_g$, which will be discussed in Chapter 5.

1.9 Outline of the Dissertation

This Dissertation presents experiments and simulations investigating the nonlinear optical response of air molecules and its crucial role in optical filamentation of intense laser pulses in atmosphere. In this Chapter, a brief review on nonlinear optics has been given, with the emphasis of the effects leading to nonlinear phase modulation and propagation. An overview of laser ionization and optical properties of the plasma has also been introduced.

Chapter 2 describes a single-shot, time- and 1-D-space-resolved method to measure the ultrafast temporal evolution of refractive index, and demonstrates the measurement of intensity-dependent index shift $n_2 I$ originates from instantaneous, electronic nonlinearity in the optical medium.

The following chapters focus on laser-induced molecular alignment. A treatment based on quantum perturbation theory is presented in Chapter 3, allowing the calculation of the ensemble-averaged alignment in the temporal vicinity of the femtosecond laser pulse, as well as the subsequent periodic alignment revivals due to the coherently excited rotational wavepacket. By applying the same technique used in Chapter 2, the transient refractive indices resulting from molecular orientational effect in some common linear gas molecules are measured in Chapter 4.

Recognizing the significance of the nonlinear index shift contributed by alignment of molecules, Chapter 5 investigates the molecular orientational effect on plasma generation in the femtosecond laser filament in atmosphere. An interferometric method is developed to directly resolve the radial and axial electron density along the meter-long filament, and for laser pulse durations longer than the rotational response timescale of the air molecules, the alignment-assisted filamentary propagation is observed, with increased plasma density and longer filament length. The experimental results are verified by simulations.

Chapter 2

Ultrafast measurement of transient refractive index shifts

2.1 Introduction

With the advance of laser technologies capable of delivering high power, the nonlinear refractive index plays an important role in both laser science and engineering. Solid-state pulsed lasers such as Nd:glass and Nd:YAG systems routinely generate several GW of power within a ~ 1 cm beam diameter. The maximum intensity is limited by $P_{\text{cr}}/A_{\text{eff}}$, where P_{cr} is the critical power for nonlinear self-focusing in the gain media or other optical elements, and A_{eff} is the effect laser beam area. When $P > P_{\text{cr}}$ self-focusing beats the natural diffraction so that catastrophic, filamenting optical damages may occur. In Ti:Sapphire-based chirped pulse amplification (CPA) systems with sub-50 fs pulse duration and multi-TW peak power, there are more considerations. The nonlinear phase is introduced to the laser pulse via self-phase modulation, and if it is accumulated too much throughout the system, the pulse cannot be compressed properly, with degraded peak power and also temporal contrast [39, 40]. The nonlinear phase shift is given by the so-called B-integral [39]:

$$B = \frac{2\pi}{\lambda} \int_0^L n_2 I dz, \tag{2.1}$$

where L is the medium length, and $B \ll 1$ implies better spatial and temporal quality of the laser. In optical fiber used in, say, communication, the optical intensity is usually much lower than in solid-state lasers, so that $n_2 I$ is smaller. However, the propagation distance L can be many kilometers so that propagation models must include the effect of n_2.

On the other hand, the nonlinear refractive index can have beneficial effects. For example, Kerr lens mode-locking, used by all modern Ti:Sapphire oscillators, is a simple but robust mode-locking technique which does not require any active component in the laser cavity [18]. Self-phase modulation (SPM) along with four-wave mixing are able to transform a narrow band laser pulse into coherent supercontinuum with frequency span more than an octave [41]. Optical Kerr gate [42] is the polarization rotation of a weak probe beam due to induced birefringence by a strong pump beam, and its application includes ultrafast all-optical switching [43], time-gated imaging [44], and fluorescence spectroscopy [45]. Nonlinear ellipse rotation [4] is related to self-induced birefringence and is used to improve the temporal contrast of ultrashort laser pulses [46]. Other examples of nonlinear propagation phenomena includes filamentation and optical soliton [47], which are studied extensively and have many potential applications.

As introduced in Chapter 1, the nonlinear index shift can be caused by prompt and delayed $\chi^{(3)}$ nonlinearities. In addition to the instantaneous electronic nonlinearity, the delayed nonlinearity also exists in the molecular gas and liquid, which is the rotational Raman effect, i.e., the orientational response induced by the femtosecond laser pulse. There are some other mechanisms which also contribute to the ultrafast refractive index shift in the optical medium. To name a few: in the molecular gas, the laser-induced rotational wavepacket produces periodic echoes of molecular alignment, which will be explained in Chapter 3 in detail. Another example is the optical ionization when the intensity at the front edge of a laser pulse exceeds the ionization threshold in the medium, resulting to rapid generation of plasma on $\sim$ fs time scale with an ionization front moving at the group velocity of the pulse, and the stepwise increase of plasma density could occur when the intensity exceeds first, second ionization threshold of atoms and so on. After the laser pulse, the free electrons and ions also recombine on a time scale ranging from $\sim$ ps to $\sim$ ns. In the plasma, the laser pulse in the relativistic regime can drive plasma waves through the ponderomotive force [48] or the Raman instability [49], with oscillation period $2\pi/\omega_p = 111$ fs for plasma density $n_e = 10^{18}$ cm^{-3}. Therefore to study these effects, a technique which is capable of measuring the ultrafast evolution of refractive index is desirable.

The nonlinear refractive index has been studied since 1960's, and several methods were developed to determine its magnitude, including nonlinear ellipse rotation [50, 51, 52], degenerate four-wave mixing (DFWM) [53, 54], nearly-degenerate three-wave mixing [55, 56], spectral analysis [57, 58], and Z-scan [59]. These methods all depend on the assumption of a mathematical relation between the refractive index variation $\Delta n(t)$ and a previously-known laser intensity envelope $I(t)$, hence do not have temporal resolution to characterize *arbitrary* changes of refractive index originated from other effects such as those mentioned above. DFWM and nearly-degenerate three-wave mixing are to determine $\chi^{(3)}_{xxxx}(-\omega;\omega,-\omega,\omega)$ by sending three waves as the input to the material and measuring the output intensity of the fourth wave. The spectral analysis is to fit the SPM spectrum with the nonlinear propagation model, and Z-scan is based on measuring the change of laser beam divergence due to self-focusing. The measurement results from all of the techniques above are also spatially-averaged and are beam profile dependent, as mentioned, for example, in Ref. [51], and thus do not have spatial resolution.

Time-resolved interferometry was employed for transient refractive index measurement [60, 61]. In general, this scheme employs a weak laser beam, which is sent to an interferometer and is first split into two arms as probe and reference, where the sample is placed in the probe arm. A strong pump beam overlaps the probe beam in the sample and induces cross-phase modulation. Then the probe beam is recombined with the reference, and the spatial interference pattern is sampled by the photodetector. The effective optical path length of the probe beam changes due to laser-induced refractive index shift in the sample, resulting to shift of the interference fringes. The time dependence of the fringe shift can be resolved by scanning the pump-probe delay, and therefore $\Delta\phi(t)$ and $\Delta n(t)$ can be reconstructed, with resolution limited by the probe pulse duration. Interferometry is highly sensitive but also unstable. Perfect spatial and temporal overlaps between two arms are required, and mechanical damping, ambient air flow reduction, or even active optical path length stabilization (for example, Ref. [60]) are usually required to compensate vibration-induced jitter of arm length difference. Careful design of optical system is also required to minimize wavefront distortion.

2.2 Single-shot supercontinuum spectral interferometry

Spectral or frequency domain interferometry (SI) [62] is another technique developed to study the ultrafast transient refractive index change induced by the interaction of intense short duration pump laser pulse with a medium. This method has been applied, for example, to measure the pump-induced phase modulation in absorptive materials [63] and optical fibers [64, 65]. Because of its sensitivity and also its simplicity as a linear method, SI has also proven useful in the temporal characterization of intense laser-plasma interactions, including density evolution of femtosecond laser produced plasma [66, 67], plasma shock waves [68], laser-cluster interactions [69], and laser wakefields [70, 71, 72].

The apparatus of SI is shown in Fig. 2.1. Two short, weak and identical laser pulses ("reference" and "probe") with temporal separation τ propagate collinearly along with an intense pump pulse through the interaction zone. The probe overlaps with the transient pump-induced refractive index change of the medium so that it gains a phase shift, while the reference arrives earlier and is not affected. The pump is then removed from the beam path and the reference and probe are sent to a spectrometer. The reference and probe fields E_{r} and E_{pr} are expressed as

$$E_{\mathrm{r}}(z=\Delta L,t)=E_{\mathrm{r0}}(t)\exp\left[i(k_0\Delta L-\omega_0 t)\right] \tag{2.2}$$

and

$$E_{\mathrm{pr}}(z=\Delta L,t)=E_{\mathrm{pr0}}(t-\tau)\exp\left[i\left(k_0\Delta L-\omega_0(t-\tau)\right)\right]\exp\left(i\Delta n\frac{\omega_0}{c}\Delta L\right), \tag{2.3}$$

where ΔL is the interaction length, E_{r0} and E_{pr0} are slowly varying amplitudes. Defining the Fourier transform as

$$\widetilde{A}(\omega) = \int_{-\infty}^{\infty} A(t) e^{i\omega t} dt, \tag{2.4}$$

and the inverse Fourier transform as

$$A(t) = \frac{1}{2\pi} \int_{-\infty}^{\infty} \widetilde{A}(\omega) e^{-i\omega t} d\omega, \tag{2.5}$$

the recorded spectrum is

$$\begin{aligned} \left|\widetilde{E}_{\mathrm{r}}(\omega) + \widetilde{E}_{\mathrm{pr}}(\omega)\right|^2 = \left|\widetilde{E}_{\mathrm{r0}}(\omega - \omega_0)\right|^2 + \left|\widetilde{E}_{\mathrm{pr0}}(\omega - \omega_0)\right|^2 \\ + 2\left|\widetilde{E}_{\mathrm{r0}}(\omega - \omega_0)\ \widetilde{E}^*_{\mathrm{pr0}}(\omega - \omega_0)\right|^2 \cos\left(\omega\tau + \Delta n \frac{\omega_0}{c} \Delta L\right), \end{aligned} \tag{2.6}$$

which produces a frequency dependent series of fringes with frequency spacing $2\pi/\tau$ plus a phase shift $\Delta\phi = \Delta n \omega_0 \Delta L/c$ caused by the pump-induced perturbation of the refractive index Δn, averaged over the duration of the probe pulse. This phase shift can be directly extracted from the interferogram using the method proposed by Takeda *et al* [73]. First, using a dummy variable t' to replace ω, a Fourier transform $t' \to \omega'$ is applied to Eq. 2.6, which produces three peaks located at zero and $\pm\tau$ "frequencies". Then a bandpass filter centered at $+\tau$ with proper width is used to select only the positive frequency component. To ensure correct phase retrieval, the value of τ should be large enough to prevent overlap of DC and $\pm\tau$ components, and its upper limit is determined by $2\pi/d\omega$, where $d\omega$ is the spectral resolution per pixel

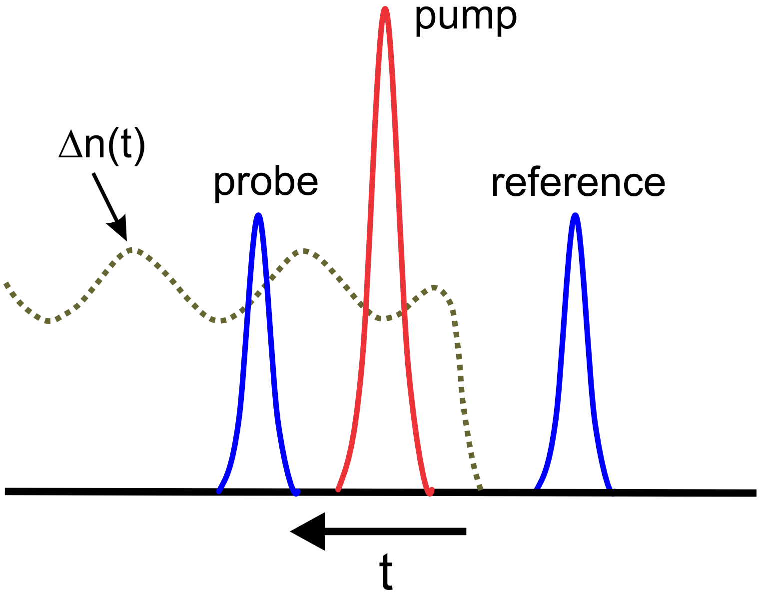

Figure 2.1: Schematics of spectral interferometry, after Ref. [72].

on the detector. Larger τ means denser fringes on the detector of the spectrometer, and there will not be enough detector pixels to represent a fringe if its period is too small, which causes loss of information. Finally, by performing an inverse Fourier transform of the filtered signal and subtracting the linear phase $\omega\tau$ from the result, the phase shift $\Delta\phi$ at a certain pump-probe delay can be recovered.

In the standard version of SI (for example, ref. [66]), the full evolution of the transient refraction index can be retrieved by stepping through relative time delays between the pump pulse and the reference-probe pulse pair, assuming that the probe pulse duration is much shorter than the time scale of refractive index modulation. Thus for such multi-shot method, there are two stringent requirements for obtaining a complete, high temporal resolution trace of refractive index evolution: an ultrashort probe pulse, and a high degree of shot-to-shot reproducibility. However, both shot-to-shot fluctuations in the pump pulse and the typically highly nonlinear response of the excited medium make good reproducibility difficult. Usually necessary is multi-shot averaging for each probe delay, which is time-consuming and may also result in the averaging to zero of real but small phase effects swamped by the shot-to-shot fluctuations. Standard SI is thus almost impractical for measuring the effects of high intensity laser pulses with repetition rate much lower than 1 Hz. For higher repetition rate systems, for example, the widely used 10 Hz Ti:Sapphire tabletop terawatt laser, in addition to fluctuations there may be long term drift of output energy, frequency and pulse shape, which can introduce systematic errors during the course of an experiment as the probe is delayed.

To overcome these difficulties, various versions of *single-shot* spectral interferometry (SSI) have been developed. These utilize chirped reference and probe pulses [74, 75, 76], or an unchirped reference pulse and a chirped probe pulse [77]. For a linearly chirped pulse with a Gaussian spectrum of full width at half maximum (FWHM) $\Delta\omega$ centered at $\omega = \omega_0$ and group delay dispersion (GDD) $\beta_2 = 1/2\ (\partial^2\phi/\partial\omega^2)|_{\omega_0}$, where $\phi(\omega)$ is the pulse phase in the frequency domain, the frequency sweep is given by $\omega = \omega_0 + bt$ with chirp parameter [78]

$$b \approx \frac{1}{2}\beta_2^{-1}\left[1 + 2\beta_2^{-2}(\Delta\omega)^{-4}\right]^{-1}.$$

The chirped probe pulse is temporally overlapped onto the full transient index evolution, so that the varying phase shift is encoded onto the chirped pulse's frequency components. This eliminates the needs of scanning the delay line.

The frequency-dependent fringe shift $\Delta\phi(\omega)$ recorded by the spectrometer allows extraction of the index-induced phase transient $\Phi(t = (\omega - \omega_0)/b)$ from a single interferogram. However, this frequency-to-time "direct mapping" approach is resolution-limited to [78]

$$\Delta t_{\mathrm{res}} \approx (\Delta\omega)^{-1}\left[1 + 2\beta_2^2(\Delta\omega)^4\right]^{1/2},$$

indicating that bandwidth-limited resolution of $\Delta t_{\mathrm{res}} \sim (\Delta\omega)^{-1}$ is achievable only for $\beta_2(\Delta\omega)^2 \ll 1$. Thus for fixed bandwidth pulses that are stretched longer (smaller b and larger β_2) in order to capture longer duration events, Δt_{res} increases and time resolution is degraded [78].

In order to take advantage of a potentially large bandwidth $\Delta\omega$ and to achieve the best time resolution, a different approach is needed for analyzing the spectral interferogram. For chirped probe and reference pulses $\widetilde{E}_{\mathrm{pr}} = \widetilde{E}_{\mathrm{pr0}}(\omega)\exp(i\phi_{pr}(\omega))$ and $\widetilde{E}_{\mathrm{r}} = \widetilde{E}_{\mathrm{r0}}(\omega)\exp(i\phi_r(\omega))$, where $\widetilde{E}_{\mathrm{pr0}}(\omega)$ and $\widetilde{E}_{\mathrm{r}}(\omega)$ are real and $\Delta\phi(\omega) = \phi_{\mathrm{pr}}(\omega) - \phi_{\mathrm{r}}(\omega)$ is the spectral phase difference between probe and reference, the same technique applied to original SI allows extraction of $\Delta\phi(\omega)$ from the spectral interferogram

$$\left|\widetilde{E}_{\mathrm{r0}}(\omega)\right|^2 + \left|\widetilde{E}_{\mathrm{pr0}}(\omega)\right|^2 + 2\left|\widetilde{E}_{\mathrm{r0}}(\omega)\widetilde{E}_{\mathrm{pr0}}(\omega)\right|\cos\left(\Delta\phi(\omega) + \omega\tau\right), \tag{2.7}$$

where τ is the probe pulse delay with respect to the reference pulse. Combining $\Delta\phi(\omega)$ with the knowledge of probe and reference spectra measured by the spectrometer $|\widetilde{E}_{\mathrm{pr0}}(\omega)| \propto \sqrt{I_{\mathrm{pr}}(\omega)}$, $|\widetilde{E}_{\mathrm{r0}}(\omega)| \propto \sqrt{I_{\mathrm{r0}}(\omega)}$, and also the chirped spectral phase $\phi_{\mathrm{r}}(\omega)$ of the reference pulse obtained by cross-phase modulation [78], the probe temporal phase shift $\Delta\Phi(t-\tau)$ is extracted using Fourier transforms [78]:

$$\Delta\Phi(t-\tau) = \mathrm{Im}\left[\ln\left(\frac{\int \widetilde{E}_{\mathrm{pr0}}(\omega)e^{i(\phi_{\mathrm{r}}(\omega)+\Delta\phi(\omega))}e^{-i\omega(t-\tau)}d\omega}{\int \widetilde{E}_{\mathrm{r0}}(\omega)e^{i\phi_{\mathrm{r}}(\omega)}e^{-i\omega(t-\tau)}d\omega}\right)\right], \tag{2.8}$$

and the time-domain probe signal $E_{\mathrm{pr}}(t)\exp(i\Delta\Phi(t))$ can be reconstructed. If an imaging spectrometer is used, the phase shift can be spatially resolved along the direction of the entrance slit, and a temporally and 1-D spatially resolved phase shift $\Delta\Phi(x,t)$ can be used to determine the transient refractive index $n(x,t)$ from $(2\pi/\lambda_0)n(x,t)L = \Delta\Phi(x,t)$, where λ_0 is the probe vacuum wavelength, x is the spatial coordinate transverse to the probe beam (and along the spectrometer slit), and L is the effective interaction length in the medium.

Essential to SSI is a broadband probe pulse. Specialized Ti:Sapphire oscillators and optical parametric amplifiers (OPA) might fulfill this requirement for output bandwidths exceeding 100 nm. However, this would dramatically increase the system cost and complexity. A convenient way to obtain broad bandwidth is through supercontinuum (SC) generation. By focusing a 80 fs, 1 mJ, 800 nm Ti:Sapphire laser pulse in atmospheric pressure air, $\sim$ 100 nm bandwidth SC probe and reference pulses centered at $\sim$ 690 nm were generated (with total SC energy 10–100 μJ), making single-shot supercontinuum spectral interferometry (SSSI) feasible [78]. In SSSI, temporal resolution of $\sim$ 10 fs was achieved [79], with probe bandwidth and spectrometer resolution as the only limiting factors. An added feature is that for experiments using 800 nm pump pulses, the SC probe central wavelength of $\sim$ 700 nm introduces negligible pump-probe walkoff owing to the mismatched group velocities during propagation through the interaction region. Pump-probe walkoff can degrade the temporal resolution, and the pump and probe wavelengths should be as close as possible to minimize this effect, thus it can be a problem for schemes using second harmonic probe pulses [77]. SSSI has been used to measure the transient Kerr nonlinearity in a solid [78], laser-induced double step ionization of helium [79], laser-heated cluster explosion [69, 80], and intense laser coupling into plasma waveguides [81]. Recently, SSI with a broadband chirped second harmonic (SHG) probe pulse at ~ 400 nm was used to measure laser wakefields induced by 800 nm pump pulses [82], but with less temporal resolution and more walkoff than with SSSI.

Note that a recent and popular method to generate a broadband supercontinuum is to guide a femtosecond laser pulse through a photonic crystal fiber [83]. However, fiber damage limits the pump laser pulse energy to the nanojoule level [84]. For a single-shot measurement where there may be significant background light, such as in laser-plasma experiments [69], nanojoule supercontinuum pulse energy is too low for practical application.

In this chapter, an improved SSSI setup employing a commercial kilohertz regenerative amplifier system producing 1 mJ, 110 fs pulses is implemented. SC pulses are generated with much lower pulse energy (than in Ref. [78]) in a sealed Xe gas cell, leaving sufficient pulse energy to use as a pump in a wide range of experiments. This new configuration will be discussed in detail, and it has been applied to measurements of the Kerr nonlinearity in optical media. The measurement of molecular orientational effect on transient refractive index is also presented in this chapter and will be further investigated in Chapter 4. The SC pulses also have excellent shot-to-shot stability, making possible the averaging of results over many thousands of shots if desired. The measurements shown in Chapter 4 have benefited from direct averaging of multiple interferograms, especially for laser-induced alignment revivals of D_2 and H_2, which produce very weak refractive index shift in our experiment conditions.

2.3 Experimental setup

Two laser pulses were split at beamsplitter BS1 from the output of a commercial Ti:Sapphire regenerative amplifier (RGA) (Spectra-Physics Spitfire) with 1 kHz repetition rate (see Fig. 2.2). In our previous work [69, 78, 79, 80, 81] SC was generated by focusing in 1 atm air a ~ 1 mJ, 70 fs laser pulse split from a 10 Hz, 2 TW Ti:Sapphire laser system based on a 10 Hz regenerative amplifier followed by two power amplifiers. Pulse-to-pulse output energy fluctuations of $\sim$ 10–15% were determined by fluctuations of the 10 Hz, 532 nm pump laser pulses. Here, the 1 kHz RGA is pumped by a CW arc lamp-pumped, intra-cavity doubled Q-switched Nd:YLF laser (Spectra Physics Merlin), with pulse-to-pulse energy fluctuation less than 2%. The result is very stable SC on a shot-to-shot basis.

For SC generation, one of the pulses (~ 300 μJ) was focused at $f/6$ into an 11-cm long xenon-filled (0–2 atm) gas cell (XGC) with 1-mm thick fused silica entrance and exit windows. Xenon gas has previously been observed to generate very broad supercontinuum spectra under femtosecond laser pulse illumination [85].

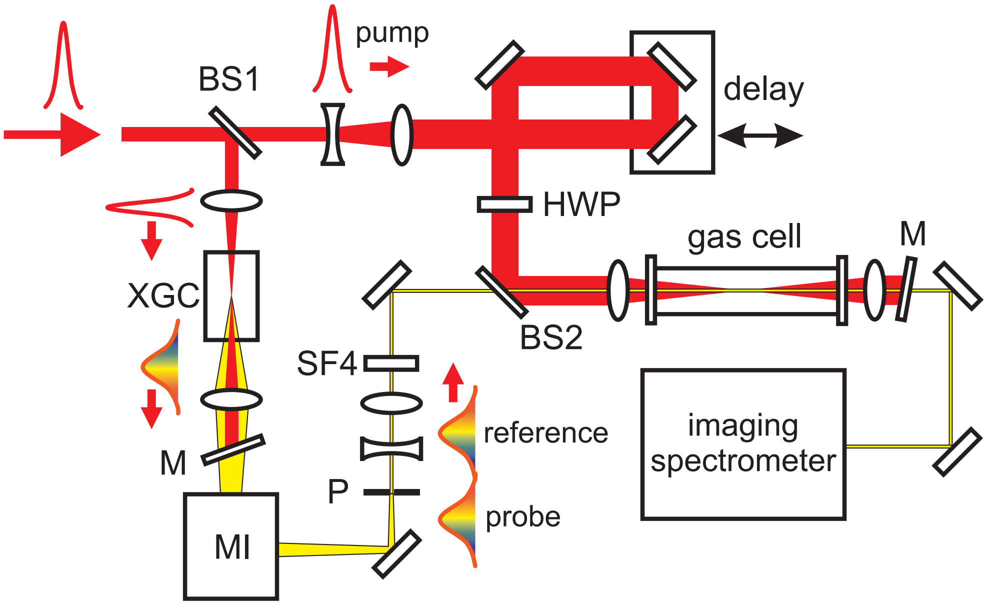

Figure 2.2: Experimental setup. BS1: beamsplitter, XGC: xenon gas cell, MI: Michelson interferometer, P: 500 μm pinhole, SF4: 2.5-cm thick SF4 glass as dispersive material, HWP: half waveplate, M: zero degree Ti:Sapphire dielectric mirror, BS2: beamsplitter for combining pump and SC pulses. The pump beam energy can be tuned by another set of half waveplate and polarizer, which is not shown in this figure.

The SC pulse (along with the fundamental) emerges from the propagation filament induced by $\chi^{(3)}$ self-focusing. The cell windows were sufficiently far from the beam waist/filament that they provided no contribution to the SC generation. The conical emission was transversely spatially chirped, with frequency increasing with radial position. This emission, with approximately 10 μJ/pulse in the SC component and the rest at the fundamental frequency, was collected by a lens at $f/3$ and converted into weakly converging beam, from which the fundamental component was removed by passing the beam through a high reflection dielectric mirror (M) centered at $\lambda = 800$ nm. The slightly converging SC pulse was then passed through a Michelson interferometer (MI) to generate a pair of co-propagating, identical pulses with variable delay (the reference and probe pulses). Beyond the Michelson, the converging beam spot was now small enough to efficiently reduce its spatial chirp and shape its transverse profile by placing a 500-μm diameter pinhole (P) in its path. By fine tuning the transverse position of the pinhole, a SC beam with high brightness, broad bandwidth, good spatial coherence, and uniform beam profile was obtained. The SC beam was then collimated by a telescope with 2× magnification, and the pulse duration and chirp parameter were tuned by adding appropriate lengths of dispersive material in the beam path. In the results shown here, a 2.5-cm thick optical grade SF4 glass window is used. This stretched the reference/probe pulses to ~ 2 ps, providing a 2 ps window for single-shot measurements of refractive index transients.

The other beam from BS1 was passed through an adjustable delay line and served as the pump. A half waveplate (HWP in Fig. 2.2) in this beam allowed independent pump polarization adjustment with respect to the SC beam. The SC and the pump beam paths were collinearly recombined at BS2, and focused by a f=41 cm lens into the sample to be measured. In the work presented here, the sample was either 200 μm thick BK7 window or a 45 cm long high pressure gas cell with 1 cm thick broadband anti-reflection coated fused silica windows. In the case of the gas cell, the windows were far enough from the pump focus so as to not contribute to any pump-induced phase shifts (cross phase modulation) to the probe. To keep the pump intensity low at the cell windows, the pump beam was expanded with 2× magnification before the focusing lens. The pump Rayleigh range in the cell was $z_{0,\mathrm{p}} = 4.5$ mm with a full width at half-maximum (FWHM) focal spot size of 36 μm by 27 μm. Pump peak intensities were determined by the known pulse energy, pulse shape (from SSSI (see below) and independently from a Grenouille measurement [86]), and relay images of the pump spot recorded on a 14-bit CCD camera. The SC beam Rayleigh range was $z_{0,\mathrm{sc}} = 24.6$ cm with a FWHM spot size of 270 μm. In the interaction region, the probe beam therefore significantly overfilled the pump in the transverse plane, allowing observation of the pump-induced phase shift across the full pump profile. The "exit" plane of the pump interaction region was imaged beyond the sample onto the spectrometer slit at 6.9× magnification. Along this beam path, the combined pump/SC beam exiting the sample was passed through a zero degree dielectric Ti:Sapphire mirror (M) to reject the pump beam. The f/2 imaging spectrometer consisted of a diffraction grating with 1200 mm^{-1} groove density and a 10-bit CCD camera (SONY XCD-SX910), which captured full frame images of 1280×960 pixels at 7.5 frames per second. The ~ 72 nm spectral window projected on the CCD sensor chip ranged from 651.7 nm to 723.2 nm, and the one-dimensional source spatial resolution was 0.67 μm/pixel along the entrance slit direction.

As discussed earlier, extraction of the probe temporal phase shift $\Delta\Phi(x, t)$, where x is the coordinate along the spectrometer slit axis in the image plane, can be achieved by either direct frequency-to-time mapping or through Fourier transforms. For extraction by Fourier transform, the full spectral phase $\phi_{\mathrm{pr}}(\omega) = \phi_{\mathrm{r}}(\omega) + \Delta\phi(\omega)$ of the probe pulse is required, necessitating knowledge of the reference phase $\phi_r(\omega)$. Determining this through the second order dispersion $\phi_{\mathrm{r}}(\omega) \cong \beta_2(\omega - \omega_0)^2$ and neglecting higher order terms has been found to be sufficient for pump pulses > 20 fs [78]. To obtain β_2, a calibration procedure using cross-phase modulation, similar to the method in Ref. [78], was applied: interferograms were recorded under varying delay τ between pump and probe pulses in 100 psi argon, giving a sequence of identical $\Delta\phi(\omega)$ traces, but shifted in frequency. For each trace the frequency ω' of maximum $\Delta\phi(\omega)$ was identified and plotted against τ. A linear fit to this plot gave for the linear chirp parameter $1/b = a = 2\beta_2\left(1 + (2\ln(2))^2\beta_2^{-2}(\Delta\omega)^{-4}\right) = 7820\ \mathrm{fs}^2$. This agrees well with the calculated total dispersion introduced by total lengths of 1.1 cm of fused silica, 3.5 cm of BK7, and 2.5 cm of SF4 in the SC beam path. Our SC probe spectral width of ~ 100 nm gives $\beta_2^{-2}(\Delta\omega)^{-4} \ll 1$, and therefore $\beta_2 \approx a/2$.

2.4 Results

Figure 2.3 shows sample spectral interferograms and extracted transient refractive index shifts $\Delta n(x,t)$ using the gas cell filled with argon at room temperature. The CCD shutter speed was set to ~ 1 ms to ensure that only one shot was recorded per image. Argon is a monatomic gas where the lowest order nonvanishing nonlinearity ($\chi^{(3)}$) at 700–800 nm is electronic, nonresonant, and nearly instantaneous, so below the ionization threshold the time- and 1D-space-dependent nonlinear phase shift due to cross-phase modulation (XPM) is given by $\Delta\Phi_{\mathrm{Ar}}(x,t) = k\int \Delta n(x,z,t)dz = k(2n_{2,\mathrm{Ar}})\int I(x,z,t)dz$, where $n_{2,\mathrm{Ar}}$ is the self-phase modulation (SPM) nonlinear refractive index for argon [2]. It is thus convenient to define an effective interaction length L by $\Delta\Phi_{\mathrm{Ar}}(x,t) = k\Delta n(x,t)L = k(2n_{2,\mathrm{Ar}})I(x,t)L$. Thus the phase shift follows the time and one-dimensional transverse envelope $I(x,t)$ of the pump pulse intensity.

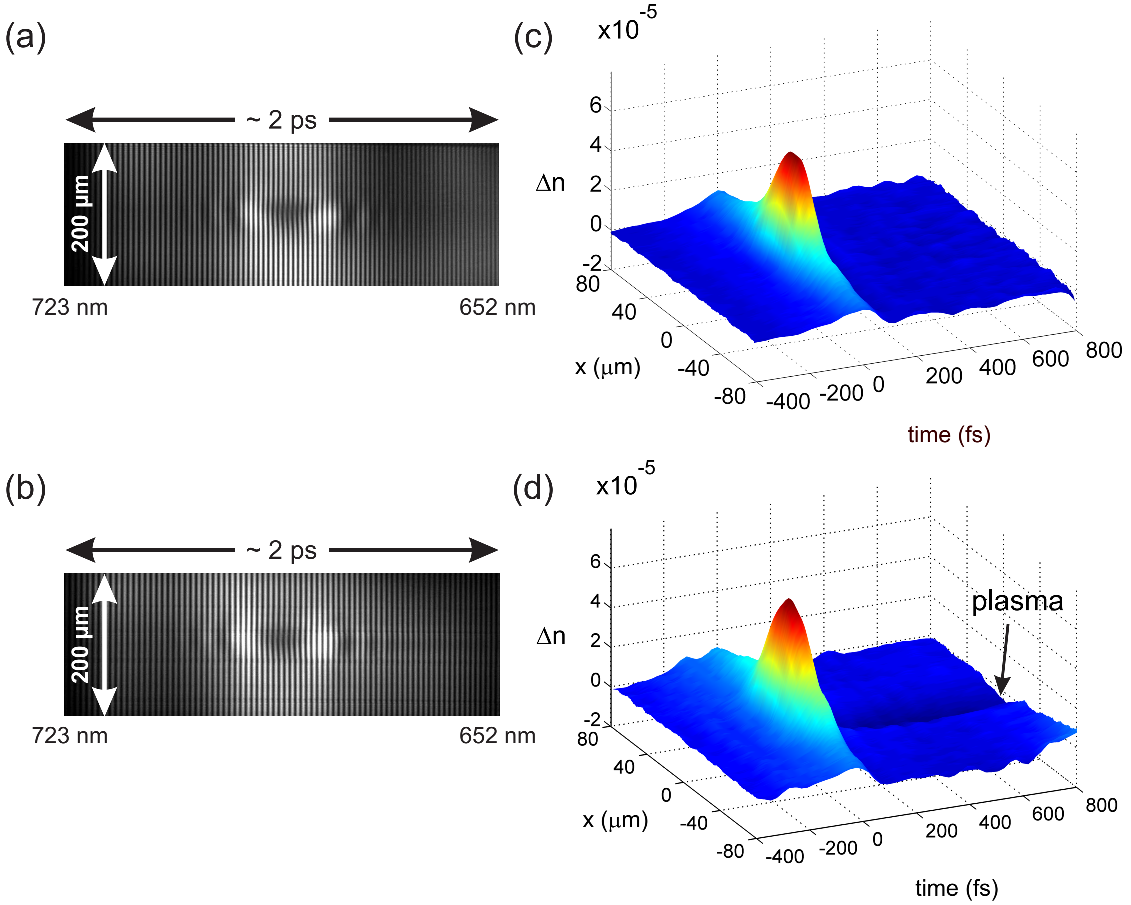

Figure 2.3: Spectral interferograms showing laser-induced, wavelength-dependent fringe shift in argon at (a) 7.8 atm and $I_{\text{peak}} = 4.1 \times 10^{13}$ W/cm^2 and (b) 4.4 atm and $I_{\text{peak}} = 7.7{\times}10^{13}$ W/cm^2, where plasma is observed as a long tail extending to the short wavelength edge on the interferogram. Note that the SC probe and reference pulses are positively chirped, thus a shorter wavelength on the interferogram means a later time. The 1D space and time variations of the effective argon nonlinear refractive index change Δn extracted from (a) and (b) are shown in (c) and (d), respectively. The positive index shift is due to instantaneous electronic nonlinearity, which follows the pump pulse temporal profile. The plasma-induced negative index shift is seen in (d) following the pump pulse. The baseline noise in extracted $\Delta n(x,t)$ plots is determined by the CCD camera pixel size, which sets the minimum resolvable fringe shift in (a) and (b).

In Fig. 2.3(a) the pump pulse intensity was intentionally kept far below the argon field ionization threshold ($\sim 10^{14}$ W/cm^2 [87]). In Fig. 2.3(b) the intensity was increased so that plasma was generated. The wavelength-dependent interference fringe shifts in Fig. 2.3(a) and Fig. 2.3(b) represent the transient modification of refractive index in the argon gas and gas/plasma. Figure 2.3(c) shows the 1D space and time variation of the argon nonlinear refractive index shift $\Delta n(x,t)$ extracted from Fig. 2.3(a), using an effective nonlinear interaction length $L_{\mathrm{Ar}} = 2.85$ mm, which is explained below: note that for well-defined gas interaction lengths, such as provided by a thin ($\ll 2z_{0,\mathrm{p}}$) gas jet [79], L could be considered a known quantity and n_2 could be extracted. Here, however, for the longer gas cell, where the effective nonlinear interaction length is less well-defined, we wish to extract L. The procedure was to compare the nonlinear Kerr effect phase shift in the gas cell, $\Delta\Phi_{\mathrm{Ar}}(x,t)$, to that in a thin BK7 (borosilicate glass) window $\Delta\Phi_{\mathrm{BK7}}(x,t) = k(2n_{2,\mathrm{BK7}})L_{\mathrm{BK7}}I(x,t)$, where the window thickness is $L_{\mathrm{BK7}} = 200\ \mu\mathrm{m} \ll 2z_{0,\mathrm{p}}$. Thus $L_{\mathrm{Ar}} = \frac{(\Delta\Phi_{\mathrm{Ar}})(2n_{2,\mathrm{BK7}})}{(\Delta\Phi_{\mathrm{BK7}})(2n_{2,\mathrm{Ar}})}L_{\mathrm{BK7}}$, using values of $n_{2,\mathrm{BK7}} = 1.75 \times 10^{-16}$ cm^2/W obtained from SSSI measurement described later, and $n_{2,\mathrm{Ar}} = 9.8 \times 10^{-20}$ cm^2 W^{-1} atm^{-1} from Ref. [88].

Figure 2.3(d) shows $\Delta n(x,t)$ extracted from Fig. 2.3(b), including the generation of plasma. The initial profile of Δn is similar to Fig. 2.3(c), then the onset of plasma generation drives Δn to a value $\Delta n_{\mathrm{plasma}} \sim -0.8 \times 10^{-5}$, corresponding to an on-axis electron density of 3.8×10^{16} cm^{-3}, which stays effectively constant for the remainder of the 2 ps probe window. The gas density is 1.2×10^{20} cm^{-3}, which means only $\sim 0.04\%$ of argon atoms are ionized. Plasma recombination occurs on a longer, nanosecond time scale. As an example of the good shot-to-shot stability

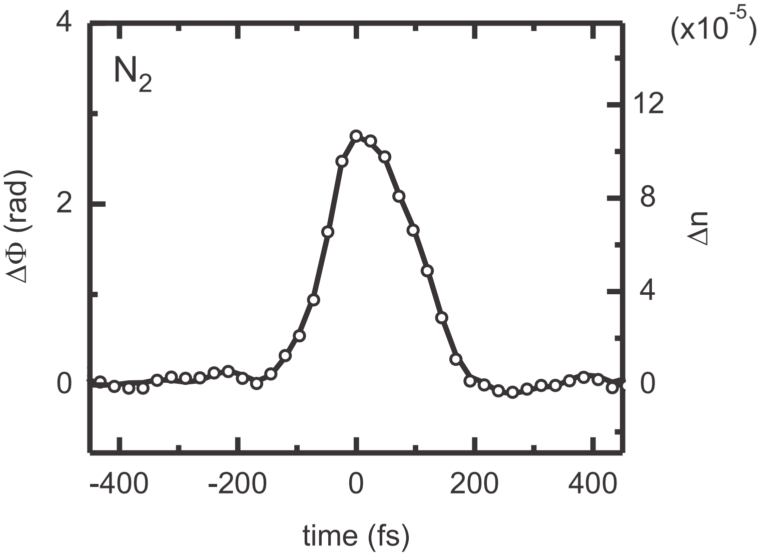

Figure 2.4: 250 shot average (solid line) and a single shot trace (circles) of refractive index transient $\Delta n(x=0,t)$ (and extracted phase $\Delta\Phi(x=0,t)$) along the beam axis for 6.4 atm nitrogen. The results agree well, confirming good shot-to-shot stability. The pump energy was 60 μJ, corresponding to $I_{\text{peak}} = 4.1 \times 10^{13}$ W/cm^2, below the threshold for nitrogen ionization.

made possible through use of a kHz regenerative amplifier system, Figure 2.4 shows a 250 shot average and a single shot sample of the phase and refractive index transient from an unionized 5.1 atm nitrogen sample. The results agree well. Evidence of shot-to-shot stability of the SC generation in both spectrum and transverse spatial distribution is further demonstrated by Figure 2.5, which shows a comparison of a single shot spectral interferogram to an interferogram averaged over 300 shots, of pump interaction with 5.1 atm of N_2O.

Figure 2.6 shows the nonlinear phase shift $\Delta n_{\text{BK7}}(x,t)$ for the 200 μm thick BK7 window, which compares quite well to $\Delta n_{\text{Ar}}(x,t)$ in Fig. 2.3(c), as it should: in BK7 glass, the dominant low order nonlinearity ($\chi^{(3)}$) is also electronic, nonresonant, and nearly instantaneous. Thus both phase shifts are proportional to $I(x,t)$, justifying our method above for finding L_{Ar}.

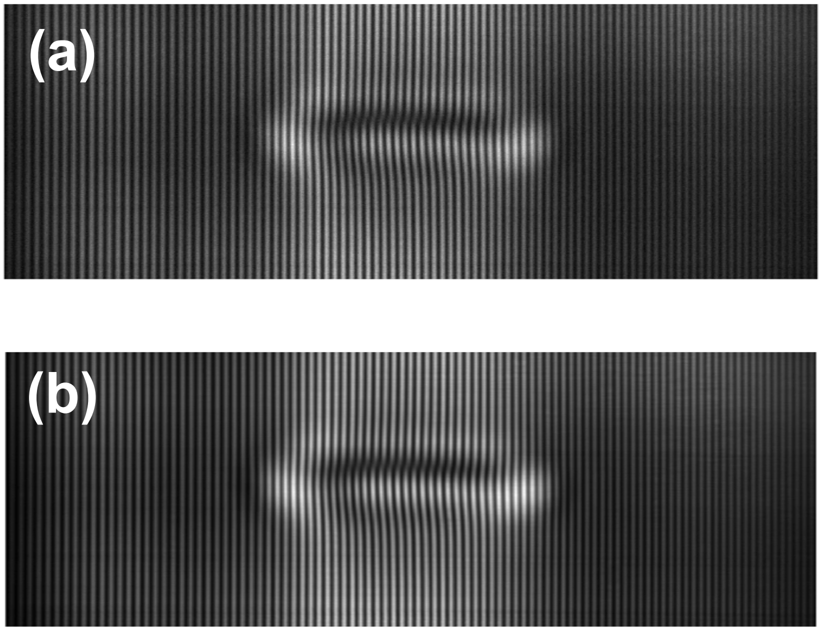

Figure 2.5: (a) A sample single-shot spectral interferogram taken in 5.1 atm N_2O with 1.4×10^{13} W/cm^2 pump intensity. (b) Averaged spectral interferogram image over 300 laser shots, taken in the same condition as (a). The close resemblance between single-shot and multi-shot-averaged spectra indicates good stability in SC generation.

Figure 2.7 shows a comparison of the pump-induced nonlinear index change in Ar, N_2, and N_2O samples for times near the pump laser pulse. Unlike Ar, the other species are linear molecules with an inertial contribution to their nonlinearity, which corresponds to delayed molecular axis alignment along the laser polarization resulting from the torque experienced by the induced molecular dipole in the laser field [89]. The prompt and delayed refractive index response can be expressed as $\Delta n(t) = 2n_{2,\mathrm{SPM}}I(t) + \int_{-\infty}^{\infty} R(\tau)I(t-\tau)d\tau$, where $n_{2,\mathrm{SPM}}$ is the SPM nonlinear refractive index, and R is a molecular response function [90]. As discussed earlier, the response of Ar is near instantaneous, as expressed by the first term only. Due to the inertial effect, the nonlinear responses of N_2 and N_2O do not follow the laser pulse intensity envelope, which is represented by the Ar response. The full theory

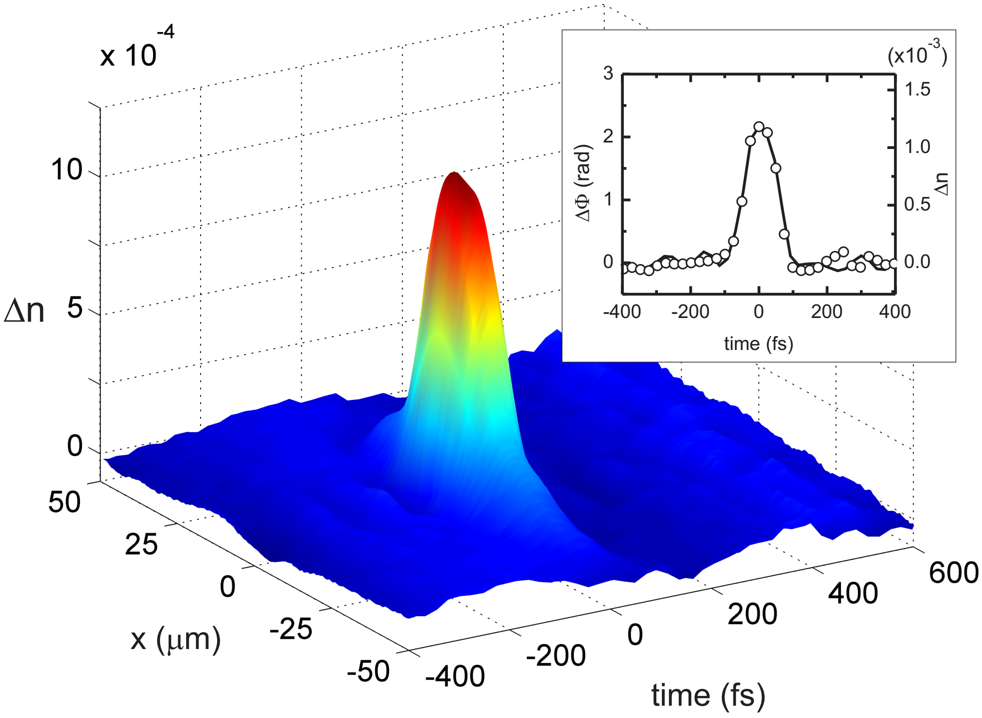

Figure 2.6: Induced nonlinear refractive index shift $\Delta n(x,t)$ from a 200 μm-thick BK7 window with 5 μJ pump pulse energy and 3.4×10^{12} W/cm^2 peak intensity. The inset is the probe phase shift $\Delta\Phi(x=0,t)$ with corresponding $\Delta n(x=0,t)$ (solid line). The temporal phase evolution profile from 7.8 atm argon (Fig. 2.3(a)), normalized to the same peak phase value, is shown here for comparison (circles).

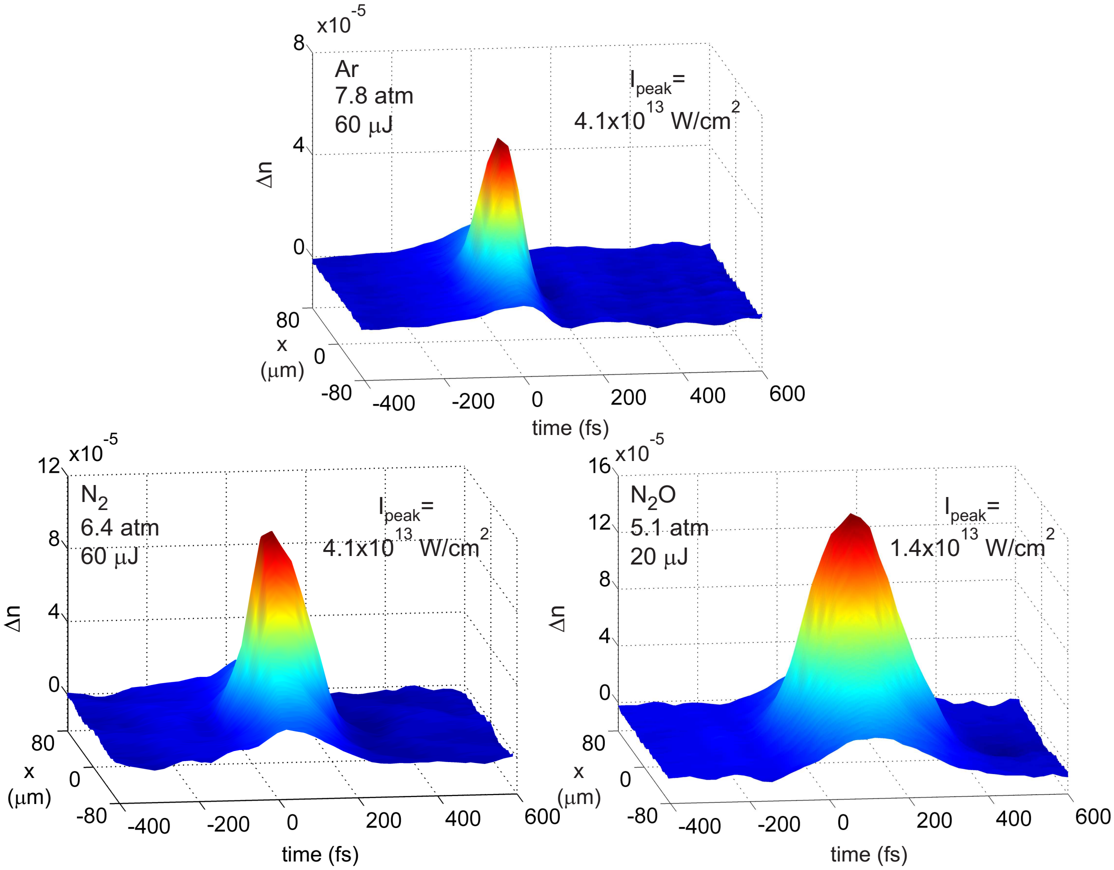

Figure 2.7: Measured nonlinear refractive index shift $\Delta n(x,t)$ in Ar, N_2, and N_2O. For the linear molecules N_2 and N_2O, part of the nonlinearity is contributed by the inertia of molecular rotation, which causes a delayed response which does not follow the pump pulse shape.

explanation on the molecular rotational effect will be given in Chapter 3.

2.5 Conclusion

In conclusion, a spectral interferometer is developed, which is capable of recording single shot records of refractive index transients with ~ 10 fs time resolution and 1D space resolution in a 2 ps window. It uses chirped supercontinuum probe pulses generated from the self-focusing of few hundred microjoule, femtosecond pulses in a Xe gas cell. This diagnostic is suitable for use with modest energy femtosecond laser systems such as those based on kHz or multi-kilohertz Ti:Sapphire regenerative amplifiers, which are the workhorse system in many ultrafast optics and molecular physics laboratories.

Chapter 3

Laser alignment of linear molecules

3.1 Introduction

Many species of liquid or gas molecules can be aligned along a specific symmetry axis with the presence of an external electric field, and a famous example is the liquid crystal. In fact, the field alignment applies to any molecule with anisotropic polarizability. Take a simple diatomic molecule without permanent dipole moment, such as oxygen or nitrogen, for example, in an external electric field. The formal treatment to this problem requires quantum mechanics, but it is intuitive to show the molecular behavior qualitatively using classical approach. As shown in Fig. 3.1, the molecular polarizability tensor $\boldsymbol{\alpha}$ can be decomposed into two components along the two orthogonal symmetry axes. $\alpha_{\parallel}$ is along the molecular "long" axis (z in Fig. 3.1(a)) and generally is larger than $\alpha_{\perp}$, which is in the direction of the "short" axis lying on the plane defined by the field direction ($\hat{\mathbf{z}}'$ in Fig. 3.1(a)) and the molecular long axis z. When the electric field is applied, the induced dipole moment is

$$\mathbf{p} = \mathbf{p}_{\parallel} + \mathbf{p}_{\perp} = \alpha_{\parallel} E \cos\theta \hat{\mathbf{e}}_{\parallel} + \alpha_{\perp} E \sin\theta \hat{\mathbf{e}}_{\perp}, \tag{3.1}$$

where $\hat{\mathbf{e}}_{\|}$ and $\hat{\mathbf{e}}_{\perp}$ are unit vectors along the long and short axes, respectively. The molecule thus experiences a torque

$$\boldsymbol{\tau} = \mathbf{p} \times \mathbf{E} = \Delta\alpha E^2 \sin\theta\cos\theta(\hat{\mathbf{e}}_{\perp} \times \hat{\mathbf{e}}_{\|}), \tag{3.2}$$

where $\Delta\alpha = \alpha_{\|} - \alpha_{\perp}$. The stored energy can be calculated by rotating the dipole against the field:

$$U = \int \tau d\theta' = \Delta\alpha E^2 \int_0^\theta \sin\theta' \cos\theta' d\theta' = \frac{1}{2}\Delta\alpha E^2 \sin^2\theta. \tag{3.3}$$

By choosing $U(\theta = \pi/2) = -\frac{1}{2}\alpha_{\perp}E^2$, one can obtain the induced dipole potential

$$U = -\frac{1}{2}E^2\left(\alpha_{\|}\cos^2\theta + \alpha_{\perp}\sin^2\theta\right) = -\frac{1}{2}\mathbf{p}\cdot\mathbf{E}. \tag{3.4}$$

The factor 1/2 comes from the fact that this is induced not permanent dipole moment, and hence is proportional to $\int EdE$ rather than $E \cdot E$.

If the molecule is treated as a classical rigid rotor and has the moment of inertia I about a certain rotation axis, then it is rotated by the torque with the angular acceleration

$$\ddot{\theta} = -\frac{\tau}{I} = -\frac{\Delta\alpha E^2}{2I}\sin 2\theta, \tag{3.5}$$

where $I = \sum m_i r_i^2$ is calculated from the mass of ith atom m_i and its normal distance to the rotation axis r_i, and the rotation axis intersects the molecular center of mass. I is assumed constant if the molecule is not deformed by the centrifugal

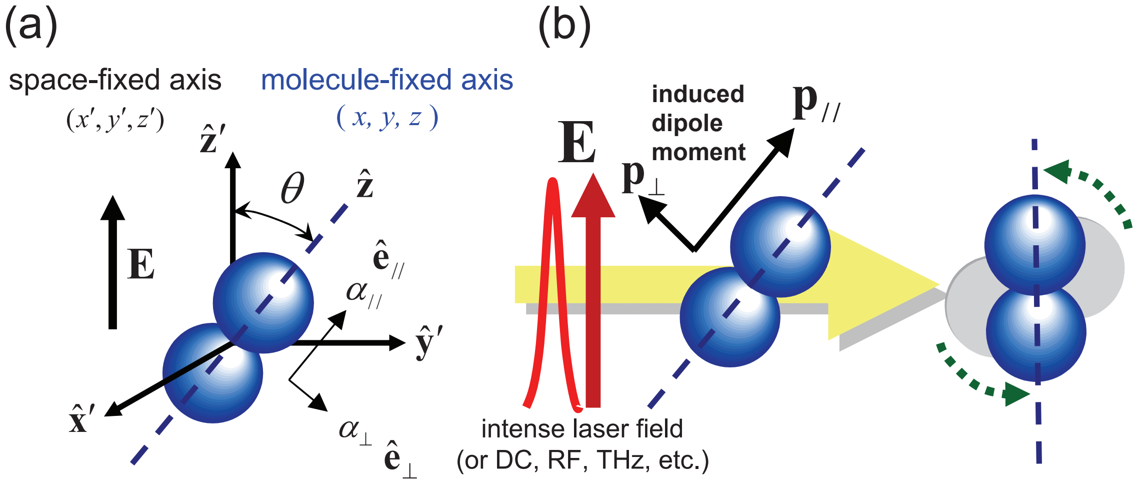

Figure 3.1: (a) The classical "dumbbell" model of a diatomic molecule having anisotropic polarizabilities $\alpha_{\parallel}$ and $\alpha_{\perp}$, with molecule-fixed and space-fixed coordinates labelled. (b) A linearly-polarized electric field induces a net dipole moment which is generally not in the same direction as the field. The molecule then experiences a torque from the electric field and tends to line up along the field direction.

force, which is generally true at room temperature.

If E is a DC field or is varying slowly, then the equation of motion Eq. 3.5 can be solved by integration under the assumption of a constant E, which gives the angular frequency

$$\omega_{\text{rot}}(t) = \sqrt{\frac{\Delta\alpha E^2}{2I}}\sqrt{\cos 2\theta(t) - \cos 2\theta_0}, \tag{3.6}$$

where $\theta(t_0) = \theta_0$ is the initial orientation angle of the molecule with respect to field direction, and $\theta(t)$ under adiabatic limit (slowly varying $E(t)$, i.e., $(dE/dt)/E \ll \dot{\theta}/\theta$) can be obtained by solving the elliptical integral. Note that we have assumed $\omega_{\text{rot}}(t_0) = 0$ for simplicity. In fact, Eq. 3.5 has the form $\propto \sin 2\theta(t)$ and is similar to the pendulum equation, which is $\propto \sin\theta(t)$. Hence the molecule undergoes pendulum oscillation in a quasi-static field, and the molecular axis periodically aligns along the field direction. Using small angle approximation, the oscillation period is

$$T_{\mathrm{rot}} = 2\pi\sqrt{\frac{I}{\Delta\alpha E^2}}, \tag{3.7}$$

and as expected, the molecule rotates faster with larger $\Delta\alpha$ and E, or smaller I. Also the temporal variation of E must be much slower than T_{rot} to make adiabatic limit valid.

On the other hand, if the external electric field turns on and off rapidly, such as the case of the linearly-polarized femtosecond laser pulse, the molecule could just rotate a small angle in the duration of the pulse. If this duration is much shorter than $2\pi/\omega_{\mathrm{rot}}$, the pulse can be approximated by a δ-function $E^2(t) = (8\pi/c)F\delta(t - t_0)$ with a finite fluence F, and the molecule can be regarded stationary when the laser pulse arrives. After the laser pulse is gone we obtain an angular velocity as a function of initial molecular orientation, with the magnitude

$$\omega_{\mathrm{rot}} = \frac{4\pi\Delta\alpha F}{cI}\sin 2\theta_0, \tag{3.8}$$

which is pointing toward $\hat{\boldsymbol{\phi}}'$ direction (azimuthal to the field direction $\hat{\mathbf{z}}'$) as shown in Fig. 3.1(a). In an ensemble of liquid or gas molecules at thermal equilibrium, the molecular orientation (θ_0, ϕ_0) is random at any moment before the presence of the laser pulse, with rotational kinetic energy distribution satisfying Maxwell-Boltzmann statistics. This extra angular velocity component $\omega_{\mathrm{rot}}\hat{\boldsymbol{\phi}}'$ introduced by the "kick" of the laser pulse makes the molecules rotate more preferably about axes lying on x'-y' plane on Fig. 3.1(a), namely, one may find the molecules have higher probability pointing toward the field direction $\hat{\mathbf{z}}'$ when taking a snapshot of the ensemble after the laser pulse is gone.

In the diatomic molecule, the two atoms are indistinguishable if they are the same species of isotope, so the molecules at angles θ and $(\pi - \theta)$ with respect to laser polarization are also indistinguishable. In this case, the molecular *alignment* rather than *orientation* is meaningful. The former is defined as the absolute angle $[0, \pi/2]$ between the external field direction and the most polarizable symmetry axis of the molecule, and the latter is defined in the similar way but with angular range $[0, \pi]$ and with consideration of swapping non-identical atoms. For instance, for the linear molecule N_2O, N-N-O and O-N-N are two different orientations but have the same alignment. To evaluate the statistical "degree" of molecular alignment in the system, average of the quantity $\cos^2\theta$ over all molecules at a specific time in the system is frequently used, which is denoted as $\langle\cos^2\theta\rangle_t$, with subscript t indicating the time dependence since the simple classical analysis above shows the aligning field imposes complex rotational dynamics on the molecules. This is not only a convenient definition satisfying the requirement of indistinguishable θ and $(\pi - \theta)$, but also an observable of the quantum mechanical system, which can be easily measured and will be discussed later in this chapter. Note that it is also possible to measure the orientation $\langle\cos\theta\rangle_t$ for polar molecules, i.e., those who do not have reflection symmetry about the rotation axis, using non-optical methods such as Coulomb explosion [91].

At thermal equilibrium in the system, the molecular orientation is random, then the ensemble average

$$\langle \cos^2\theta \rangle_t = \frac{1}{2\pi}\int_0^{2\pi} d\phi \int_0^{\frac{\pi}{2}} \cos^2\theta \sin\theta d\theta = \frac{1}{3} \tag{3.9}$$

is obtained by integrating over 2π solid angle or the upper unit hemisphere and is a constant at any time. This is justified by the ergodic hypothesis, that ensemble averages of random systems can be computed as averages over coordinates. The value 1/3 is the baseline when there is no net alignment in the ensemble, therefore we can formally define the degree of alignment as $\langle \cos^2\theta \rangle_t - 1/3$. The system at some instance $t = t_0$ is said to have some degree of "alignment" when $\langle \cos^2\theta \rangle_{t=t_0} - 1/3 > 0$, and to have some degree of "anti-alignment" when $\langle \cos^2\theta \rangle_{t=t_0} - 1/3 < 0$. The maximum degree of alignment has the value 2/3 and occurs when every molecule in the ensemble is aligned along the field direction. On the contrary, the maximum degree of anti-alignment is $-1/3$, and happens when the molecules are all perpendicular to the field direction.

Various laser cooling and optical trapping techniques (for example, Refs. [92, 93, 94]) have been developed to spatially confine or translate atoms, molecules and small objects such as cells and have wide applications. Similarly, manipulating alignment or orientation of molecules is also of great interest. Unlike the single atom, the molecule generally does not have spherical symmetry, and it is naturally to expect that its chemical and physical properties are orientation- (alignment-) dependent. Take two chemical reactions related to methyl iodide $Cl^- + CH_3I \rightarrow CH_3Cl + I^-$ and $Rb + CH_3I \rightarrow RbI + CH_3$ for example. The former most probably occurs when the Cl^- ion collides the CH_3I molecule at the methyl functional group side [95], and the latter happens preferably when the Rb atom approaches the iodide end of the molecule [96]. One can maximize the rate for different reactions by selecting the proper molecular orientation. In Atomic, molecular, and optical (AMO) physics and high harmonic generation (HHG), laser alignment helps to study some fundamental problems such as angular dependence of optical ionization rate [97] and alignment-controlled high harmonic generation [98] of linear molecules. Moreover, interference of electron de Broglie waves during the recombination process in laser-aligned and ionized CO_2 molecule is observed via HHG [99]. Other important contributions with the aid of laser alignment include tomographic reconstruction of molecular orbitals [100] and electron charge localization in H_2 and D_2 molecules during the photoionization by attosecond pulses [101].

3.2 Transient refractive index arises from molecular alignment

In a system of gaseous linear molecules at thermal equilibrium, the molecules are randomly oriented. At macroscopic scale the system is isotropic because the anisotropic polarizability from each molecule is averaged out. However birefringence can occur when some degree of alignment emerges in the system. To show this, we start from the dielectric response tensor in a gas sample

$$\boldsymbol{\epsilon} = 1 + 4\pi \langle \boldsymbol{\chi} \rangle_t = 1 + 4\pi N \langle \boldsymbol{\alpha} \rangle_t, \tag{3.10}$$

where N is the number density of the molecules, $\langle \boldsymbol{\alpha} \rangle_t$ is the time-dependent ensemble average of the second rank molecular polarizability tensor $\boldsymbol{\alpha}$, and the induced dipoles on each molecule is assumed to have no interaction with each other. Then the index of refraction becomes

$$n^2 = 1 + 4\pi N \langle \hat{\mathbf{e}} \cdot \boldsymbol{\alpha} \cdot \hat{\mathbf{e}} \rangle_t, \tag{3.11}$$

with

$$\langle \hat{\mathbf{e}} \cdot \boldsymbol{\alpha} \cdot \hat{\mathbf{e}} \rangle_t = \langle \sum_i \sum_j e_i \alpha_{ij} e_j \rangle_t \equiv \langle e_i \alpha_{ij} e_j \rangle_t. \tag{3.12}$$

Here, $\hat{\mathbf{e}}$ is the optical field polarization, and for simplicity the summation signs are omitted. This Einstein summation convention for repeated indices will be used throughout this Dissertation. The refractive index is in the form of Eq. 3.11 because the induced polarization is not necessarily in the same direction of the electric field. One has to find the projection of $\mathbf{P}$ onto $\mathbf{E}$ to obtain the refractive index along the field polarization direction.

For a linear molecule, where we choose the body-fixed axis z to be along the molecular axis as shown in Fig. 3.1, the polarizability tensor can be diagonalized:

$$\boldsymbol{\alpha} = \begin{bmatrix} \alpha_{xx} & 0 & 0 \\ 0 & \alpha_{yy} & 0 \\ 0 & 0 & \alpha_{zz} \end{bmatrix} = \begin{bmatrix} \alpha_{\perp} & 0 & 0 \\ 0 & \alpha_{\perp} & 0 \\ 0 & 0 & \alpha_{\parallel} \end{bmatrix}. \tag{3.13}$$

Owing to molecular symmetry about the z-axis, the optical electric field can be taken as $\mathbf{E} = \hat{\mathbf{x}} E_x + \hat{\mathbf{z}} E_z$ for a particular molecular orientation. Therefore, for an ensemble of molecular orientations in the space-fixed field, $n^2 = 1 + 4\pi N(\langle e_x^2 \rangle_t \alpha_{xx} + \langle e_z^2 \rangle_t \alpha_{zz})$, or

$$n^2(t) = 1 + 4\pi N \left(\Delta\alpha \langle \cos^2\theta \rangle_t + \alpha_\perp \right), \tag{3.14}$$

where $\Delta\alpha = \alpha_\parallel - \alpha_\perp$ and $e_z = \hat{\mathbf{e}} \cdot \hat{\mathbf{z}} = \cos\theta$ is the cosine of the angle between the molecular (z) axis and the electric field. Since $4\pi N \Delta\alpha \ll 1$ in a molecular gas, this allows an approximation of index shift

$$\Delta n(t) = \frac{2\pi N}{n_0} \Delta\alpha \left(\langle \cos^2\theta \rangle_t - \frac{1}{3} \right), \tag{3.15}$$

where we have used the fact $\langle \cos^2\theta \rangle_{t=-\infty} = 1/3$ and $n^2(t = -\infty) = n_0^2 = 1 + 4\pi N(\Delta\alpha/3 + \alpha_\perp)$ when the molecules initially have random orientations prior to the presence of the aligning field.

The discussion of transient refractive index here has followed the same coordinate convention as field alignment in Sec. 3.1, so Eq. 3.15 can be directly applied to a linearly-polarized aligning laser pulse itself, or to a following weak "probe" pulse with the same polarization. Measuring this transient shift of refractive index using a probe laser directly leads to the information of alignment in the molecular gas sample, which will be the topic of Chapter 4. Note that If the probe pulse polarization is perpendicular to the aligning "pump" pulse, it can be shown that the probe sees a different transient refractive index

$$\Delta n(t) = \frac{2\pi N}{n_0} \Delta\alpha \left(\frac{1}{2} \langle \sin^2\theta \rangle_t - \frac{1}{3} \right), \tag{3.16}$$

where $\langle \sin^2\theta \rangle_{t=-\infty} = 2/3$. This gives a result similar to Eq. 3.15 with half of the magnitude of the transient term, and its sign is flipped.

3.3 Quantum rigid rotor

In quantum mechanics, the molecular rotation is described by the rotational wavefunction of a free rigid rotor, which has the general form:

$$\Psi(t) = \sum_{j,m} a_{j,m} \left| j, m \right\rangle e^{-i(E_j/\hbar)t}, \tag{3.17}$$

with eigenenergies

$$E_j = \frac{\hbar^2 j(j+1)}{2I} \tag{3.18}$$

where I is the moment of inertia, j and m are integers satisfying $j \geq 0$ and $-j \leq m \leq j$. Each E_j corresponds to $2j+1$ degenerate J_z states labeled by m. Using the convention of rotational spectroscopy, $E_j = hcBj(j+1) = \hbar\omega_j$, where B is the rotational constant defined as $B = \hbar/(4\pi cI)$, and $\omega_j = 2\pi cBj(j+1)$.

The eigenfunctions $\left| j, m \right\rangle$ are the spherical harmonics

$$Y_j^m(\theta, \phi) = \sqrt{\frac{2j+1}{4\pi}\frac{(j-m)!}{(j+m)!}}(-1)^m e^{im\phi} P_j^m\left(\cos\theta\right), \tag{3.19}$$

where

$$P_j^m(x) = \frac{1}{2^j \cdot j!}\left(1 - x^2\right)^{m/2} \frac{d^{j+m}}{dx^{j+m}}\left(x^2 - 1\right)^j \tag{3.20}$$

is the associated Legendre function. Equation 3.19 is obtained from the eigenvalue problems of the pair of commuting operators J_z and J^2:

$$J_z Y(\theta,\phi) = \frac{h}{i}\frac{\partial}{\partial\phi} Y(\theta,\phi) = m\hbar Y(\theta,\phi) \tag{3.21}$$

and

$$J^2 Y(\theta,\phi) = -\hbar^2 \left[\frac{1}{\sin^2\theta}\frac{\partial^2}{\partial\phi^2} + \frac{1}{\sin\theta}\frac{\partial}{\partial\theta}\sin\theta\frac{\partial}{\partial\theta}\right] Y(\theta,\phi) = \hbar^2\lambda Y(\theta,\phi). \tag{3.22}$$

3.4 Density matrix formalism

For a system with a known pure quantum state $|\Psi\rangle$, such as a single rigid rotor, it is possible to obtain the expectation value, i.e., the quantum mechanical average of an observable Q of this state $\langle Q\rangle \equiv \langle\Psi|Q|\Psi\rangle$. The wavefunction representation of $|\Psi\rangle$ is $\Psi = \sum_j a_j |j\rangle$, a linear superposition of its eigenstates, where a_j is the complex amplitude satisfying $\sum_j |a_j|^2 = 1$. For a stationary state, $a_j = \alpha_j e^{i\phi_j} e^{-i(E_j/\hbar)t}$, where $0 \leq \alpha_j \leq 1$ is real, E_j is the eigenenergy of $|j\rangle$, and ϕ_j denotes the phase relation between each j state. It is possible to determine the quantum probability $|a_j|^2$ for all possible j states by performing measurements on many identically-prepared systems.

However, consider we have a mixture of N systems which are not necessarily initially identical, namely, each of them could be $\Psi_a = \sum a_j |j\rangle$, $\Psi_b = \sum b_j |j\rangle$, $\Psi_c = \sum c_j |j\rangle$, etc. If N is very large, for example, a 1-cm^3 gas sample at 1 atm pressure and room temperature which contains $\sim 10^{20}$ molecules, it is impossible to gain the full knowledge to this mixed state and explicitly write down the wavefunction.

Instead, we can specify the probability P_n of a molecule that is in the state $\Psi_n = a_{nj} \left| j \right\rangle$, with the constraint $\sum_n P_n = 1$. Note that P_n is the classical probability arising from lack of complete information of the system, which is different from the concept of quantum probability. The ensemble-averaged expectation value of an observable Q becomes

$$\begin{aligned}
\overline{\langle Q \rangle} &= \sum_n P_n \left\langle \Psi_n \right| Q \left| \Psi_n \right\rangle \\
&= \sum_n P_n \sum_{jk} a_{nj} a_{nk}^* \left\langle k \right| Q \left| j \right\rangle \\
&= \sum_{jk} \left\langle j \right| \left(\sum_n P_n a_{nj} a_{nk}^* \left| j \right\rangle \left\langle k \right| \right) \left| k \right\rangle \left\langle k \right| Q \left| j \right\rangle \\
&= \mathrm{Tr}\left(\rho Q\right),
\end{aligned} \tag{3.23}$$

where Tr denotes the trace of the matrix, and

$$\rho = \sum_{jk} \sum_n P_n a_{nj} a_{nk}^* \left| j \right\rangle \left\langle k \right| = \sum_n P_n \left| \Psi_n \right\rangle \left\langle \Psi_n \right| \tag{3.24}$$

is the density operator, with its matrix element

$$\rho_{jk} = \sum_n P_n a_{nj} a_{nk}^*. \tag{3.25}$$

The temporal evolution of density operator has the differential equation form

$$\frac{d\rho}{dt} = -\frac{i}{\hbar} \left[H, \rho\right], \tag{3.26}$$

where H is Hamiltonian of the system, [ ] is the commutator. For an ensemble of free rigid rotors without interaction with each other or with external electric field, $H = L^2/(2I) \equiv H_0$. Then the matrix representation of ρ, or density matrix, is given by

$$\rho = \sum_{j',j,m',m} \rho_{j',j}^{m',m} \left|j', m'\right\rangle\left\langle j, m\right| , \tag{3.27}$$

under the basis of angular momentum eigenstates $|j, m\rangle$. For simplicity we may use $|p\rangle \equiv |j', m'\rangle$ and $|q\rangle \equiv |j, m\rangle$ for now. The temporal evolution of each density matrix element becomes

$$\frac{d}{dt}\rho_{pq} = -\frac{i}{\hbar} \left\langle p\right| \left[H_0, \rho\right] \left|q\right\rangle = -i\omega_{pq}\rho_{pq}, \tag{3.28}$$

where we have used the definition $\hbar\omega_{pq} \equiv (E_p - E_q)$ for convenience.

If an external electric field is applied, then the interaction Hamiltonian becomes $H = H_0 + h_E$, where $h_E = -\frac{1}{2}\mathbf{p} \cdot \mathbf{E} - \boldsymbol{\mu} \cdot \mathbf{E}$ contains both induced and permanent dipole moments of the molecules for generality. Now the calculation of $\langle p| [h_E, \rho] |q\rangle = (h_E)_{pk}\rho_{kq} - \rho_{pk}(h_E)_{kq}$ with $(h_E)_{pk} = \langle p| h_E |k\rangle$ is involved. The matrix element of permanent and induced dipole terms in h_E are given by

$$\left(h_{\text{perm}}\right)_{pk} = -\mu E \left\langle p\right| \cos\theta \left|k\right\rangle , \tag{3.29}$$

and

$$\left(h_{\text{ind}}\right)_{pk} = -\frac{1}{2}E^2 \left[\Delta\alpha \left\langle p\right| \cos^2\theta \left|k\right\rangle + \alpha_{\perp} \left\langle p\right| 1 \left|k\right\rangle\right] , \tag{3.30}$$

respectively. One may identify that

$$\cos\theta = \sqrt{\frac{4\pi}{3}} Y_1^0(\theta,\phi), \tag{3.31}$$

and

$$\cos^2\theta = \frac{1}{3}\left[\sqrt{\frac{16\pi}{5}} Y_2^0(\theta,\phi) + 1\right]. \tag{3.32}$$

Employing the theory of addition of angular momenta [102]

$$\begin{aligned}\int \left(Y_j^m\right)^* Y_{j_1}^{m_1} Y_{j_2}^{m_2} d\Omega \\ = \sqrt{\frac{(2j_1+1)(2j_2+1)}{4\pi(2j+1)}} \langle j_1 j_2; 00 | j_1 j_2; j0\rangle \langle j_1 j_2; m_1 m_2 | j_1 j_2; jm\rangle ,\end{aligned} \tag{3.33}$$

where $\langle j_1 j_2; m_1 m_2 | j_1 j_2; jm\rangle$ is the Clebsch-Gordan coefficient for $|j_1 - j_2| \le j \le j_1 + j_2$ and $m = m_1 + m_2$, the matrix element of $\cos\theta$ and $\cos^2\theta$ can be calculated. Moreover, the selection rules are easily revealed from the Clebsch-Gordan coefficient $\langle j_1 j_2; 00 | j_1 j_2; j0\rangle$ in Eq. 3.33, which is nonzero only when $j - j_1 - j_2$ is even, using the symmetry relation $\langle j_1 j_2; m_1 m_2 | j_1 j_2; jm\rangle = (-1)^{j-j_1-j_2} \langle j_1 j_2; -m_1 - m_2 | j_1 j_2; j - m\rangle$ [103]. For permanent dipole moment only $j' = j \pm 1$ transitions with $m' = m$ are allowed, while $j' = j$ and $j' = j \pm 2$ with $m' = m$ are allowed for induced dipole moment. The selection rule $m' = m$ is due to the fact that the Hamiltonian h_E is not ϕ-dependent when the electric field is linearly polarized, therefore $\langle J_z\rangle$ is conserved since $d\langle J_z\rangle/dt \propto \langle [h_E, J_z]\rangle = 0$, where $J_z = -i\hbar\partial/\partial\phi$. Note that the matrix element $\langle p|\cos^2\theta|q\rangle$ can be viewed as a two-photon process $\sum_i \langle p|\cos\theta|i\rangle\langle i|\cos\theta|q\rangle$, where

$|i\rangle$ is a set of intermediate virtual states. This explains the selection rule too: the two photons induce two successive transitions $|q\rangle \rightarrow |i\rangle$ and $|i\rangle \rightarrow |p\rangle$, with coupling between j and $j \pm 1$ states for each. The overall possible j-state couplings are therefore $|j\rangle \rightarrow |j\rangle$ and $|j\rangle \rightarrow |j \pm 2\rangle$.

Defining $\langle j', m'| \cos^2\theta \,|j, m\rangle \equiv Q^m_{j'j}$ and $\langle j', m'| \cos\theta \,|j, m\rangle \equiv T^m_{j'j}$, we have

$$\begin{aligned} \frac{d\rho^m_{j'j}}{dt} = -i\omega_{j'j}\rho^m_{j'j} + \frac{i\Delta\alpha}{2\hbar}E^2\left(Q^m_{j'q}\rho^m_{qj} - \rho^m_{j'q}Q^m_{qj}\right) \\ + \frac{i\mu}{\hbar}E\left(T^m_{j'q}\rho^m_{qj} - \rho^m_{j'q}T^m_{qj}\right) + \left(\frac{d\rho^m_{j'j}}{dt}\right)_{\text{diss}}, \end{aligned} \tag{3.34}$$

where the last term on the right hand side represents a phenomenological dephasing term corresponding to collisions and spontaneous emission. Note that both $\cos\theta$ and $\cos^2\theta$ are Hermitian operators, so $(Q^m_{j'j})^* = Q^m_{jj'}$ and $(T^m_{j'j})^* = T^m_{jj'}$. Also note that we only label one m index because there is no coupling between each m state. Finally, either ensemble-averaged alignment or orientation of molecules is determined from

$$\mathrm{Tr}(\rho\cos^2\theta) = \sum_m \rho^m_{jk}Q^m_{kj}, \tag{3.35}$$

or

$$\mathrm{Tr}(\rho\cos\theta) = \sum_m \rho^m_{jk}T^m_{kj}, \tag{3.36}$$

with an additional summation over all m states.

If the electric field E is contributed by a femtosecond laser pulse $E(t) = E_0(t)\cos\omega t$, where $E_0(t)$ is the slowly varying envelope and ω is the carrier frequency, then it is the cycle average of the laser field dominating the field-molecule interaction, because the rotational response of the molecules is much slower than the fast oscillating optical field component. This results in inefficient coupling between the laser field and the molecular permanent dipole moment because $\langle \boldsymbol{\mu} \cdot \mathbf{E}(t) \rangle_{\text{cycle}} = 0$. At terahertz [104] to microwave [105] frequencies the response from the permanent dipole moment is more significant. On the other hand $\langle \mathbf{p} \cdot \mathbf{E}(t) \rangle_{\text{cycle}} \propto \frac{1}{2} E_0^2(t)$ for induced dipole moment, so we may replace the full temporal description $E^2(t)$ by the cycle average $\frac{1}{2} E_0^2(t)$ in Eq. 3.34. Note that femtosecond-laser-induced molecular orientation has also been demonstrated using two-color laser fields [91] or by combining a ultrashort laser pulse with a DC field [106].

The matrix elements Q_{jk}^m are calculated from either Eq. 3.33 or from directly performing the solid angle integration of the spherical harmonics. The nonzero elements are listed below:

$$Q_{j-2,j}^m = Q_{j,j-2}^m = \sqrt{\frac{(j^2 - m^2)}{(2j-1)^2} \frac{((j-1)^2 - m^2)}{(2j+1)(2j-3)}}, \tag{3.37}$$

$$Q_{jj}^m = \frac{-(j^2 - m^2)}{(2j-1)(2j+1)} + \frac{(j+1)^2 - m^2}{(2j+1)(2j+3)}, \tag{3.38}$$

$$Q_{j+2,j}^m = Q_{j,j+2}^m = \sqrt{\frac{((j+2)^2 - m^2)}{(2j+3)^2} \frac{((j+1)^2 - m^2)}{(2j+1)(2j+5)}}. \tag{3.39}$$

3.5 Partition function and consideration of symmetry

According to Eq. 3.25, the general form of the diagonal elements in the density matrix is $\rho_{jj} = \sum_n P_n |a_{nj}|^2$, which is the ensemble average of quantum probability for occupation of state j in the macroscopic system and therefore its meaning is apparent: it is the *population* at state j, which is connected to the macroscopic behavior of the system seen by an observer. For an ensemble of rigid rotors at thermal equilibrium and not subject to the external field ($H = H_0$), the population corresponding to eigenenergy E_j is $\sum_{m=-j}^{j} \rho_{jj}^m \equiv \rho_{jj}$, where a summation over degenerate m states is performed, and ρ_{jj} should obey Boltzmann distribution $\propto \exp(-E_j/k_B T)$, where k_B is Boltzmann constant and T is temperature. It is also required that $\sum_{j,m} \rho_{jj}^m = 1$ for normalization.

In statistical mechanics one may define a partition function Z for a many-body system at thermal equilibrium. The rotational partition function for heteronuclear diatomic molecules, or more generally, linear molecules without nuclear reflection symmetry about the rotation axis, is

$$Z = \sum_{j=0}^{\infty} (2j+1) e^{-hcBj(j+1)/k_B T}, \tag{3.40}$$

where $2j+1$ arises from counting the degenerate m states. The probability of being state j with rotational energy E_j is then given by

$$P(E_j) = \frac{(2j+1) e^{-hcBj(j+1)/k_B T}}{Z}. \tag{3.41}$$

Comparing with properties of the density matrix, one may find $\rho_{jj} = P(E_j)$.

For homonuclear diatomic molecules, however, calculating the partition function is tricky due to the quantum symmetry requirement imposed on the identical particles. That is, the *total* wavefunction of the molecule

$$\Psi_{\text{total}} = \Psi_{\text{tran}}\Psi_{\text{vib}}\Psi_{\text{elec}}\Psi_{\text{rot}}\Psi_{\text{nucl}}$$

should be either symmetric for Bosonic or anti-symmetric for Fermionic nuclei. The wavefunctions Ψ with subscripts trans, vib, elec, rot, and nucl denote translational, vibrational, electronic, rotational, and nuclear wavefunction, respectively. More precisely, Ψ_{total} has definite parity: the anti-symmetric wavefunction changes its sign under pairwise particle label exchange, i.e., $P(\Psi) = -\Psi$ with $P : (1, 2) \rightarrow (2, 1)$, where 1 and 2 are particle labels or coordinates, whereas $P(\Psi) = \Psi$ for the symmetric wavefunction. The translational wavefunction is $\Psi_{\text{tran}} \sim \exp(i\mathbf{p} \cdot \mathbf{r})$, where $\mathbf{p} = \mathbf{p_1} + \mathbf{p_2}$ and $\mathbf{r} = (\mathbf{r_1} + \mathbf{r_2})/2$, and the ground state vibrational wavefunction is $\Psi_{\text{vib}} \sim \exp(-(x_2 - x_1)^2/x_0^2)$, therefore Ψ_{tran} and Ψ_{vib} are invariant under nuclear exchange. Furthermore, most of the common homonuclear diatomic gases such as hydrogen, deuterium, and nitrogen have symmetric covalent bond electron wavefunctions Ψ_{elec} at their ground states, so the problem is reduced to parities of molecular rotation and total nuclear spin wavefunctions Ψ_{rot} and Ψ_{nucl}.

The spherical harmonics $Y_j^m(\theta, \phi)$ form a complete set of orthonormal basis of the rotational wavefunction, and it is easy to show that

$$\Psi_{\text{rot}} = Y_j^m(\pi - \theta, \phi + \pi) = (-1)^j Y_j^m(\theta, \phi) \tag{3.42}$$

under parity transformation, which is equivalent here to nuclear exchange for diatomic molecules. Finally, in the diatomic molecule with each nucleus of spin I possessing $2I+1$ possible M (I_z) states, there are $(2I+1)^2$ total spin eigenstates, with $I(2I+1)$ anti-symmetric and $(I+1)(2I+1)$ symmetric states [107]. This is given by counting the possible combination of nuclear spin states leading to an anti-symmetric total spin eigenstate $|M_i M_j\rangle - |M_j M_i\rangle$, where $1 \leq i < j \leq 2I+1$. Therefore the nuclear spin statistics force either odd rotational J states associated with $(2I+1)(2I)/2 = I(2I+1)$ anti-symmetric total nuclear spin states, or even J associated with $(I+1)(2I+1)$ symmetric total nuclear spin states for integer spin (Boson) nuclei (so that Ψ_{total} is symmetric), and vice versa for half-integer spin (Fermion) nuclei (so that Ψ_{total} is antisymmetric). For example, both ^{14}N and D (^{2}H) have nuclear spin $I = 1$ (Boson), so the statistical weighting factors of $^{14}\mathrm{N}_2$ and D_2 are 6 for even J and 3 for odd J values. Another example is H_2, in which each nucleus has half interger spin $I = \frac{1}{2}$ (Fermion), so the weighting factors are 1 for J_{even} and 3 for J_{odd}. Note that $I = 0$ for ^{16}O, however the ground state electron wavefunction of the $^{16}\mathrm{O}_2$ molecule is *anti-symmetric* [108], so only *odd* J rotational states can exist at the electronic ground state. To conclude, one may obtain a spin-statistics-weighted partition function for the homonuclear diatomic molecule:

$$Z = \sum_{j=0}^{\infty} D_j (2j+1) e^{-hcBj(j+1)/k_B T}, \tag{3.43}$$

where D_j is the statistical weighting factor previously discussed (for example, for

N_2, $D_{j,\text{even}} = 6$ and $D_{j,\text{odd}} = 3$), and

$$\rho_{jj}^{m} = \frac{D_j e^{-hcBj(j+1)/k_B T}}{Z}, \tag{3.44}$$

or

$$\rho_{jj} = \frac{D_j (2j+1) e^{-hcBj(j+1)/k_B T}}{Z}, \tag{3.45}$$

summing over the degenerate m states. This gives the initials values for Eq. 3.34.

3.6 Perturbation theory

Equation 3.34 now is able to be solved numerically, however it can consume a significant amount of computing power due to its potentially large matrix size. Here we try to use an approximation method to find a closed-form solution of ρ. Consider a femtosecond laser pulse interacting with a molecule without permanent dipole moment (the contribution of any permanent dipole moment cycle averages to zero in the optical field, leaving only the induced dipole), and assume $h_E \ll H_0$, the density matrix is calculated to first order in the optical perturbation $\rho(t) = \rho^{(0)} + \rho^{(1)}(t)$, where

$$\left(\rho^{(1)}(t)\right)_{kl} = -\frac{i}{\hbar}\int_{-\infty}^{t} d\tau \left[h_E, \rho^{(0)}\right]_{kl} e^{(i\omega_{kl}+\gamma_{kl})(\tau - t)}, \tag{3.46}$$

is the first order correction to the density matrix induced by the perturbation Hamiltonian $h_E = -\frac{1}{2}\mathbf{p}\cdot\mathbf{E}$, where $\mathbf{p} = \boldsymbol{\alpha}\cdot\mathbf{E}$ is the induced molecular dipole moment and $\mathbf{E}(\tau)$ is the laser field, whose pulse envelope peak is located at time $\tau = 0$. In Eq. 3.46, $\omega_{kl} = (E_k - E_l)/\hbar$ corresponds to rotational states $|k\rangle = |j, m\rangle$ and

$|l\rangle = |j', m'\rangle$ with energies $E_k = E_{j,m} = hcBj(j+1)$ and $E_l = E_{j',m'} = hcBj'(j'+1)$, γ_{kl} is the dephasing rate between states k and l, $\rho^{(0)}$ is the zeroth order density matrix describing a thermal equilibrium distribution of rotational states at $t = -\infty$. Use of first order perturbation theory is justified by the experimental results in Chapter 4 showing that $\langle\cos^2\theta\rangle_t$ deviates from the unperturbed $\langle\cos^2\theta\rangle_{t=-\infty} = 1/3$ by small amounts.

The commutator matrix element in Eq. 3.46 is $\left[h_E, \rho^{(0)}\right]_{kl} = (\rho_l^{(0)} - \rho_k^{(0)})(h_E)_{kl}$, where $\rho_l^{(0)} \equiv \rho_{ll}^{(0)}$ (no sum), $\rho_k^{(0)} \equiv \rho_{kk}^{(0)}$ (no sum), and

$$(h_E)_{kl} = -\frac{1}{2}\Delta\alpha\,|\mathbf{E}|^2\,(\langle k|\cos^2\theta\,|l\rangle - \alpha_\perp\delta_{kl}), \tag{3.47}$$

where δ_{kl} is the unity matrix. From Sec. 3.4 we know that the matrix element $\langle k|\cos^2\theta\,|l\rangle = \langle j,m|\cos^2\theta\,|j',m'\rangle$ is nonvanishing only for $m' = m$ and $j' = j \pm 2$ or $j' = j$. The non-coupling between different m states corresponds to the interaction symmetry about the molecular (z) axis (or conservation of angular momentum), while the j coupling corresponds to the two-photon non-resonant Raman excitation process which results in population of the spectrum of rotational states.

Following the same convention as in Sec. 3.4, $Q^m_{jj'} = \langle j,m|\cos^2\theta\,|j',m'\rangle$ and noting from above that $\left[h_E, \rho^{(0)}\right]_{kl}$ is nonvanishing only for the non-diagonal components $j' = j \pm 2$, Eq. 3.46 becomes

$$\begin{aligned}\rho^{m(1)}_{j,j-2}(t) = &-\frac{i\Delta\alpha}{2\hbar}\left(\rho_j^{m(0)} - \rho_{j-2}^{m(0)}\right)\\ &\times Q^m_{j,j-2}e^{-(\omega_{j,j-2}+\gamma_{j,j-2})t}\int_{-\infty}^{t} d\tau E^2(\tau)e^{(i\omega_{j,j-2}+\gamma_{j,j-2})\tau}\end{aligned} \tag{3.48}$$

where $\omega_{j,j-2} = (E_j - E_{j-2})/\hbar = 4\pi cB(2j-1)$ and $\rho_j^{m(0)}$ is defined in Eq. 3.44. Note that the equation for $\rho_{j,j+2}^{m(1)}$ is implicitly included in Eq. 3.48 since $\rho_{j,j+2}^{m(1)} = (\rho_{j+2,j}^{m(1)})^*$, which is equivalent to $\rho_{j-2,j}^{m(1)} = (\rho_{j,j-2}^{m(1)})^*$.

Finally, from Eq. 3.35, the ensemble-averaged alignment is

$$\begin{aligned}\left\langle \cos^2\theta \right\rangle_t &= \sum_m \rho_{kl}^m Q_{lk}^m|_{k=l} + \sum_m \rho_{kl}^m Q_{lk}^m|_{k\neq l} \\ &= \frac{1}{3} + \left[\rho_{j,j-2}^{m(1)} + \left(\rho_{j,j-2}^{m(1)}\right)^*\right] Q_{j,j-2}^m,\end{aligned} \tag{3.49}$$

or

$$\begin{aligned}\left\langle \cos^2\theta \right\rangle_t = \frac{1}{3} - \frac{\Delta\alpha}{\hbar}\Bigg[&\sum_{j,m}\left(\rho_j^{m(0)} - \rho_{j-2}^{m(0)}\right)\left(Q_{j,j-2}^m\right)^2 \\ &\times \mathrm{Im}\left(e^{(i\omega_{j,j-2}-\gamma_{j,j-2})t}\int_{-\infty}^{t} d\tau E^2(\tau) e^{(-i\omega_{j,j-2}+\gamma_{j,j-2})\tau}\right)\Bigg],\end{aligned} \tag{3.50}$$

where we have used the facts that $\sum_m Q_{jj}^m = 1/3$, and $Q_{j,j-2}^m = (Q_{j,j-2}^m)^* = Q_{j-2,j}^m$ is real. Summing Eq. 3.50 from $m = -j$ through $m = j$ eliminates m to yield

$$\begin{aligned}\left\langle \cos^2\theta \right\rangle_t = \frac{1}{3} - \frac{2\Delta\alpha}{15\hbar}\Bigg[&\sum_j \frac{j(j-1)}{2j-1}\left(\frac{\rho_j^{(0)}}{2j+1} - \frac{\rho_{j-2}^{(0)}}{2j-3}\right) \\ &\times \mathrm{Im}\left(e^{(i\omega_{j,j-2}-\gamma_{j,j-2})t}\int_{-\infty}^{t} d\tau E^2(\tau) e^{(-i\omega_{j,j-2}+\gamma_{j,j-2})\tau}\right)\Bigg],\end{aligned} \tag{3.51}$$

where $\rho_j^{(0)} = (2j+1)\rho_j^{m(0)}$, and we have used the relation

$$\sum_m \left(Q_{j,j-2}^m\right)^2 = \frac{2}{15}\frac{j(j-1)}{2j-1}. \tag{3.52}$$

Again, for a femtosecond laser pulse, only the cycle-averaged field torques the molecules significantly. The laser field is taken to be $\mathbf{E}(t) = \hat{\mathbf{e}}\varepsilon(t)(e^{i\omega t} + e^{-i\omega t})/2$, where ω is the optical carrier frequency and $\varepsilon(t)$ is the slowly varying field envelope whose temporal width is much greater than $2\pi/\omega$. Therefore $\langle E^2(t)\rangle_{\text{cycle}} = \frac{1}{2}\varepsilon^2(t)$ is the cycle average and should be plugged into Eqs. 3.50 and 3.51.

Several special cases can be calculated. For a delta-function pump pulse having a fluence F (in erg/cm^2), $\varepsilon^2(\tau) = (8\pi/c)F\delta(\tau)$ and Eq. 3.51 becomes

$$\left\langle \cos^2\theta \right\rangle_t = \frac{1}{3} - \frac{8\pi\Delta\alpha F}{15\hbar c}\left[\sum_j \frac{j(j-1)}{2j-1}\left(\frac{\rho_j^{(0)}}{2j+1} - \frac{\rho_{j-2}^{(0)}}{2j-3}\right)e^{-\gamma_{j,j-2}t}\sin\left(\omega_{j,j-2}t\right)\right]. \tag{3.53}$$

This case models an extremely short pump pulse with wide bandwidth. For a Gaussian pump pulse with temporal full width at half maximum (FWHM) τ_p and peak field amplitude E_0, and for times $t \gg \tau_p$, the upper limit of the integral in Eq. 3.51 can be taken to infinity yielding

$$\begin{aligned}\left\langle \cos^2\theta \right\rangle_t = \frac{1}{3} - \sqrt{\frac{\pi}{\ln 2}}\frac{\Delta\alpha\tau_p E_0^2}{15\hbar}\Bigg[\sum_j \frac{j(j-1)}{2j-1}\left(\frac{\rho_j^{(0)}}{2j+1} - \frac{\rho_{j-2}^{(0)}}{2j-3}\right) \\ \times e^{-(\omega_{j,j-2}^2-\gamma_{j,j-2}^2)\tau_p^2/(16\ln 2)}e^{-\gamma_{j,j-2}t}\sin\left(\omega_{j,j-2}t - \frac{\gamma_{j,j-2}\omega_{j,j-2}\tau_p^2}{8\ln 2}\right)\Bigg].\end{aligned} \tag{3.54}$$

Both Eqs. 3.53 and 3.54 are appropriate for examining the alignment response for times well after the laser pulse. For the alignment response during and immediately after the pump pulse, a simple expression can be obtained by assuming a laser envelope of the form $\varepsilon^2(\tau) = E_0^2 \cos^2\left(\frac{\pi}{2}\frac{\tau}{\tau_0}\right)$ for $|\tau| \leq \tau_0$ and $\varepsilon^2(\tau) = 0$ for $|\tau| > \tau_0$, with FWHM duration τ_0. For times $|\tau| \leq \tau_0$, Eq. 3.51 becomes

$$\begin{aligned}\left\langle \cos^2\theta \right\rangle_t = \frac{1}{3} - \frac{\Delta\alpha E_0^2}{15\hbar} \sum_j \frac{j(j-1)}{2j-1} \left(\frac{\rho_j^{(0)}}{2j+1} - \frac{\rho_{j-2}^{(0)}}{2j-3} \right) \Big[a_1 + (a_2 + a_3) \cos(\pi t/\tau_0) \\ + (a_4 - a_5) \sin(\pi t/\tau_0) + (a_4 + a_5 - a_6) e^{-\gamma_{j,j-2}(t+\tau_0)} \sin(\omega_{j,j-2}(t+\tau_0)) \\ + (-a_1 + a_2 + a_3) e^{-\gamma_{j,j-2}(t+\tau_0)} \cos(\omega_{j,j-2}(t+\tau_0)) \Big],\end{aligned} \tag{3.55}$$

and for $|\tau| > \tau_0$ it becomes

$$\begin{aligned}\left\langle \cos^2\theta \right\rangle_t = \frac{1}{3} - \frac{\Delta\alpha E_0^2}{15\hbar} \sum_j \frac{j(j-1)}{2j-1} \left(\frac{\rho_j^{(0)}}{2j+1} - \frac{\rho_{j-2}^{(0)}}{2j-3} \right) \\ \times \Big[(a_6 - a_4 - a_5) e^{-\gamma_{j,j-2}(t-\tau_0)} \sin(\omega_{j,j-2}(t-\tau_0)) \\ + (-a_6 + a_4 + a_5) e^{-\gamma_{j,j-2}(t+\tau_0)} \sin(\omega_{j,j-2}(t+\tau_0)) \\ + (a_1 - a_2 - a_3) e^{-\gamma_{j,j-2}(t-\tau_0)} \cos(\omega_{j,j-2}(t-\tau_0)) \\ + (-a_1 + a_2 + a_3) e^{-\gamma_{j,j-2}(t+\tau_0)} \cos(\omega_{j,j-2}(t+\tau_0)) \Big],\end{aligned} \tag{3.56}$$

where

$a_1 = \frac{1}{2}\omega_{j,j-2} / \left(\gamma_{j,j-2}^2 + \omega_{j,j-2}^2\right)$,

$a_2 = \frac{1}{4}\left(\omega_{j,j-2} - \pi/\tau_0\right) / \left(\gamma_{j,j-2}^2 + \left(\omega_{j,j-2} - \pi/\tau_0\right)^2\right)$,

$a_3 = \frac{1}{4}\left(\omega_{j,j-2} + \pi/\tau_0\right) / \left(\gamma_{j,j-2}^2 + \left(\omega_{j,j-2} + \pi/\tau_0\right)^2\right)$,

$a_4 = \frac{1}{4}\gamma_{j,j-2} / \left(\gamma_{j,j-2}^2 + (\omega_{j,j-2} - \pi/\tau_0)^2\right),$

$a_5 = \frac{1}{4}\gamma_{j,j-2} / \left(\gamma_{j,j-2}^2 + (\omega_{j,j-2} + \pi/\tau_0)^2\right),$

$a_6 = \frac{1}{2}\gamma_{j,j-2} / \left(\gamma_{j,j-2}^2 + \omega_{j,j-2}^2\right).$

3.7 Discussion

The meaning of the diagonal density matrix element ρ_{jj} is the population, which has been discussed in Sec. 3.5. On the other hand, the off-diagonal term of the density matrix $\rho_{jk} = \sum_n P_n a_{nj} a_{nk}^* = \sum_n P_n |a_{nj}||a_{nk}| \exp\left(i(\phi_{nj} - \phi_{nk})\right)$ gives the *coherence* between two states j and k in the ensemble. If the relative phase $\phi_{nj} - \phi_{nk}$ for each of the possible n states (for $j \neq k$) in the ensemble is indeterminate, then $\rho_{jk} = 0$, corresponding to have no coherence between j and k, which is the case for a collection of air molecules in thermal equilibrium.

Now we can see deeper insight of results derived in Sec. 3.4 and 3.6. For simplicity we neglect the relaxation parameter γ introduced in Eq. 3.46 for now. Equation 3.48 shows that under the first order approximation the laser pulse "locks" the relative phases among all the odd-j and among all the even-j rotational eigenfunctions, and this coherent excitation is proportional to the population difference between states j and $j-2$. As long as ordered initial phase relations between many rotational eigenfunctions are created from randomness, and the eigenfunctions evolve according to temporal phase $\exp\left(-i(E_j/\hbar)t\right)$, their superposition forms a wavepacket $|\Psi\rangle = \sum_{j,m} |a_{j,m}| e^{i\phi_{j,m}} |j,m\rangle\, e^{-i\omega_j t}$, where $\omega_j = E_j/\hbar = 2\pi c B j(j+1)$, and $\phi_{j,m}$ is the phase of $a_{j,m}$. The absolute square of this wavepacket is a train of sharp amplitude spikes on time axis at some repetition rate which will be apparent shortly, due to the fact that the rotational levels (energies and frequencies) are quantized. The train of spikes can last for very long time compared with the laser pulse duration and decays due to collision. The last term in Eq. 3.48 $\int_{-\infty}^{t} d\tau E^2(\tau)e^{i\omega_{j,j-2}\tau}$ represents the initial influence of the laser electric field which is analogous to the classical torque impulse applied to the molecules. Note that for times t after the laser pulse is gone, the upper limit of the integral can be replaced by $+\infty$, which makes it Fourier transform of $E^2(\tau)$ of the laser pulse. Therefore the maximum degree of coherence $\rho^m_{j,j-2}$ after the laser pulse is proportional to not only $\rho_j^{m(0)} - \rho_{j-2}^{m(0)}$ but also the spectral intensity $\widetilde{I}(\omega_{j,j-2})$. Note that to the first order approximation the laser pulse excitation does not alter the population, so we may drop the superscript (0) from $\rho_j^{m(0)}$ for the following discussions.

The effect of finite bandwidth of laser pulse will be discussed later. Here, for further simplification we consider the impulse response of the molecular rotation by modeling the laser pulse as a delta function located at $t = 0$ in Eq. 3.48. At $t = 0$ all temporal phase components $e^{-i\omega_j t}$ in the wavepacket are in phase. Note that the coherent spike of the wavepacket actually arises at a time t_{peak} *later* due to the extra constant relative phase $\phi_{j,m} - \phi_{j-2,m} = -\pi/2$ between $|j, m\rangle$ and $|j-2, m\rangle$ coming from the factor of $-i$ in Eq. 3.48, which is the consequence of the rotational inertia effect. As $|\Psi\rangle$ evolves further in time each $|j, m\rangle$ state advances with its own phase factor $\exp(-i\omega_j t)$, so that a sum over a large number of states tends to result in rapid cancellation. However, when time passes through values $t = qT_{\text{rev}}$, where q is an integer and $T_{\text{rev}} = 2\pi/\omega_1 = (2cB)^{-1}$, the phases become $\omega_j t = q\pi j(j+1)$, an integer multiple of 2π, causing a "full revival": all the wavepacket's constituent states are rephased to their initial values at $t = 0$, and produce another coherent spike at $T_{\text{rev}} + t_{\text{peak}}$, with $t_{\text{peak}} \ll T_{\text{rev}}$ in general. There also exist "partial revivals" at specific fractions of T_{rev}. When $t = q(T_{\text{rev}}/2)$ and q is odd ("half-revival"), $\omega_j t = q\pi j(j+1)/2$. This puts the two sets of states with $j(j+1)/2$ even ($j = 0, 3, 4, 7, 8, 11, 12, \cdots$) and with $j(j+1)/2$ odd ($j = 1, 2, 5, 6, 9, 10, \cdots$) separately in phase, with a phase difference of π. These two sets of j states interfere with each other, leading to different shape of temporal coherence from the full revival case. Partial revivals can also occur at times $T_{\text{rev}}/4$, $T_{\text{rev}}/8$, $T_{\text{rev}}/16$, etc., because $j(j+1)$ is even. For quarter revivals at $t = q(T_{\text{rev}}/4)$ with odd q, there are four sets of rotational states separately in phase. When $q = 1, 5, 9, \cdots = 4n + 1$ where n is an integer, the four sets of states with their relative phases in the parentheses are $j = 0, 7, 8, \cdots$ (0), $j = 1, 6, 9, \cdots$ $(\pi/2)$, $j = 3, 4, 11, 12, \cdots$ (π), and $j = 2, 5, 10, \cdots$ $(3\pi/2)$. When $q = 3, 7, 11, \cdots = 4n + 3$ the sets of j states and their relative phases become $j = 0, 7, 8, \cdots$ (0), $j = 2, 5, 10, \cdots$ $(\pi/2)$, $j = 3, 4, 11, 12, \cdots$ (π), and $j = 1, 6, 9, \cdots$ $(3\pi/2)$. This causes different behaviors of the wavepacket at around $(n + 1/4)T_{\text{rev}}$ and $(n + 3/4)T_{\text{rev}}$. Fractional revivals at shorter intervals than $T_{\text{rev}}/4$ are difficult to observe, because they contain more subsets of in-phase states possessing different relative phases. These subsets tend to cancel each other and thus the wavepacket amplitude is much weaker. The peak amplitude of partial revivals also depends on nuclear spin statistics discussed in Sec. 3.5.

The ensemble-averaged molecular alignment $\langle \cos^2\theta \rangle_t - 1/3$ is the measurable quantity of the system rather than the rotational wavepacket itself. The calculated

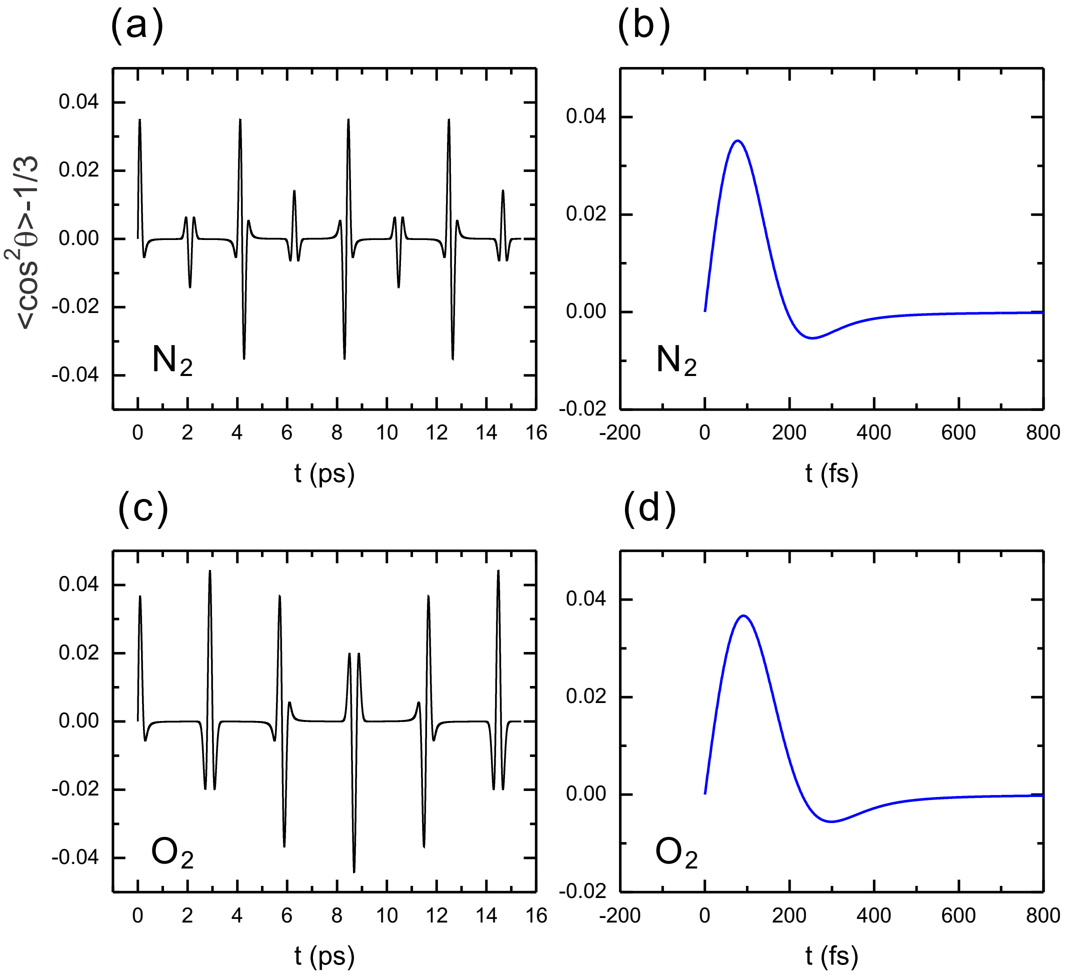

Figure 3.2: Calculated molecular alignment at $T = 300$ K excited by a delta-function laser pulse with 1 J/cm^2 fluence and successive quarter-, half-, and full-revivals in (a) N_2 and (c) O_2. The full-revival periods are $T_{\mathrm{rev},N_2} = 8.33$ ps for N_2 and $T_{\mathrm{rev},O_2} = 11.59$ ps for O_2, respectively. Panels (b) and (d) are details of (a) and (c) from 0 to 800 fs.

impulse responses of $^{14}N_2$ and $^{16}O_2$ molecular alignment from Eq. 3.53 are shown in Fig 3.2(a) and 3.2(c), respectively, from $t = 0$ to 16 ps. It can be seen that the first alignment peak occurs at $t_{\mathrm{peak},N_2} = 77$ fs for N_2 in Fig. 3.2(b) and at $t = t_{\mathrm{peak},O_2} = 91$ fs for O_2 in Fig. 3.2(d) due to the slow rotational response of molecules (compared with orbital electrons) to the laser field. Moreover, the alignment is proportional to the superposition of $\sin(\omega_{j,j-2}t)$ over many j levels, with $\omega_{j,j-2} = (E_j - E_{j-2})/\hbar = 4\pi cB(2j-1)$ and a fixed frequency spacing $\Delta\omega = \omega_{j+1,j-1} - \omega_{j,j-2} =$

$8\pi cB$. Therefore the full revival period of the alignment occurs at times $\frac{1}{2}\Delta\omega t = q2\pi$, or $t = qT_{\mathrm{rev}}$, where $\frac{1}{2}\Delta\omega = 2\pi/T_{\mathrm{rev}} = \Omega_{\mathrm{rev}}$ is the fundamental beating frequency, and this agrees with the observation of $\rho^m_{j,j-2}$ from Eq. 3.48. The calculated full revival periods of N_2 and O_2 are $T_{\mathrm{rev},N_2} = 8.33$ ps and $T_{\mathrm{rev},O_2} = 11.59$ ps, respectively.

Note that Eq. 3.53 has the form $\sum_p f(p)\sin\left((2p+1)\Omega_{\mathrm{rev}}t\right)$ with $p = 1, 2, 3, \cdots$ when $\gamma_{j,j-2}$ and the DC term 1/3 are neglected, and $(2p+1)\Omega_{\mathrm{rev}}t = \pi$ for each p when $t = qT_{\mathrm{rev}}/2$ and q is odd, which is called "half-revival" and can be seen in Fig 3.2. At half-revivals all the frequency components in Eq.3.53 have a π phase shift compared with those at full-revivals, therefore the alignment peaks near the half-revivals have the same shape as those near the full-revivals except that their signs are flipped. There also exist "quarter-revivals": at $t = (4n+1)T_{\mathrm{rev}}/4$ with $n = 0, 1, 2, \cdots$, the phases of the sinusoidal functions in Eq. 3.53 are $\pi/2$ for odd j and $-\pi/2$ for even j; at $t = (4n+3)T_{\mathrm{rev}}/4$, the phases are $-\pi/2$ for odd j and $\pi/2$ for even j instead. As discussed in Sec. 3.5, the population ratio of odd-j to even-j states $\rho^m_{j,\mathrm{odd}} : \rho^m_{j,\mathrm{even}}$ is $1:2$ for N_2 and $1:0$ for O_2. Therefore in N_2, the molecular alignment contributed by even-j states is partially cancelled by the contribution of odd-j states near the quarter-revivals, resulting to lower degree of alignment (or anti-alignment) than that near half- and full-revivals. Because O_2 only has odd j levels, there is no such cancellation effect near the quarter-revivals, so the alignment (anti-alignment) is larger than N_2. Also as shown in Fig. 3.2, the alignment quarter-revivals near $t = (4n+1)T_{\mathrm{rev}}/4$ and near $t = (4n+3)T_{\mathrm{rev}}/4$ have opposite signs, which is again the consequence of sign flipping of sinusoidal functions in Eq. 3.53. In Chapter 4 we will encounter N_2O, a linear molecule without reflection symmetry about its rotational axis. The nuclear spin statistics is no longer a concern, so $\rho_{j,\mathrm{odd}}^m : \rho_{j,\mathrm{even}}^m = 1 : 1$ and thus the quarter-revivals of alignment does not exist.

The width of alignment or anti-alignment ($\langle\cos^2\theta\rangle_t - 1/3$) peaks is determined by the number of rotational states contributing to the wavepacket. Similar to the idea of a mode-locked laser pulse, which has shorter duration with broader bandwidth (larger number of constituting longitudinal optical modes), the peak width of alignment is approximately $\sim T_{\mathrm{rev}}/N_{\mathrm{rot}}$, where N_{rot} is the number of rotational states contributing to the wavepacket, which is a function of temperature and pump pulse duration (bandwidth). For impulse excitation, N_{rot} is determined by thermal population of the rotational states, which can be seen as the dependence on $\sum_m(\rho_j^{m(0)} - \rho_{j-2}^{m(0)})(Q_{j,j-2}^m)^2$ for each j in Eq. 3.50. The population ρ_j at $T = 300$ K for N_2 and O_2 are shown in Figs. 3.3(a) and 3.3(b), respectively, with ρ_j^m shown in the insets. Their contributions to the molecular alignment in both gases, in terms of amplitudes of constituent frequency components $\omega_{j,j-2}$, are also shown in Figs. 3.3(c) and 3.3(d). For finite-bandwidth excitation, N_{rot} is further limited by the pulse duration, which is evident from the term $\exp\left(-\omega_{j,j-2}^2\tau_p^2/(16\ln 2)\right)$ for each j (neglecting $\gamma_{j,j-2}$) in Eq. 3.54, where τ_p is the pump pulse duration. Therefore when the rotational thermal distribution bandwidth $\Delta\omega_{\mathrm{rot}}$ is larger than the laser pulse envelope bandwidth, for those frequencies $\omega_{j,j-2} > (16\ln 2)\tau_p^{-1}$ their contributions to the wavepacket are less significant than those excited by the delta-function pulse, resulting in wider width of alignment (anti-alignment) peaks. This will be discussed in detail along with experimental results in Chapter 4.

The location of the first alignment peak t_{peak} excited by the laser pulse can

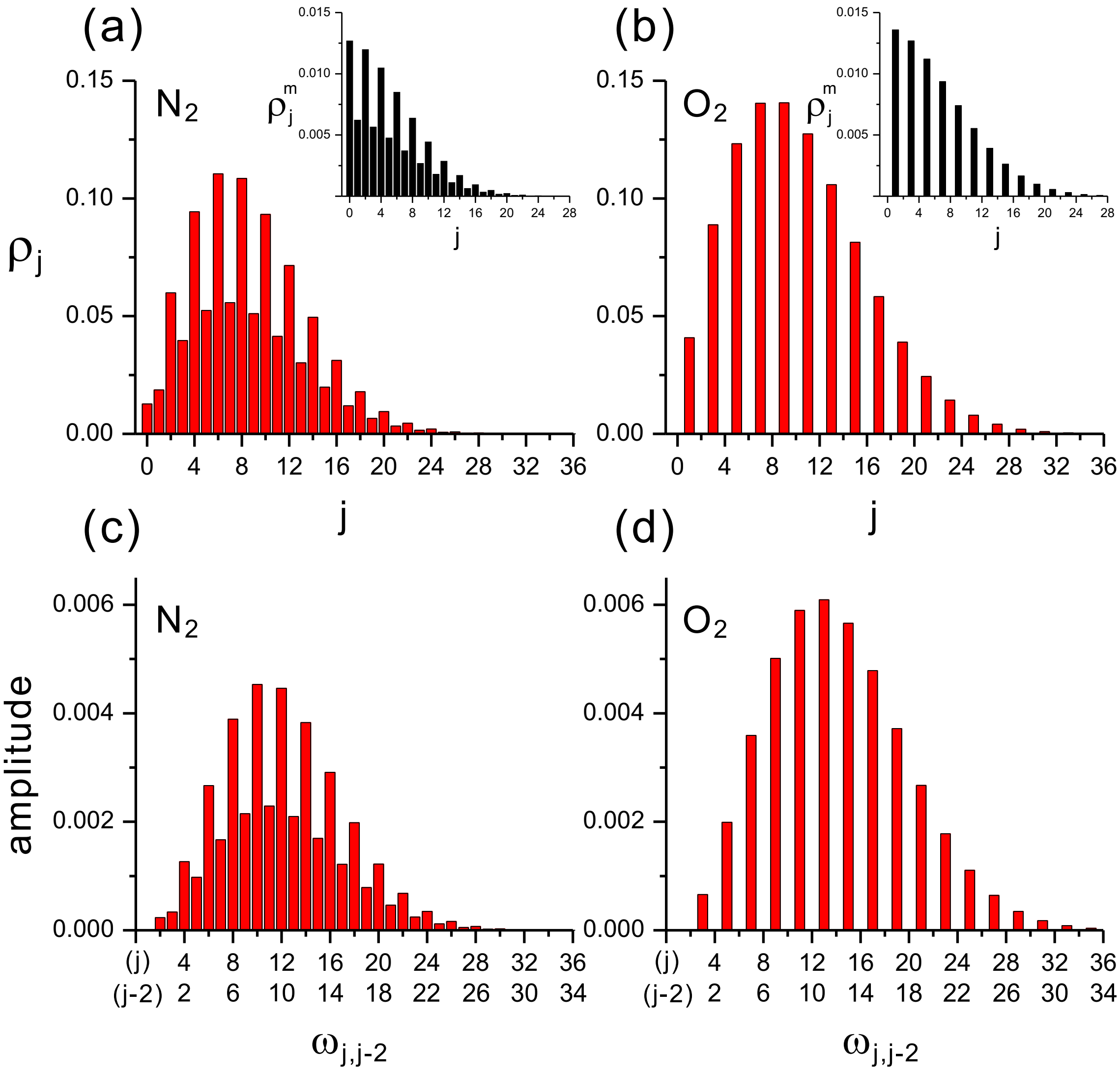

Figure 3.3: Thermal populations of the rotational states $\rho_j = (2j+1)\rho_j^m$ at $T = 300$ K in (a) N_2 and (b) O_2, with corresponding ρ_j^m shown in the insets, and calculated spectral amplitudes for each $\omega_{j,j-2}$ contributing to the molecular alignment in (c) N_2 and (d) O_2, excited by the same 1 J/cm^2 delta-function pulse as in Fig. 3.2.

Table 3.1: Selected linear molecular parameters $\Delta\alpha$ and rotational constant B from Ref. [109]. T_{rev} is calculated from $(2cB)^{-1}$.

Molecule	$\Delta\alpha$ (10^{-25} cm^3)	B (cm^{-1})	T_{rev} (ps)
N_2	9.3	2.001	8.33
O_2	11.4	1.438	11.59
N_2O	27.9	0.4116	40.49
D_2	2.92	29.90	0.557
H_2	3.02	59.30	0.281

be also estimated. Realizing that Eq. 3.53 can be approximated into the form $\sin\omega_c t \sum_n f(n)\cos(n\Delta\omega t)$ with $n = 0, 1, 2, \cdots$, where $\omega_c \gg \Delta\omega = 8\pi cB$ is the "center frequency" of the alignment spectral component. The first maximum occurs slightly earlier than $t = \pi/(2\omega_c)$ due to the modulation of $\sum_n f(n)\cos(n\Delta\omega t)$ over the more rapid-varying $\sin\omega_c t$, and thus we can regard this as the upper limit of t_{peak}. From Figs. 3.3(c) and 3.3(d), ω_c is found to be at $(j, j-2) = (11, 9)$ for N_2 and $(13, 11)$ for O_2, therefore $t_{\mathrm{peak},N_2} \sim T_{\mathrm{rev},N_2}/84 = 100$ fs and $t_{\mathrm{peak},O_2} \sim T_{\mathrm{rev},O_2}/100 = 116$ fs, which is close to the observation from Fig. 3.2(b) and 3.2(d). The parameters $\Delta\alpha$, B and T_{rev} for selected linear molecules are listed in Table 3.1 and will be used throughout this Dissertation.

Chapter 4

Measurement of rotational wave packet revivals of linear gas molecules

4.1 Introduction

Alignment of molecules has applications in a wide variety of fields including chemistry, molecular physics, and high harmonic generation mentioned in Sec. 3.1. Furthermore, molecular alignment in intense laser fields exhibits periodic revival structures, shifting the refractive index in proportional to the degree of alignment, as discussed in Chapter 3. A wake of refractive index echoes following an intense femtosecond pump pulse is produced in the gas medium, which serves as an ultrafast phase modulator for another co-propagating laser pulse later in time. When the delay between the two pulses is appropriately tuned, the second pulse spectrum can be significantly broadened [110, 111, 112, 113]. Compression of such spectrally-broadened pulse is also demonstrated by introducing dispersive material after phase modulation [110]. The refractive index transient also acts like a dynamic lens because the degree of alignment (anti-alignment) is proportional to the pump beam profile, which is usually higher near the beam center and lower near the edge. This molecular lensing effect [112] should be taken into account for correctly modelling the nonlinear propagation effect, in addition to electronic $\chi^{(3)}$-induced self-focusing.

In fact, as it will be seen later, for common diatomic gases such as nitrogen and oxygen, molecular alignment contribute much more than instantaneous nonlinearity to the refractive index modulation, contradicting results previously reported elsewhere. The alignment effect to nonlinear propagation will be explored in Chapter 5.

Many methods have been developed for producing and measuring laser alignment of molecules. Thus far, all methods use variations of the multi-shot pump and probe technique. For very low density molecular samples, an intense laser pulse (pump pulse) is used to align the molecule, and an intense ultrashort secondary pulse stepped through a variable delay (probe pulse) is used to remove electrons by field ionization and initiate coulomb explosion. The ionic fragment velocities are along the molecular axis direction at the time of electron removal, angularly resolved with respect to the pump polarization. This "Coulomb explosion imaging" technique measures the time resolved molecular alignment [114, 115].

All optical multi-shot pump-probe methods have also been used. The earliest optical measurements of alignment were applied to picosecond optical Kerr gating in liquids [42, 116]. A linearly polarized pump pulse torqued CS_2 molecules into alignment, creating a transient birefringence sampled by the polarization rotation imposed on a probe pulse variably delayed in the temporal vicinity of the pump. Later, it was realized that probe pulse delays long after the pump could sample quantum echoes of the molecular alignment (also called rotational recurrences) if this measurement were performed in much less collisional CS_2 vapour [117]. A version of this technique, now called Optical Kerr Effect (OKE) spectroscopy [118], depends on the birefringence, or small anisotropic refractive index change in a gas or liquid induced by the presence of pump-aligned molecules, and has been used to measure a wide range of molecular alignment dynamics, including the prompt response near the pump pulse and quantum echoes.

Other optical methods have recently been developed which depend on probe beam refraction from aligned molecular gas samples [119] and ionization of these samples [120]. Spectral modulations imposed on sequentially delayed short probe pulses have also been used to map out wavepacket recurrences, although the time resolution of these measurements is limited by the relatively long (> 50 fs) probe pulse duration, and quantitative molecular response is obtained only through propagation model-dependent fits to the shifted spectra [90, 121].

The only technique described above which is capable of direct quantitative measurement of alignment is Coulomb explosion imaging [114, 115], but this method is not capable of spatial resolution, and it is a time-consuming multi-shot pump-probe method. None of the above techniques combine the direct measurement of alignment, spatially resolved across the laser beam, with alignment evolution measured in a single shot.

In Chapter 2, a single-shot method for measuring ultrafast refractive index transient with 1-D space resolution was presented, with temporal resolution only limited by bandwidth of the supercontinuum probe beam. Here, this technique is used to measure the ultrafast laser-induced molecular alignment and the following periodic alignment recurrences that appear long after the laser pulse has passed. The single-shot measurement is an improvement over previous techniques for several reasons. First, in laser systems having even small shot to shot variations in energy (typical of most femtosecond laser systems) or pulse width, the alignment response will vary from shot to shot and the result of composite measurements could obscure low levels of response. Second, in experiments where conditions such as pump laser pulse energy or gas pressure are varied, collecting the full temporal response for each set of conditions is far less time consuming than doing shot by shot temporal scans.

4.2 Experimental setup and noise reduction technique

The experimental setup for measuring molecular alignment is the same as described in Chapter 2, which is partly shown again in Fig 4.1. A broadband (~ 100 nm FWHM) supercontinuum (SC) pulse is generated using self-focusing of a ~ 200–300 μJ, 100 fs, 800 nm Ti:Sapphire laser pulse in a xenon gas cell (not shown). The SC pulse is split into collinear twin pulses separated by time τ using a Michelson interferometer (reference pulse followed by probe pulse), which were then passed through a 2.5-cm-thick window of SF4 glass, dispersively stretching and linearly chirping them up to ~ 2 ps. For measuring pump-probe delays longer than the 2 ps probe pulse window, a delay line was implemented for placing the 2 ps probe window at delays up to 5 ns with respect to the pump. This allows measuring recurrences that occurred well after the pump pulse. The probe and reference SC beams were combined at a beamsplitter with the pump, and the three pulses were collinearly focused into a 45-cm-long gas cell. The combined pump/SC beam exiting the cell was passed through a zero degree dielectric Ti:Sapphire mirror to reject the pump beam.

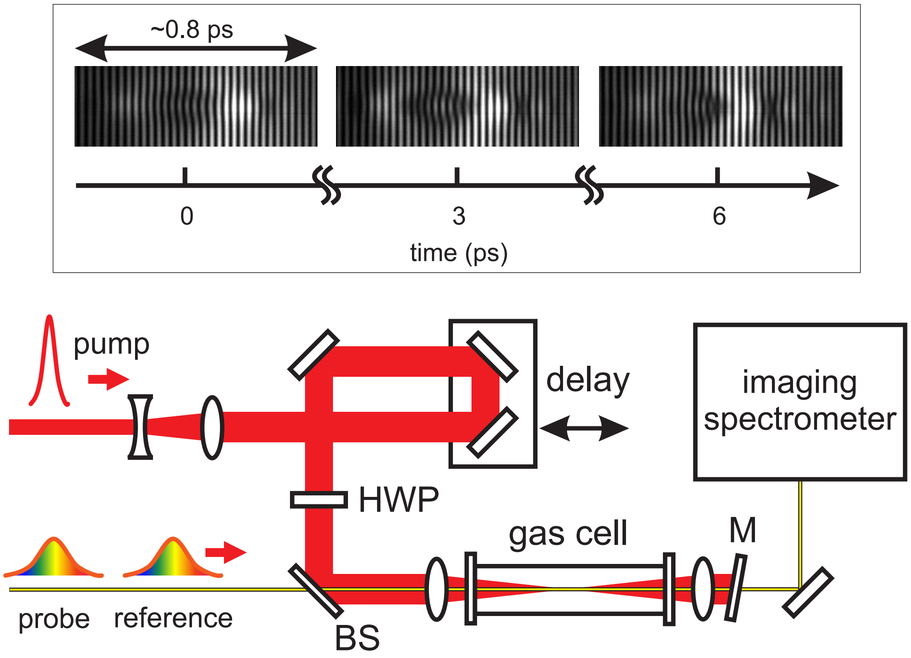

Figure 4.1: Experimental setup. HWP: half waveplate, BS: beamsplitter for combining pump and SC pulses, M: zero degree Ti:Sapphire dielectric mirror. The inset shows interferograms in 3 temporal windows, corresponding to laser field alignment (0 ps), quarter revival ($\sim$ 3 ps), and half revival ($\sim$ 6 ps) of the rotational wavepacket in 5.1 atm O_2.

The SC beam was imaged from the exit plane of the nonlinear interaction zone in the cell onto the entrance slit of an $f/2$ imaging spectrometer with a 1200 groove·mm^{-1} grating and a 10-bit CCD camera at the focal plane, recording interference patterns in the spectral domain (spectral interferograms). These 2D patterns had a $\sim$ 100 nm wide wavelength axis and perpendicular to that, a 0.67 μm/pixel spatial resolution along the entrance slit direction.

In addition, in anticipation of potentially tiny spectral amplitude modulations and phase shifts compared to the experiments in Chapter 2, in this Chapter a new method for interferogram analysis is implemented . For a CCD camera, thermal excitation of electrons, or dark current, from the CCD chip pixels, and readout noise from the amplifier and A/D circuit are two dominant noise sources [122]. To

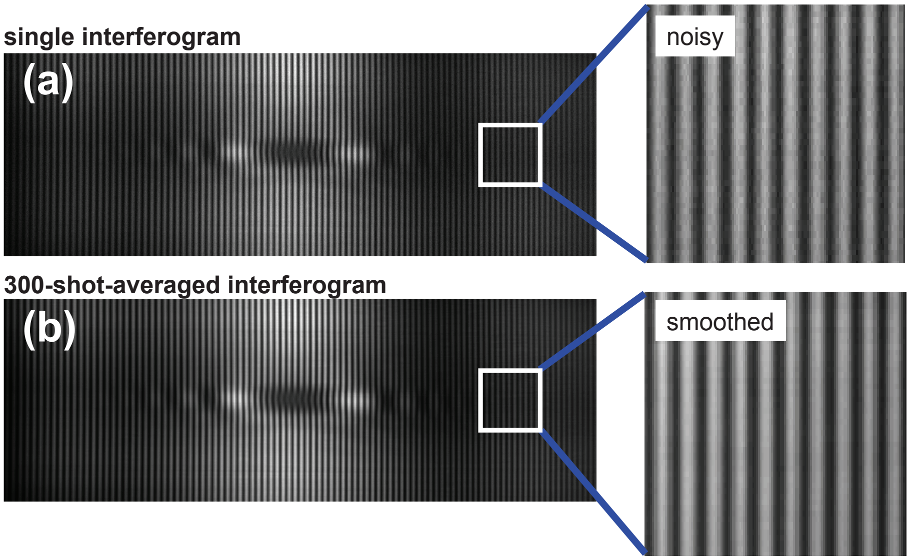

Figure 4.2: Sample interferogram images (a) from a single laser shot, and (b) after averaging over 300 shots.

suppress the interferogram noise and reveal the signals possibly smaller than the noise level of an individual shot, multi-shot averaging is desirable. Figure 4.2 has demonstrated the SC shot-to-shot stability by comparing a single interferogram with the averaged interferogram from 300 laser shots, and they appeared to be almost identical. However when examined closely, it can be seen that the interferogram image taken from a single laser shot (Fig. 4.2(a)) contains noisy speckles, while in its multi-shot-averaged counterpart (Fig. 4.2(b)) such noise is averaged out and results in a cleaner, smoother image with fringe pattern nearly unaffected. Therefore, instead of averaging spectral phases and amplitudse of probe and reference pulses retrieved from multiple interferograms, is was found feasible to directly average 300 consecutive interferograms *before* phase extraction, which dramatically increased speed of data processing. An estimate of the error in the extracted phase is $\delta\Phi_{\rm shot}/N_{\rm int}^{1/2}$, where $\delta\Phi_{\rm shot}$ is the maximum noise amplitude in the extracted phase of an individual shot and N_{int} is the number of averaged interferograms. Note that this procedure depends on the excellent shot-to-shot stability of the interferogram fringe locations and fringe visibility made possible by the very stable kHz pump laser and SC generation technique. For experiments with more shot-to-shot variability (such as typical with 10 Hz pump lasers), a much lower noise CCD camera would be required to achieve in a single shot the low levels of phase shift extracted in the current experiment. Also note that this methodology is still legitimately called "single-shot" even when this averaging technique is involved, owing to the fact that a single interferogram represents a snapshot of phase shift evolution during ~ 2 ps interval. By contrast the conventional multi-shot methods acquire information only at a specific time for each measurement.

4.3 Rotational inertia effect: delayed initial alignment by the laser field

The transient refractive index due to intense laser pulse interaction with linear gas molecules given in Chapter 3

$$n^2(t) = 1 + 4\pi N \left(\Delta\alpha\langle\cos^2\theta\rangle_t + \alpha_\perp\right) \tag{4.1}$$

only accounts for index variation owing to ensemble-averaged molecular alignment and neglects the "prompt" contribution of the nonlinear distortion of the molecular electron cloud by the laser field. Including both effect, it can be shown that, to second order in the field, the effective index is given by

$$\begin{aligned}\frac{n^2(t)-1}{4\pi N} &= \Delta\alpha\left\langle\cos^2\theta\right\rangle_t+\alpha_\perp \\ &\quad+|\mathbf{E}(t)|^2\left[\left\langle\sin^4\theta\right\rangle_t\alpha^{(3)}_{xxxx}+\frac{1}{4}\left\langle\sin^2 2\theta\right\rangle_t\left(\alpha^{(3)}_{xxzz}+\alpha^{(3)}_{zzxx}\right)+\left\langle\cos^4\theta\right\rangle_t\alpha^{(3)}_{zzzz}\right],\end{aligned} \tag{4.2}$$

where $\alpha^{(3)}_{ijkl}$ is the fourth rank molecular polarizability tensor and the "prompt" contribution is proportional to the square of the field envelope amplitude $|\mathbf{E}(t)|^2$. As seen in, for instance, Eq. 3.55, the angular ensemble averages $\langle\ \ \rangle_t$ consist of a constant term (from $t=-\infty$) and a term which is second order in peak field amplitude E_0. The prompt response therefore has an isotropic part proportional to $|\mathbf{E}(t)|^2$, and an orientational part proportional to $E_0^2|\mathbf{E}(t)|^2$ which is significantly smaller. The contribution to the refractive index of the prompt isotropic part is written as

$$\begin{aligned}n_2 I(t) = 2\pi N\,|\mathbf{E}(t)|^2\Big[&\left\langle\sin^4\theta\right\rangle_{t=-\infty}\alpha^{(3)}_{xxxx} \\ &+\frac{1}{4}\left\langle\sin^2 2\theta\right\rangle_{t=-\infty}\left(\alpha^{(3)}_{xxzz}+\alpha^{(3)}_{zzxx}\right)+\left\langle\cos^4\theta\right\rangle_{t=-\infty}\alpha^{(3)}_{zzzz}\Big],\end{aligned} \tag{4.3}$$

where n_2 is the isotropic nonlinear index of refraction, $I(t)$ is the laser intensity, and where $\left\langle\sin^4\theta\right\rangle_{t=-\infty}=8/15$, $\left\langle\sin^2 2\theta\right\rangle_{t=-\infty}=8/15$, and $\langle\cos^4\theta\rangle_{t=-\infty}=1/5$.

The effect of molecular rotational inertia is immediately seen from a comparison of the response of various gases during a time window which includes the pump pulse. The calculated (solid line) and measured (open circles) transient refractive index shifts in N_2 and N_2O near the 110 fs pump pulse are shown in Fig. 4.3(a) and Fig. 4.3(b). To compare the effect of rotational inertia, the peak magnitudes of Δn for both gases are normalized to 1. The calculation employs Eq. 3.55 and Eq. 3.56, which is the result of first-order perturbation theory with laser pulse shape approximated by the square of a cosine function. This approximation allows a well-defined envelope with its magnitude vanished at both beginning and end of the pulse. Due to the difficulty of determining the relative timing between the laser pulse and the transient refractive index measured from the experiment, the peaks of the normalized $\Delta n(t)$ from the experiment are aligned to that in the corresponding calculated curves on time axis for comparison in Fig. 4.3(a) and 4.3(b), and both measurements in two gases match the calculations remarkably well. The pulsed laser field gives an initial "kick" to the molecules, and due to rotational inertia they do not line up along the laser field instantaneously. Thus in Fig. 4.3(a) and 4.3(b), Δn peaks later than the driving laser pulse, with the peak for N_2 leading that of N_2O. This is understood from the larger N_2O moment of inertia I, where $B = h/(8\pi^2 cI)$. Moreover, as the coherently excited rotational wavepacket of N_2O evolves more slowly than that of N_2, its Δn falls back to zero more slowly than the Δn for N_2.

It is important to note that in the calculation of Fig. 4.3, the instantaneous electronic nonlinear response ($\chi^{(3)}$) is not included, but the measurements still agree well with the calculations. This implies that the alignment effect of the molecules dominates the prompt electronic response $n_2 I$: there is no pre-spike nor abrupt change of slope at the rising edge of measured $\Delta n(t)$, which are signatures of significant instantaneous component, in both gas species. The measured Δn curves

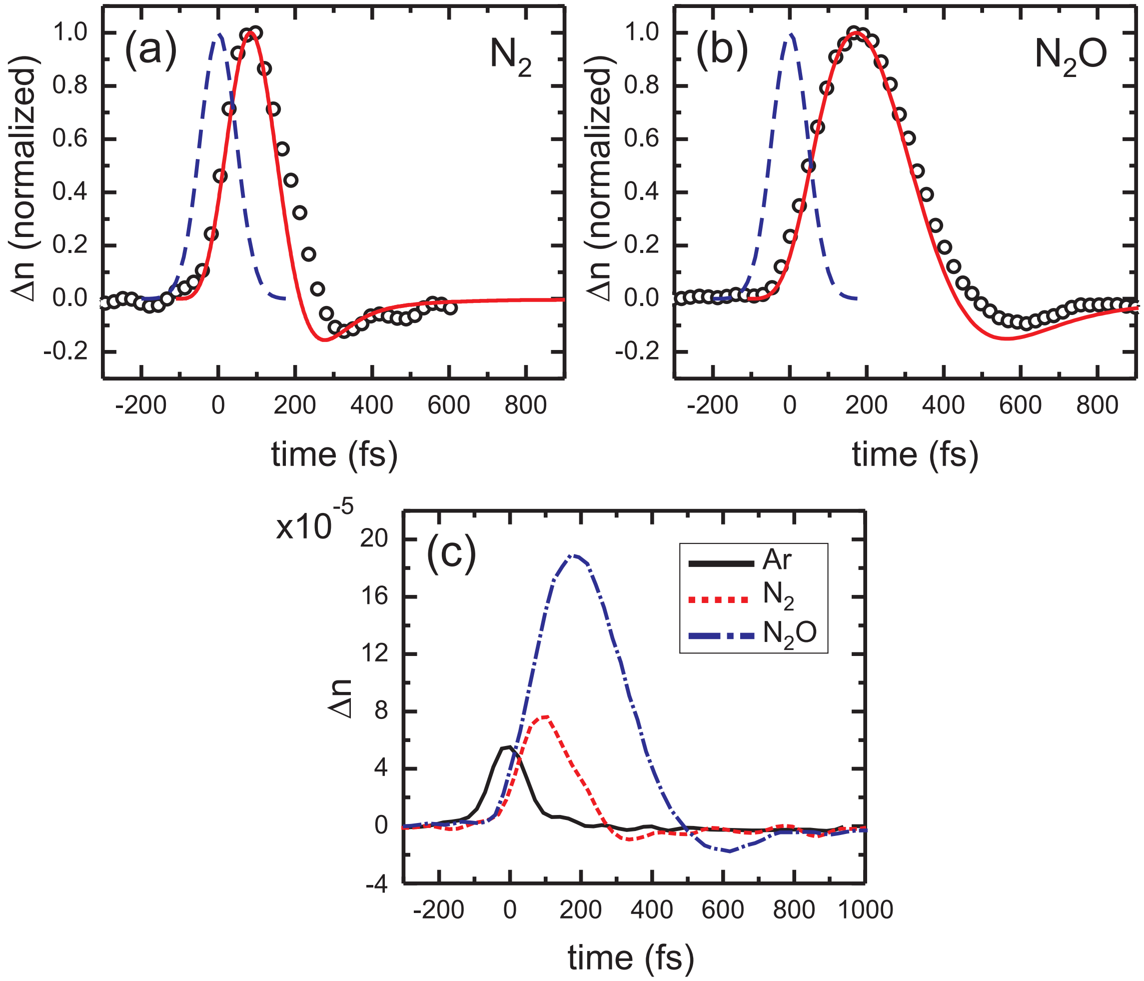

Figure 4.3: Normalized transient shift of refractive index Δn from measurements (open circles) and calculations (solid line) for (a) N_2 and (b) N_2O. For comparison, a Gaussian function centered at $t = 0$ with 110 fs FWHM duration is shown on each figure (dashed line) to represent the pump pulse envelope. Un-normalized Δn traces of (a) and (b), along with instantaneous electronic nonlinear response in Ar, are shown in (c), under the experiment conditions of 110 fs pump pulse duration with 95 μJ (6.7×10^{13} W/cm^2), 60 μJ (4.2×10^{13} W/cm^2), and 20 μJ (1.4×10^{13} W/cm^2) pulse energy (peak intensity), in 4.4 atm Ar, N_2, and N_2O, respectively.

are slightly wider than the calculations, which implies that there may be a small index change contributed by instantaneous $n_2 I$. This differs from Ref. [123], where the prompt response and the rotational inertia effects for N_2 are considered to contribute approximately equally to the transient refractive index. The justification in Ref. [123] relies on measurements of spectral modulation of an intense, 120-fs laser pulse passing through the gas sample, and the analysis requires free fitting of two parameters $n_{2,\text{instant}}$ and $n_{2,\text{rotation}} \propto \Delta\alpha$ to a detailed propagation model. This issue is important for studies of long range propagation and filamentation of femtosecond laser pulses in the atmosphere [90, 123, 124, 125], where the molecular alignment effect has been long underestimated. This will be further investigated in Chapter 5.

Figure 4.3(c) compares un-normalized Δn results using 4.4 atm Ar, N_2, and N_2O, with 95 μJ pump energy (6.7×10^{13} W/cm^2 peak intensity) for Ar, 60 μJ (4.2×10^{13} W/cm^2 peak intensity) for N_2, and 20 μJ (1.4×10^{13} W/cm^2 peak intensity) for N_2O. These intensities were chosen to produce as large a phase shift as possible without continuum generation and ionization, which would interfere with the SC probe and reference spectra. The Ar response is the purely prompt nonlinear electronic response. N_2 and N_2O measurements were conducted at lower intensities than Ar, however they still introduce larger index shifts, again implying that the orientational effect dominates in N_2 and N_2O. Note that as seen later in this chapter, for H_2 and D_2 the prompt electronic response is larger than the alignment response under the experiment conditions.

4.4 Quantum echoes of refractive index due to rephasing of the rotational wave packet

As mentioned earlier, at times past the pump pulse, molecular gases can exhibit echoes in their refractive index response due to the induced temporal coherence of multiple rotational quantum states. Figure 4.4(a) shows probe beam-center lineouts of the measured alignment $\langle \cos^2\theta \rangle_t - 1/3$ for 6.4 atm of N_2 for time windows centered at $t = 0$ through $t = 1.25\ T_{\mathrm{rev}}$ in $0.25\ T_{\mathrm{rev}}$ steps (where for $B_{N_2} = 2.0$ cm^{-1} [109], $T_{\mathrm{rev}} = (2cB_{N_2})^{-1} = 8.33$ ps). The pump pulse was 60 μJ, 110 fs, with peak intensity $I = 4.1 \times 10^{13}$ W/cm^2. Note that preceding the half revivals ($t = qT_{\mathrm{rev}}/2$, q is odd) and the full revivals (q is even) by an interval $\delta t \sim T_{\mathrm{rev}}/N_{\mathrm{rot}}$ are positive and negative excursions corresponding to alignment and anti-alignment, respectively. Figure 4.4(b) shows the corresponding space-time images across the probe beam, clearly showing the radial intensity dependence of alignment. Figure 4.4(c) shows a calculation of $\langle \cos^2\theta \rangle_t - 1/3$ for N_2 (using $\Delta\alpha_{N_2} = 9.3 \times 10^{-25}$ cm^3) comparing the finite pulse response (Eq. 3.55 and Eq. 3.56) with the impulse pump response (Eq. 3.53). The finite-bandwidth pulse is modeled by the square of cosine function with phase ranging from $-\pi/2$ to $\pi/2$, and the impulse is modelled by a delta function representing a laser pulse with extremely short duration and ultra-broad bandwidth, and for both cases the laser fluence is matched to the experimental value of 4.5×10^7 erg/cm^2. The decay constant $\gamma_{j,j-2}$ in Eqs. 3.53, 3.55 and 3.56 is assumed to be zero in the calculation for both finite pulse and impulse responses. It is seen that the finite pulse result match to the experimental curves

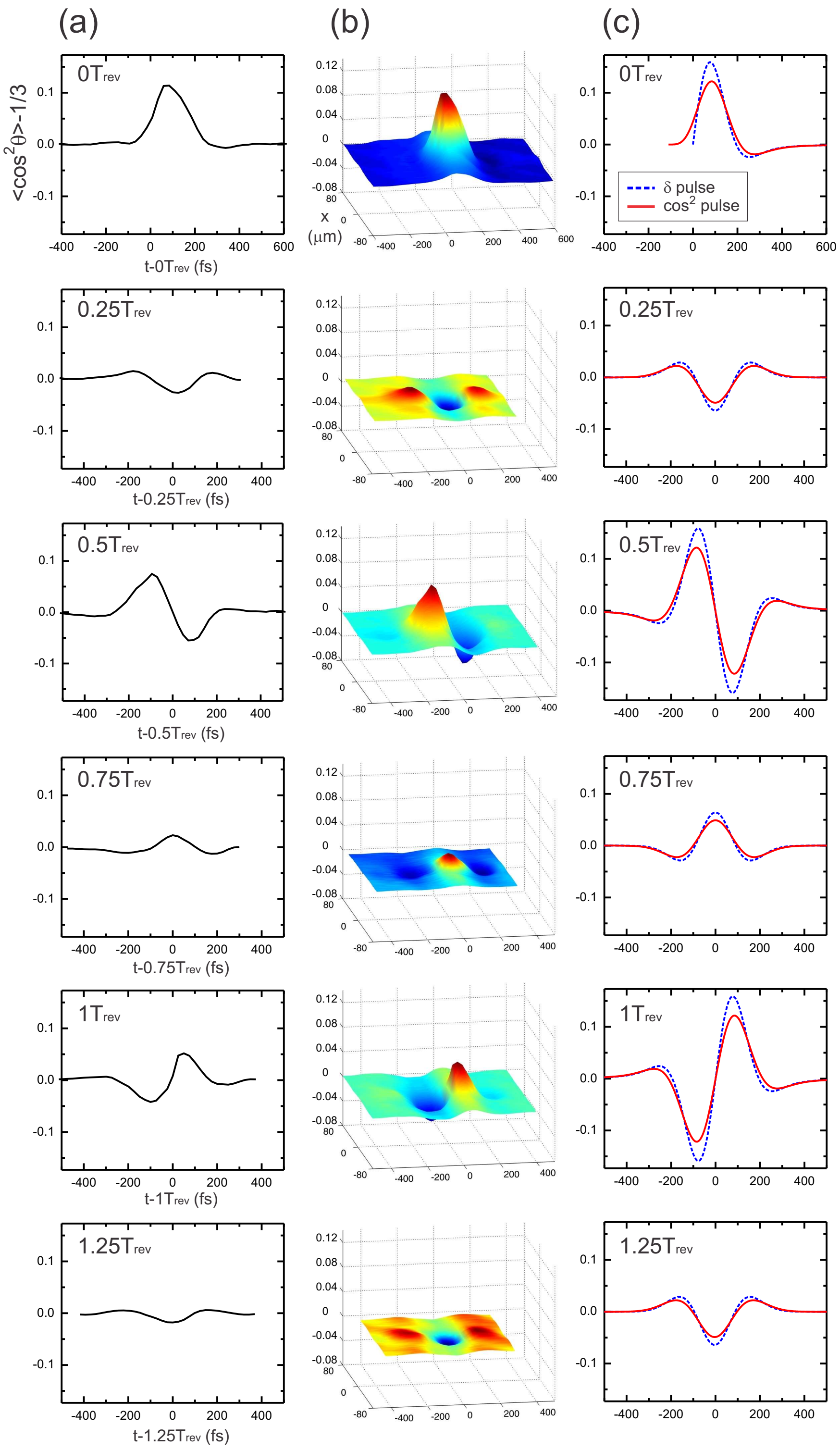

Figure 4.4: Measured N_2 alignment up to $t = 1.25\ T_{\text{rev}}$ for 6.4 atm gas pressure and 4.1×10^{13} W/cm^2 pump peak intensity: (a) probe beam central lineout, and (b) corresponding 2-D space- and time-resolved image across the probe beam. Calculated alignment is shown in (c), assuming two different excitation pulse shapes: delta function (dashed curve) and $\cos^2$ function with 110 fs FWHM (solid curve). For N_2, $T_{\text{rev}} = 8.3$ ps, and the collisional dephasing of wavepacket is not included in this calculation.

better, but the delta-function result is still quite reasonable. To explain this, note that for a thermal rotational distribution, it can be shown that the most populous state contributing to the wavepacket has $j = j_{\max} \sim \frac{3}{4}(1 + (1 + \frac{8}{9}\frac{k_B T}{Bhc})^{1/2})$. For $k_B T/Bhc \gg 1$, which is the case for N_2, $j_{\max} \sim (k_B T/Bhc)^{1/2} \sim 10$. For large $j_{\max}$, the frequency width of the thermal distribution of rotational states available for pumping is $\Delta\omega_{\text{rot}} \sim k_B T/\hbar \sim 4 \times 10^{13}$ s^{-1}. By comparison, the pump laser intensity envelope bandwidth $\widetilde{I}(\omega) = \int_{-\infty}^{\infty} I(t) \exp(-i\omega t) dt$ (corresponding to $\Delta\lambda_{\text{laser}} \sim 10$ nm) is $\Delta\omega_{\text{laser}} \sim 3 \times 10^{13}$ s^{-1}. As $\Delta\omega_{\text{laser}} \sim \Delta\omega_{\text{rot}}$, the bandwidth of the laser intensity envelope adequately overlaps the thermal distribution and therefore one would expect reasonable agreement in Fig. 4.4(c) with the delta function pump.

Note that the shapes of the calculated finite pulse alignment response curves for N_2 are an excellent match to the experimental results, except with discrepancies in amplitude. The calculation shows equal peak amplitudes for quarter-revivals and for half-, full-revivals and the initial response, while the measured amplitudes decay in time. This is because the dephasing (decoherence) terms $\gamma_{j,j-2}$ have been omitted in the calculation.

Figure 4.5 repeats for O_2 in the format of Fig. 4.4 for a cell pressure of 5.1 atm and pump pulse energy 40 μJ (peak intensity $I = 2.7 \times 10^{13}$ W/cm^2). Figure 4.5(a) shows probe beam-center lineouts of the measured O_2 alignment $\langle \cos^2\theta \rangle_t - 1/3$ for time windows centered at $t = 0$ through $t = 1.25\ T_{\text{rev}}$ in 0.25 T_{rev} steps, where $T_{\text{rev}} = (2cB_{O_2})^{-1} = 11.6$ ps [109]. Note that unlike in N_2, the $t = 1/4\ T_{\text{rev}}$ and $t = 3/4\ T_{\text{rev}}$ revivals in O_2 are comparable in amplitude to the full- and half-revivals, which originates from the zero nuclear spin of $^{16}_{8}O$. As discussed in

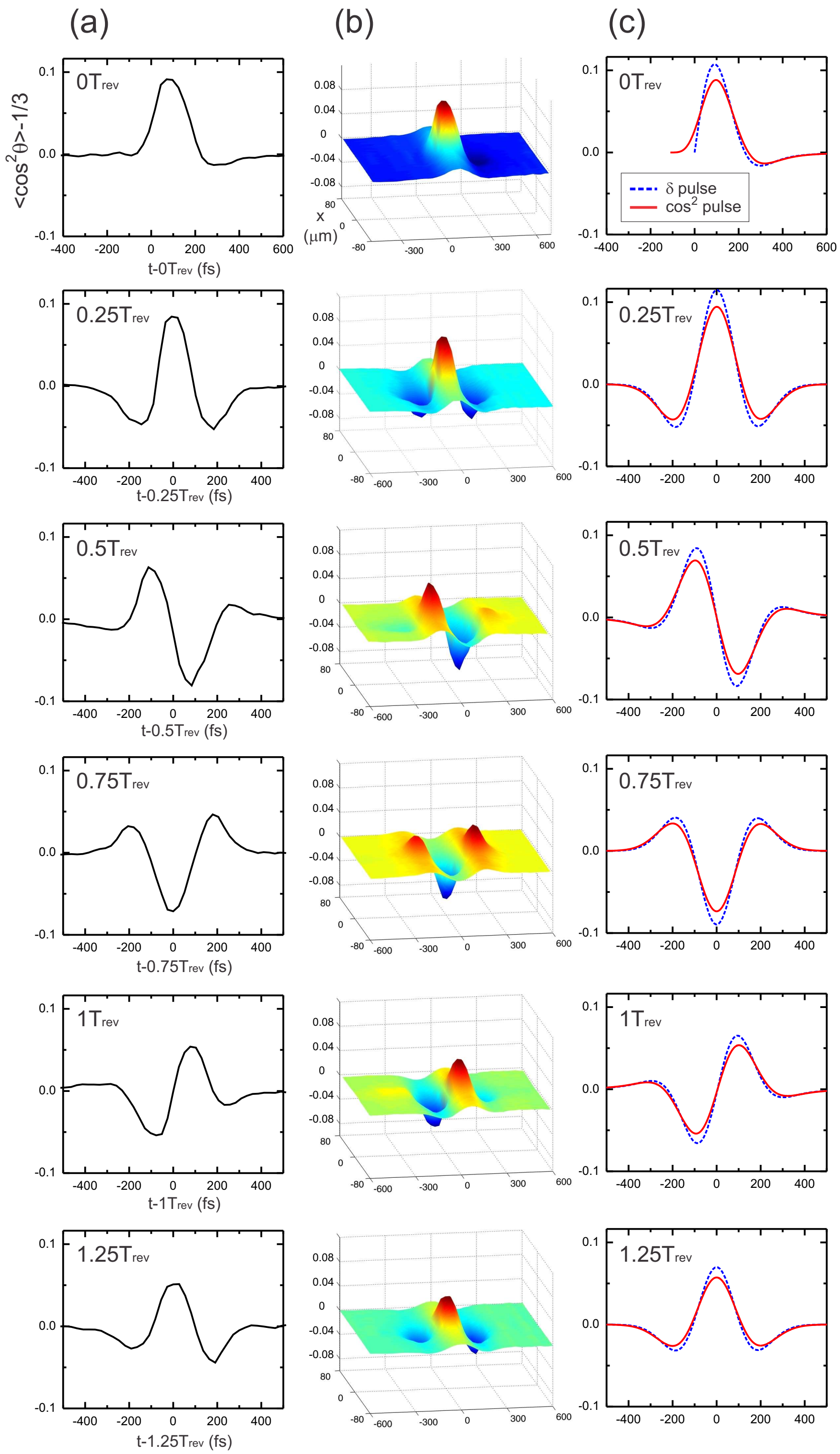

Figure 4.5: Measured O_2 alignment up to $t = 1.25\ T_{\text{rev}}$, where $T_{\text{rev}} = 11.6$ ps for O_2, for 5.1 atm gas pressure and 2.7×10^{13} W/cm^2 pump peak intensity: (a) probe beam central lineout, and (b) corresponding 2-D space- and time-resolved image across the probe beam. The dephasing time constant $1/\gamma = 23.2$ ps was obtained by fitting the peak amplitudes of (a) to an exponential. Calculated alignment is shown in (c), including dephasing by using the extracted value of γ, and assuming two different excitation pulse shapes: delta function (dashed curve) and $\cos^2$ function with 110 fs FWHM (solid curve).

Chapter 3, only odd j states are populated, so that at the quarter revivals there is no cancellation of aligned and anti-aligned states as observed in N_2. Figure 4.5(b) shows the same revivals plotted versus space and time, and Fig. 4.5(c) shows calculations of alignment (using $B_{O_2} = 1.44$ cm^{-1} and $\Delta\alpha_{O_2} = 1.14 \times 10^{-24}$ cm^3 [109]) using the delta function pulse and the finite duration (110 fs) pulse, where a damping rate of $\gamma_{j,j-2} = \gamma = 4.31 \times 10^{10}$ s^{-1} (or dephasing time $1/\gamma = 23.2$ ps) was used. The damping rate was obtained from a fit to the declining peak amplitudes in the time sequence data of Fig. 4.5(a). Since dephasing is dominated by elastic molecular collisions, there should be little j dependence of the dephasing rate; hence it is reasonable to put $\gamma_{j,j-2} = \gamma$. For O_2, as for N_2 in Fig. 4.4, the best agreement with the data is obtained with the finite pulse, with the delta function response fitting the finite pulse response reasonably well. For oxygen at room temperature, $j_{\max} \sim 13$ and therefore, to a similar extent as in N_2, the rotational state wavepacket contribution is thermally limited rather than pump laser spectrum limited.

Results for N_2O, a linear molecule with a much greater moment of inertia (and lower rotational constant) are shown in Fig. 4.6, for pump energy of 20 μJ (peak intensity $I = 1.4 \times 10^{13}$ W/cm^2) and cell pressure 2.4 atm. Beam center lineouts of the alignment are shown in Fig. 4.6(a) for windows centered at $t = 0$, $t = 0.5\ T_{\mathrm{rev}}$ and $t = T_{\mathrm{rev}}$, where $T_{\mathrm{rev}} = (2cB_{N_2O})^{-1} = 40.5$ ps [109]. The 1/4 and 3/4 revivals are not present owing to the axial asymmetry of the linear N_2O molecule, in which the atoms are ordered N-N-O. Thus even and odd j rotational states are populated with equal weight, causing the aligned and anti-aligned contributions to cancel. Figure 4.6 shows the same revivals in full space-time plots, and Fig. 4.6(c) again

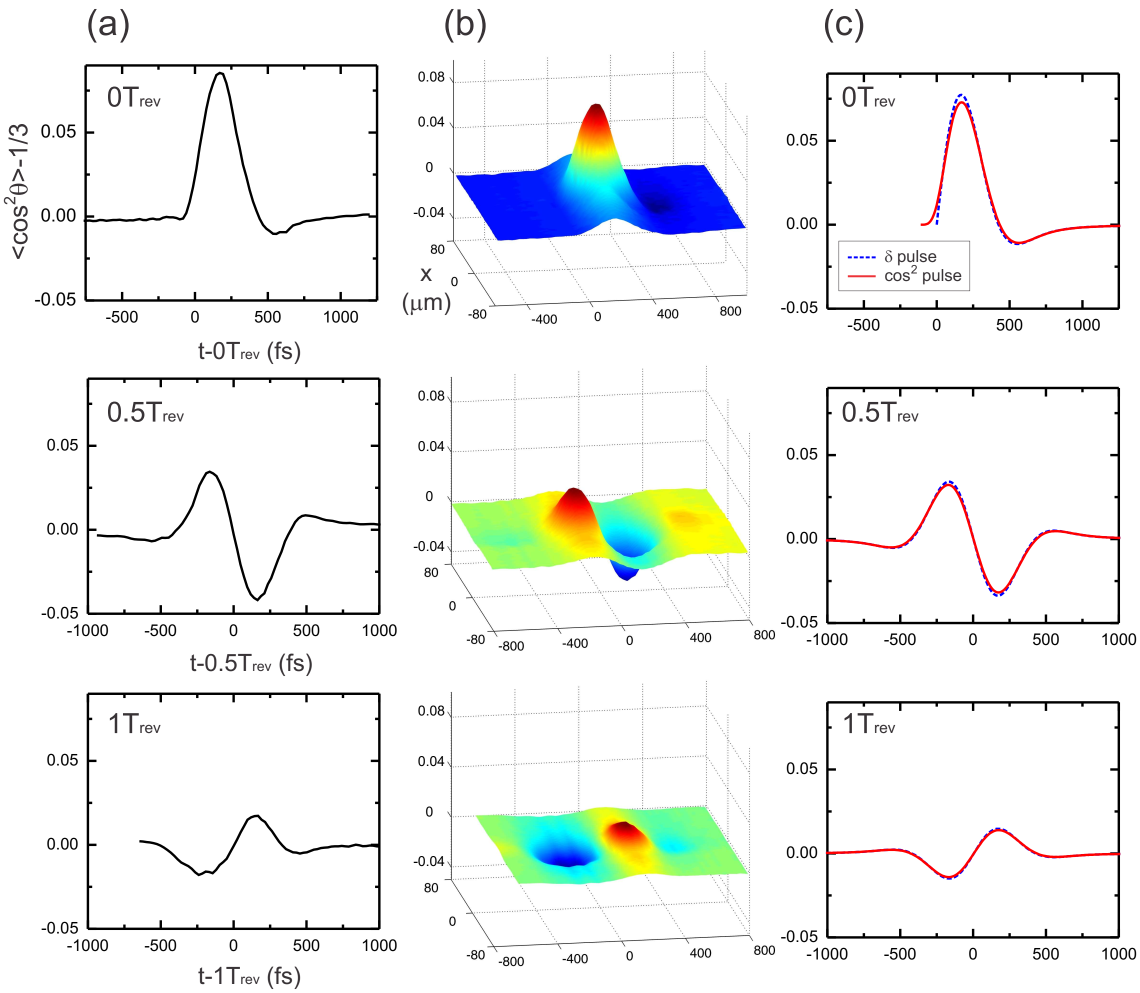

Figure 4.6: Measured N_2O alignment up to $t = T_{\text{rev}}$, where $T_{\text{rev}} = 40.5$ ps for N_2O, for 2.4 atm gas pressure and 1.4×10^{13} W/cm^2 pump peak intensity: (a) probe beam central lineout, and (b) corresponding 2-D space- and time-resolved image across the probe beam. Note that the 1/4 and 3/4 revivals are not present due to the axial asymmetry of the N_2O molecule. The dephasing time constant $1/\gamma = 23.8$ ps was obtained by fitting the peak amplitudes of (a) to an exponential. Calculated alignment is shown in (c), using the extracted dephasing rate γ and assuming two different excitation pulse shapes: delta function (dashed curve) and cos^2 function with 110 fs FWHM (solid curve).

shows calculations for finite and delta function pulses using $B_{\mathrm{N_2O}} = 0.412$ cm^{-1} and $\Delta\alpha_{\mathrm{N_2O}} = 2.79 \times 10^{-24}$ cm^3 [109]. Here the delta function result shows even better agreement with the finite pulse result and the experimental revival curves. Here $j_{\mathrm{max}} \sim 22$, so the approximation $\Delta\omega_{\mathrm{rot}} \sim k_B T/\hbar$ applies even better, with $\Delta\omega_{\mathrm{laser}} > \Delta\omega_{\mathrm{rot}}$ as in the N_2 and O_2 cases.

Measurements are also performed for D_2 and H_2, which have the smallest moments of inertia and largest values of B and therefore rotate the fastest. In Fig. 4.7(a) is shown a beam center lineout of the alignment recurrences in 7.8 atm D_2 for a pump energy of 65 μJ (peak intensity $I = 4.4 \times 10^{13}$ W/cm^2), with the corresponding time-space plot shown in Fig. 4.7(b). The delta function and finite pulse calculations are shown in Fig. 4.7(d), where $\Delta\alpha_{D_2} = 0.292 \times 10^{-24}$ cm^3 [109] and $B_{D_2} = 30.4$ cm^{-1} are used, as determined below in connection with Fig. 4.7(c). This corresponds to $T_{\mathrm{rev}} = 548$ fs, so that the single-shot temporal window is ~ 2.5 T_{rev} long. Earlier results for D_2 using Coulomb explosion imaging [126] showed revivals through ~ 0.5 T_{rev}, with error bars comparable to the revival amplitudes. In the case presented here, apart from any effects due to probe bandwidth limitation or phase front distortion [78, 79], the estimated error is $(\delta\Phi_{\mathrm{shot}}/N_{\mathrm{int}}^{1/2})(\Delta\Phi)^{-1} \sim 2\%$.

For D_2, there are two significant differences with the calculations for the smaller B molecules discussed earlier. First, the delta-function and finite pulse results are strikingly different. The large value of B results in much lower j states dominating the wavepacket so that for D_2, $j_{\mathrm{max}} \sim \frac{3}{4}(1 + (1 + \frac{8}{9}\frac{k_B T}{Bhc})^{1/2}) \sim 2$–3. Deuterium has a spin-1 nucleus, so that for the D_2 molecule, even rotational j states are twice as populated as odd j. Dominant coupled $\Delta j = 2$ states near j_{max} are therefore $j = 2$

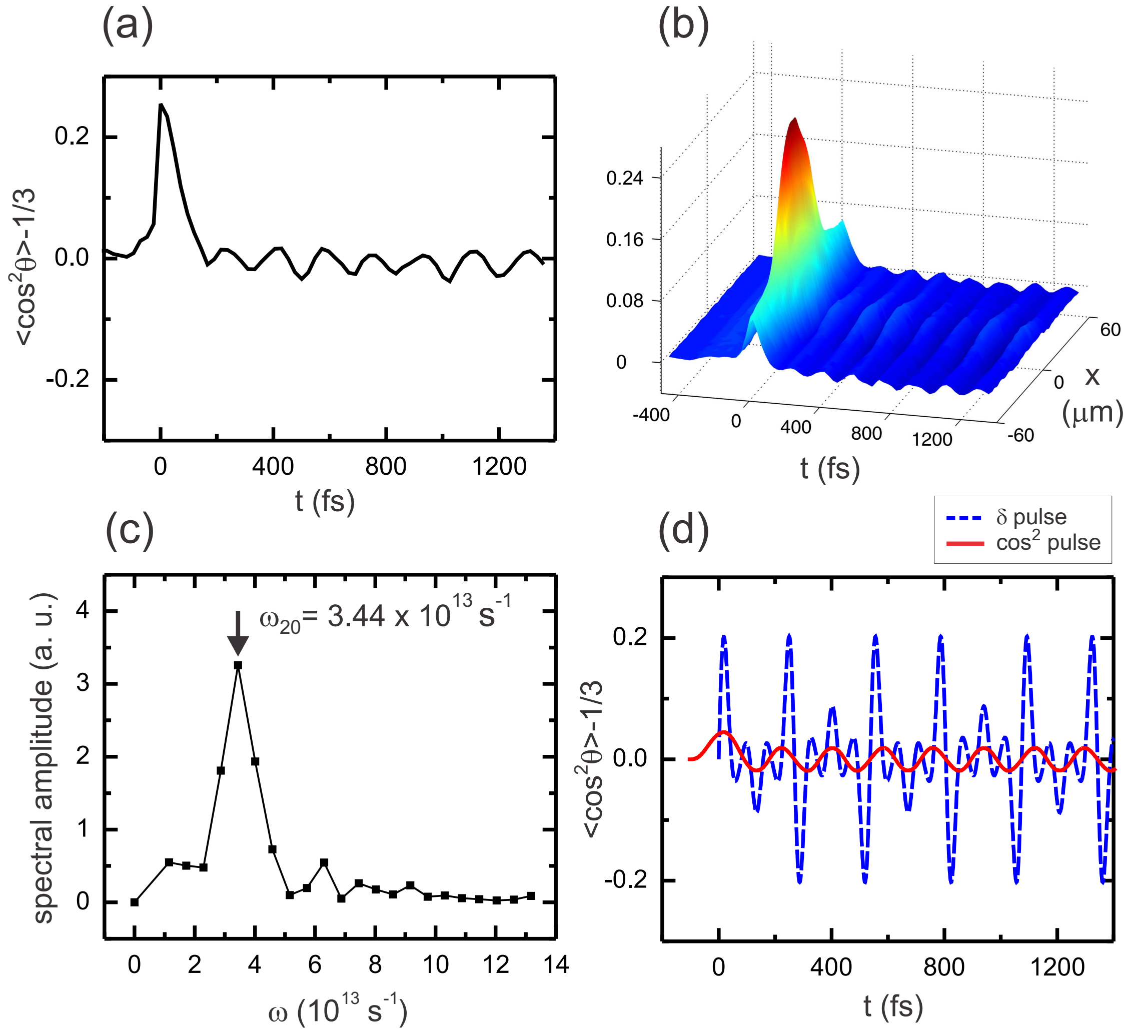

Figure 4.7: (a) Pump beam center lineout and (b) corresponding x-t perspective plot of measured D_2 molecule alignment recurrences excited by 65 μJ pump energy (4.4×10^{13} W/cm^2 peak intensity), with 7.8 atm gas pressure. (c) Fourier transform of the signal representing rotational wavepacket revivals after the pump pulse in (a). The peak frequency is identified as $\omega_{2,0} \sim 3.4 \times 10^{13}$ s^{-1}, giving the rotational constant $B_{D_2} = 30.4$ cm^{-1}. (d) Calculated alignment with delta function (dashed curve) and 110 fs cos^2 function (solid curve), using B_{D_2} obtained in (c).

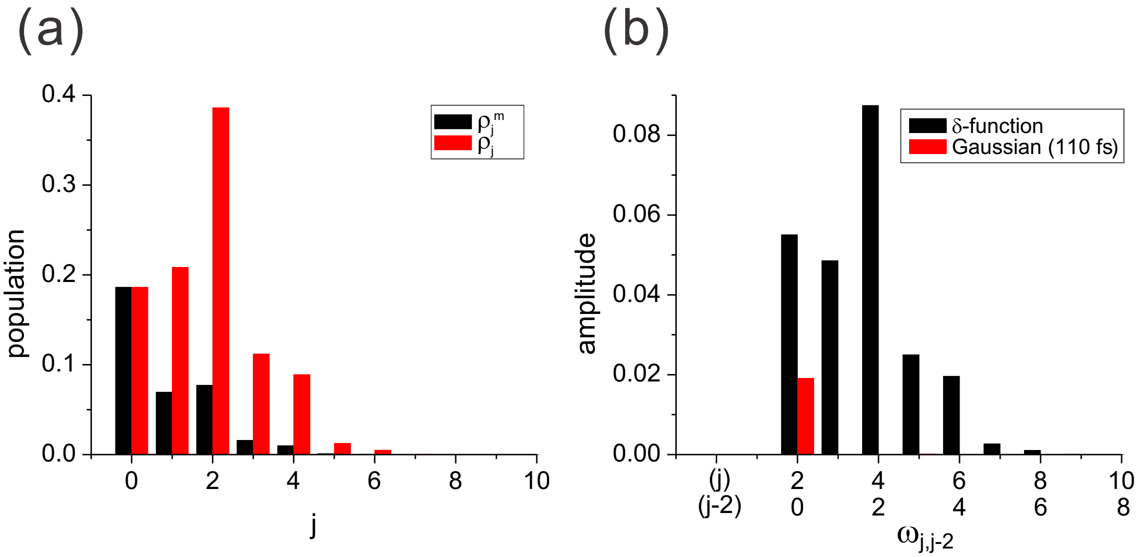

Figure 4.8: (a) Thermal rotational population ρ_j and ρ_j^m, and (b) calculated amplitude of frequency components $\omega_{j,j-2}$ contributing to molecular alignment of D_2 at $T = 300$ K. The pump pulse shapes are assumed to be delta function and Gaussian, with fluence (peak intensity) matching the experimental parameters used in Fig. 4.7.

and $j = 4$, which have a frequency spacing $\omega_{4,2} = \omega_4 - \omega_2 = 28\pi c B_{\mathrm{D}_2} = 8.0 \times 10^{13}$ s^{-1}, or $j = 0$ and $j = 2$, with $\omega_{2,0} = 12\pi c B_{\mathrm{D}_2} = 3.4 \times 10^{13}$ s^{-1}. Thus, the pump intensity envelope bandwidth of 3×10^{13} s^{-1} is barely adequate to overlap the latter two rotation states. Fourier transforming the revivals of Fig. 4.7(a) (ignoring the first spike representing the initial alignment plus the electronic response) shows explicitly, as seen in Fig. 4.7(c), the sparse modal content of the wavepacket: the peak at $\omega = 3.44 \times 10^{13}$ s^{-1} is immediately identified as $\omega_{2,0}$, and allows us to extract the value of $B_{\mathrm{D}_2} = 30.4$ cm^{-1} used in the calculations as discussed above. There is negligible contribution from other states. The estimation above is also confirmed by calculating the thermal population of D_2 rotational levels ρ_j^m (for each m state, as defined in Eq. 3.44) and $\rho_j = (2j + 1)\rho_j^m$ (summing over all degenerate m states) at $T = 300$ K, and spectral amplitude of alignment revivals (which is in proportional to $(\rho_j^m - \rho_{j-2}^m)(j^2 - j)/(2j-1))$ for each constituent frequency component $\omega_{j,j-2}$ by impulse excitation (using Eq. 3.53) and by a 110-fs finite-bandwidth pulse (using Eq. 3.54), which are shown in Fig. 4.8(a) and Fig. 4.8(b), respectively.

Results for H_2 are shown in Fig. 4.9, for the same pressure and pump laser conditions as in the D_2 measurement. A beam center lineout of alignment is shown in Fig. 4.9(a), and it is seen that the effect is much smaller than in D_2. If not for the full space-time plot in Fig. 4.9(b), where the revivals are seen to follow the pulse like a wake, one might not have recognized the small amplitude revivals in the lineout. For H_2, the error in the extracted phase shift is estimated to be $(\delta\Phi_{\text{shot}}/N_{\text{int}}^{1/2})(\Delta\Phi)^{-1} \sim 15\%$. The revivals are well-modelled by the finite pulse calculation, where the rotational constant that best fits the Fourier-transformed response is $B_{H_2} = 61.8\ \text{cm}^{-1}$, in good agreement with previous values [109], and using $\Delta\alpha_{H_2} = 0.30 \times 10^{-24}\ \text{cm}^3$ [109]. This corresponds to $T_{\text{rev}} = 270$ fs, so that the single-shot temporal window is $\sim 3\ T_{\text{rev}}$ long. As in the case for D_2, the delta function and finite pulse calculations differ substantially because of the insufficient pump bandwidth of the finite pulse to populate many rotational states.

For the H_2 rotational wavepacket, the most populated state is estimated to be $j_{\text{max}} \sim 2$. The spin of the H nucleus is 1/2, so that odd j states are 3 times more populated than even j states, therefore the likely coupled $\Delta j = 2$ states are actually $j = 3$ and $j = 1$ for a delta-function pulse. However for a 110-fs laser pulse envelope, the bandwidth is far from adequate to reach $\omega_{3,1}$, and it can only excite alignment between $j = 2$ and $j = 0$ with $\omega_{2,0} = 12\pi c B_{H_2} \sim 7 \times 10^{13}\ \text{s}^{-1}$, and the amplitude is much weaker than that excited by the same pulse in D_2. Figure 4.9(c) shows a

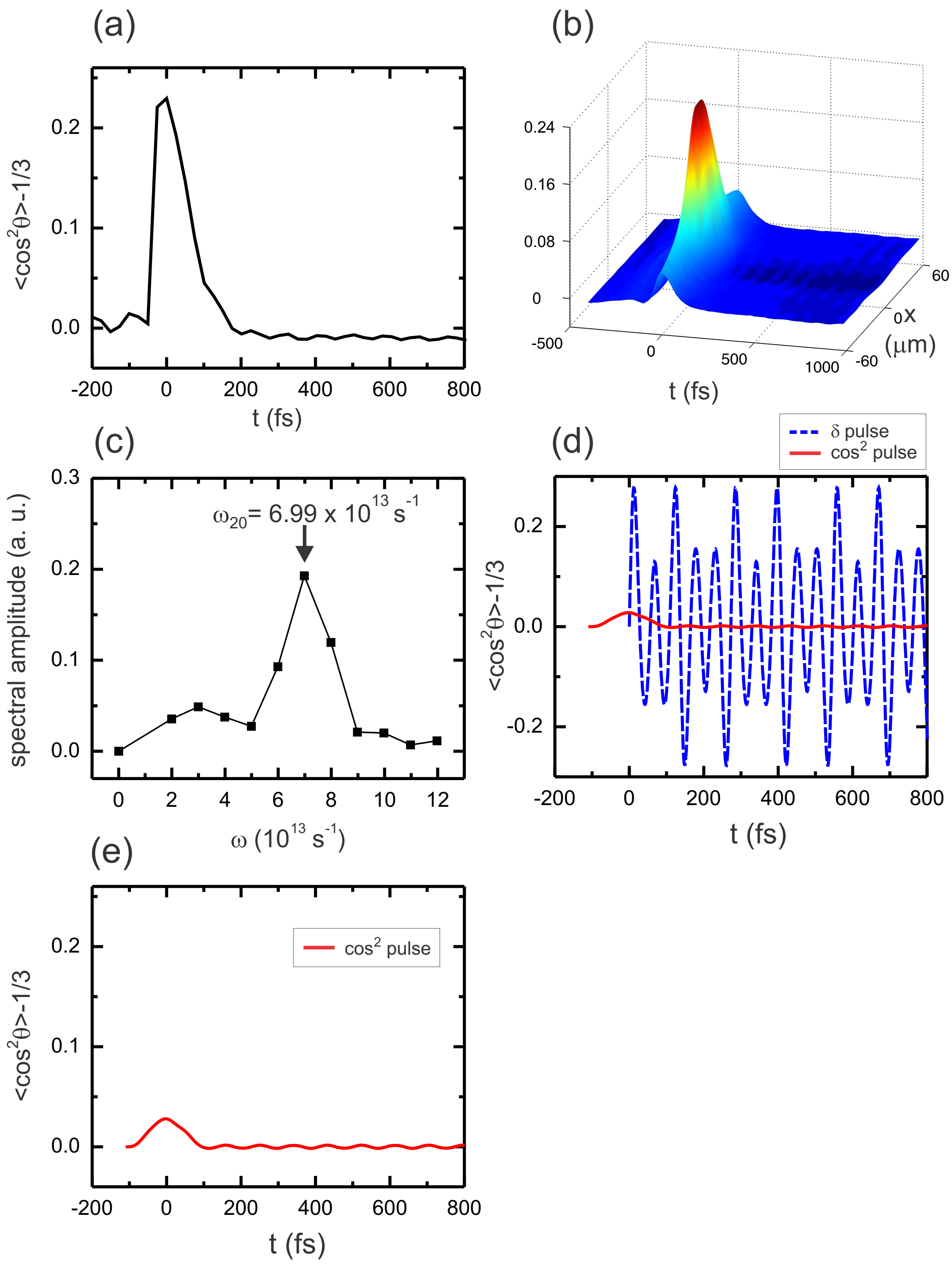

Figure 4.9: (a) Pump beam center lineout and (b) corresponding x-t perspective plot of H_2 alignment recurrences, measured in the same experiment conditions as in Fig. 4.7. (c) $\omega_{2,0} \sim 7 \times 10^{13}$ s^{-1} is observed by Fourier transformation of recurrence signal (neglecting the first peak) in (a), which gives the rotational constant $B_{H_2} = 61.8$ cm^{-1}. (d) Calculated alignment with delta function (dashed line) and 110-fs $\cos^2$ function (solid line), with rotational constant given from (c). The calculated $\cos^2$ pulse response is shown again in (e), with proper scaling revealing the small wiggles of revivals.

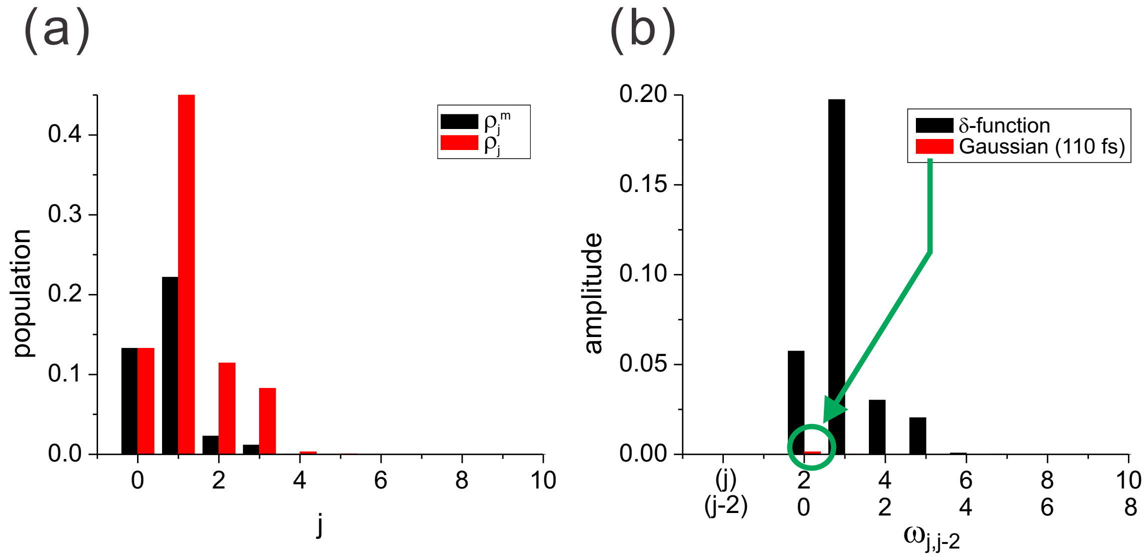

Figure 4.10: (a) Thermal rotational population ρ_j and ρ_j^m, and (b) calculated amplitude of frequency components $\omega_{j,j-2}$ contributing to molecular alignment of H_2 at $T = 300$ K. The pump pulse shapes are assumed to be delta function and Gaussian, with fluence (peak intensity) matching the experimental parameters used in Fig. 4.9.

Fourier transform of the revivals of Fig. 4.9(a), confirming that the H_2 revivals are generated by beating of the two low amplitude $j = 0$ and $j = 2$ rotational modes.

The calculated alignments excited by the delta-function pulse and by the 110 fs finite-bandwidth pulse are shown in Fig. 4.9(d) and Fig. 4.9(e). Employing the same methods applied to D_2, the thermal population of H_2 rotational levels at 300K and spectral amplitudes of calculated alignment revivals are shown in Fig. 4.10(a) and 4.10(b), respectively. From Fig. 4.10(a) it can be seen that the most populated state is $j = 1$, which is close to the simple estimation above, and for the impulse response the dominating spectral component is $\omega_{3,1}$, as shown in Fig. 4.10(b). On the other hand, it can be also confirmed from Fig. 4.10(b) that the major frequency component of H_2 alignment revivals induced by the 110-fs laser pulse is $\omega_{2,0}$, which is the same as in D_2 but has much weaker amplitude compared with Fig. 4.8(b).

In contrast to the finite pulse calculations (Fig. 4.7(d) and Fig. 4.9(d)(e)), the experimental results of D_2 and H_2 alignment (Fig. 4.7(a) and Fig. 4.9(a)) show an initial peak with much higher amplitude than the following revivals. We note that the calculation accounts only for the rotational effect on the refractive index. For D_2 and H_2, the relative contribution of the isotropic $n_2 I$ to the prompt response is much greater than for the smaller B molecules, where the delayed rotational response dominates near the pump, as seen by the excellent match of calculations and experiment shown for N_2, O_2, and N_2O.

Measurement of molecular alignment at different angles between the pump and probe polarization is also demonstrated. The pump polarization is tuned by rotating a half wave plate in the pump beam path (HWP in Fig. 4.1). The reflectivity of the dielectric-coated beamsplitter (BS in Fig. 4.1) is not sensitive to polarization over the pump pulse bandwidth. This is verified by measuring the reflected pump pulse energy while rotating the pump polarization. As an example, for 5.2 atm of O_2, Fig. 4.11 compares the response near $t = 0.75\ T_{\mathrm{rev}}$ for pump polarization parallel ($\langle \cos^2\theta \rangle_t - \frac{1}{3}$) and perpendicular ($\frac{1}{2}\left\langle \sin^2\theta \right\rangle_t - \frac{1}{3}$) to the probe. The pump energy and peak intensity are 40 μJ and 2.7×10^{13} W/cm^2, respectively. As expected, the measured response from perpendicular polarization case has half the magnitude of the parallel polarization case with the sign flipped.

Finally, results are presented for the gas pressure dependence of collisional dephasing of the wavepacket. The first half-revival in N_2O is shown in Fig. 4.12(a) normalized to the first alignment peak near $t = 0$ for several gas cell pressures: 2.4, 3.7, 5.1, and 6.4 atm. The dephasing rate γ for each pressure was obtained from a

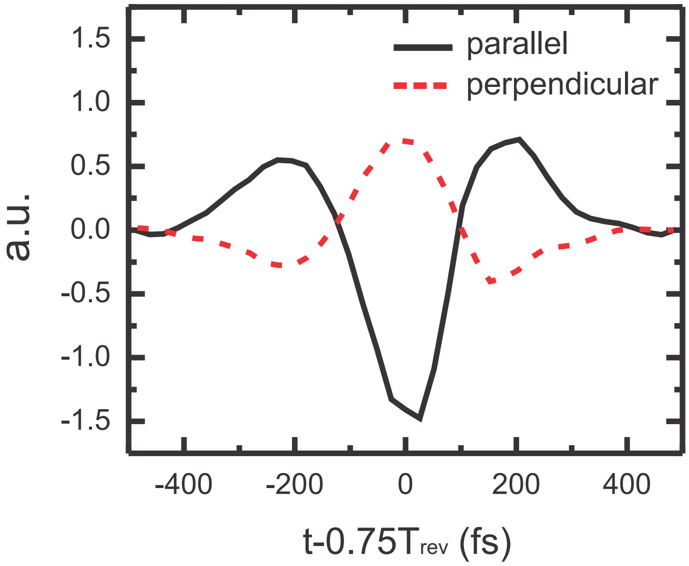

Figure 4.11: Transient refractive indices of 5.1 atm O_2 near 3/4-revival of the rotational wavepacket for the pump polarization parallel (solid curve) and perpendicular (dashed curve) to the probe beam. The pump pulse energy and peak intensity is 40 μJ and 2.7×10^{13} W/cm^2.

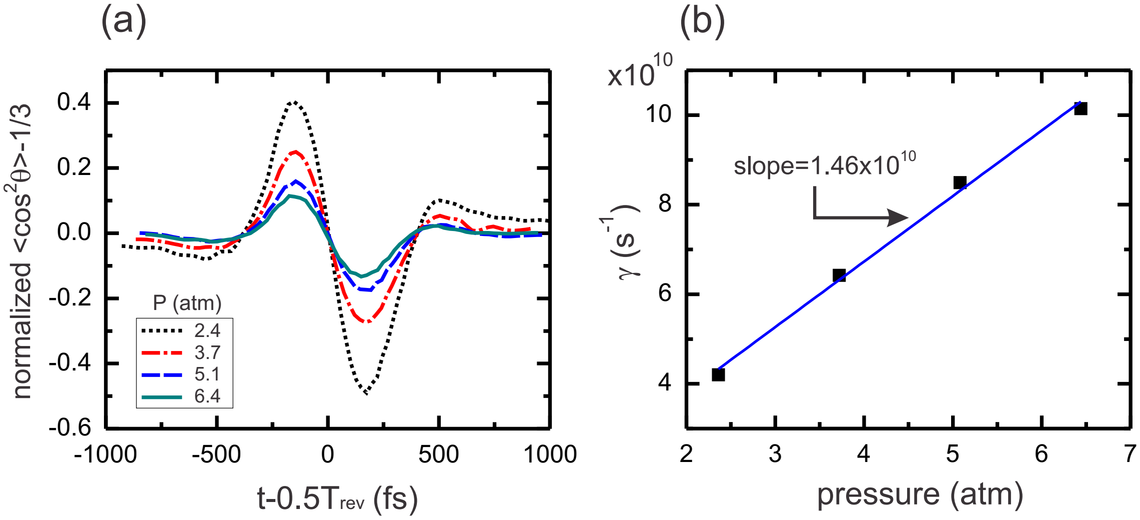

Figure 4.12: (a) Measured 1/2-revivals of N_2O alignment at pressures of 2.4, 3.7, 5.1, and 6.4 atm, normalized to the peak alignment amplitude near $t = 0$. (b) Dephasing rate γ versus N_2O pressure (squares) with a linear fit (solid line). The dephasing rate per unit pressure is 1.46×10^{10} s^{-1} atm^{-1}. The laser pulse energy is 20 μJ, corresponding to 1.4×10^{13} W/cm^2 peak intensity.

fit to the decay of revival amplitudes from $t = 0$ through $t = T_{\mathrm{rev}}$. The dephasing rate is plotted versus pressure in Fig. 4.12(b), and it is seen that the dependence is linear, as expected from the process of binary collisions. The dephasing rate per unit pressure obtained from a linear fit is 1.46×10^{10} s^{-1} atm^{-1}.

4.5 Conclusion

In conclusion, single-shot supercontinuum spectral interferometry (SSSI) is applied to measure, for the first time in a single-shot, the space- and time-resolved quantum rotational echo response of a number of molecular gases to femtosecond pulse excitation. In particular, these measurements have been achieved for H_2 and D_2, for which the low level of the effect could easily have been hidden in the shot-to-shot fluctuations characteristic of multi-shot pump-probe techniques.

Chapter 5

Direct measurement of the electron density of femtosecond laser pulse-induced filament in air

5.1 Introduction

It is shown by a simple model in Chapter 1 that diffraction of a laser pulse can be balanced by self-focusing, when the peak laser power reaches a critical power P_{cr}. This phenomenon was first observed in solids [21, 127, 128], in which fine damage tracks were formed for an extended length along the direction of laser propagation, indicating that the laser beam formed a transversely confined “hot spot”, with the local intensity exceeding the material damage threshold for an axial distance significantly longer than the Rayleigh range. In 1995, filamentation of intense femtosecond laser pulses in gas was reported [23]. In this case, in addition to diffraction, plasma generation and refraction is also involved and plays an important role to the beam propagation. When the laser power is above P_{cr}, the laser intensity will eventually exceed the ionization threshold of the gas due to self-focusing during the propagation. The resulting plasma provides a negative-lens-like refractive index profile, which tends to defocus the beam. This dynamic balancing between self-focusing and ionization defocusing leads to the development of one or multiple highly transversely confined (< 100 μm in diameter) optical “filaments” at a typical intensity of $\sim 10^{13}$ W/cm^2, with self-sustained propagation accompanied by electron density tracks over distances from centimeters to meters in the laboratory, or even hundreds of meters in the atmosphere.

Filamentation by femtosecond pulses in gases has been subsequently studied by many groups pursuing both basic understanding and applications [129, 130, 131]. Because the extended propagation of high intensities in a filament is not constrained by the need for a guiding structure, it is ideal for applications requiring long-range delivery of optical fields, such as remote sensing [132], spectral broadening [133] and shaping [134] of ultrashort laser pulses, and terahertz generation [135, 136]. Moreover, the filament is an ionized channel, which is promising for guiding of electrical discharges and even for lightning protection [137, 138].

While optical filamentation can be simply interpreted as the dynamic balance between nonlinear self-focusing of an intense optical pulse and laser plasma-induced defocusing, the detailed process is rather complicated and requires a full spatio-temporal model simulation to describe such nonlinear propagation. A simplified pictorial description of filamentation process is the "moving focus" model [139, 140], in which during the propagation the different time slices of the laser pulse have different effective focal length [19]:

$$z_{\mathrm{f}} = \frac{0.367 z_{\mathrm{R}}}{\sqrt{\left[\left(\frac{P}{P_{\mathrm{cr}}}\right)^{1/2} - 0.852\right]^2 - 0.0219}}, \tag{5.1}$$

where z_{R} is the Rayleigh range, and P is the power at the specific time slice of the laser pulse. It is usually preferable to use a lens to aid the self-focusing so that the filamentation can start within a shorter propagation range. In this case the effective focal length becomes $z_{\mathrm{f}'} = 1/(z_{\mathrm{f}}^{-1} + f^{-1})$, where f is the focal length of the lens. As illustrated in Fig. 5.1, a particular time slice is focused to a high intensity spot, defocused by the plasma, then is refocused back from the plasma-free region, and the whole process repeats itself. The filament is therefore formed by the axially moving hot spot ("core") originated from each time slice of the pulse undergoing such defocusing and refocusing, and it is surrounded by a low intensity halo, or "background reservoir" [23, 140, 141], which is composed of the unfocused and defocused portion of the pulse. This process significantly distorts the pulse shape both spatially and temporally, and is accompanied by interesting phenomena such as continuum generation [133], conical emission [141], and intensity (and also electron density) clamping [30, 142, 143]. The reservoir is found to be vital for filamentary propagation [144]. An example of a long-range femtosecond laser filament in air imaged by a CCD camera is shown in Fig. 5.2(a), and the extended fluorescence track is due to the radiative recombination [129]. Figure 5.2(b) shows transverse laser beam profiles at the end of the filament at different pulse energies (peak powers) [112], and the onset of the filament can be seen when $P > P_{\mathrm{cr}}$, with the presence of the bright core surrounded by the background reservoir.

For filamentation formation in atmosphere, simulations [130, 145, 146, 147] have predicted typical peak electron densities anywhere from $\sim 10^{12}$ through 10^{17} cm^{-3} depending on laser and focusing conditions. Many experimental methods have been developed and have also produced estimates in this range, including plasma

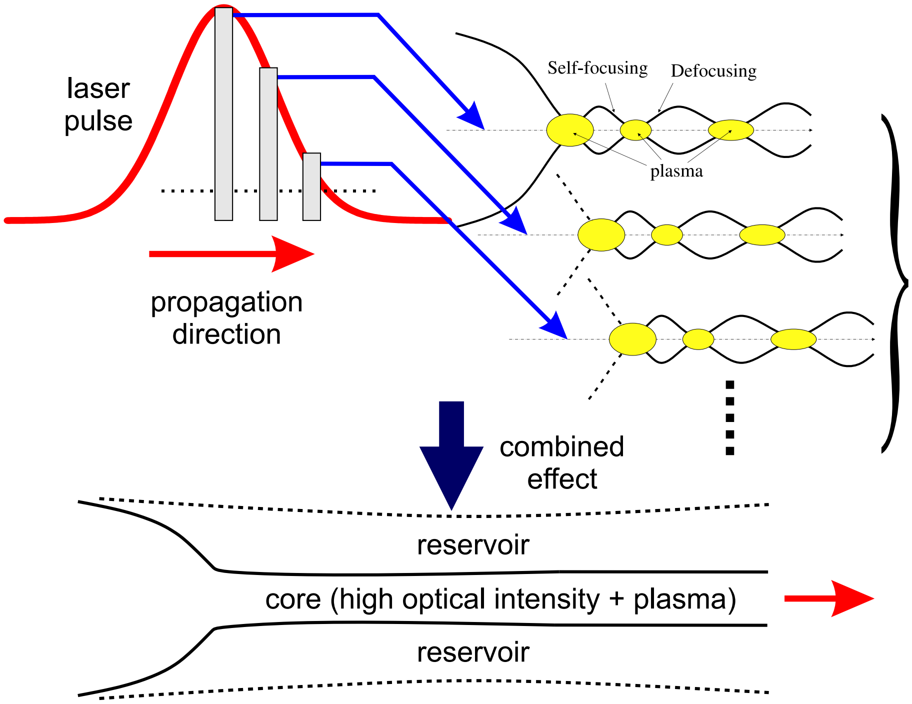

Figure 5.1: A simplified pictorial illustration of the moving-focus model, after Ref. [130].

fluorescence [148], secondary electrical discharges [149], fluorescence spectroscopy [150], longitudinal spectral interferometry [151], shadowgraphy and optical diffraction [152, 153], and electron conductivity [154]. However, all of these techniques are indirect methods, which either have no spatial resolution or require the precise prior knowledge of the laser pulse, and thus can only be considered as methods for crude estimation. Given the centrality of the electron density profile to the physics and applications of femtosecond filaments, the prior literature's lack of direct space- and time-resolved measurements is striking.

An issue in the study of atmospheric filamentation is that the physics of the optical nonlinearity has been long incorrectly perceived. Nonlinear propagation originates from the distortion of the electron clouds of atoms by the intense laser pulse, leading to an ensemble-averaged dipole moment nonlinearly increasing with

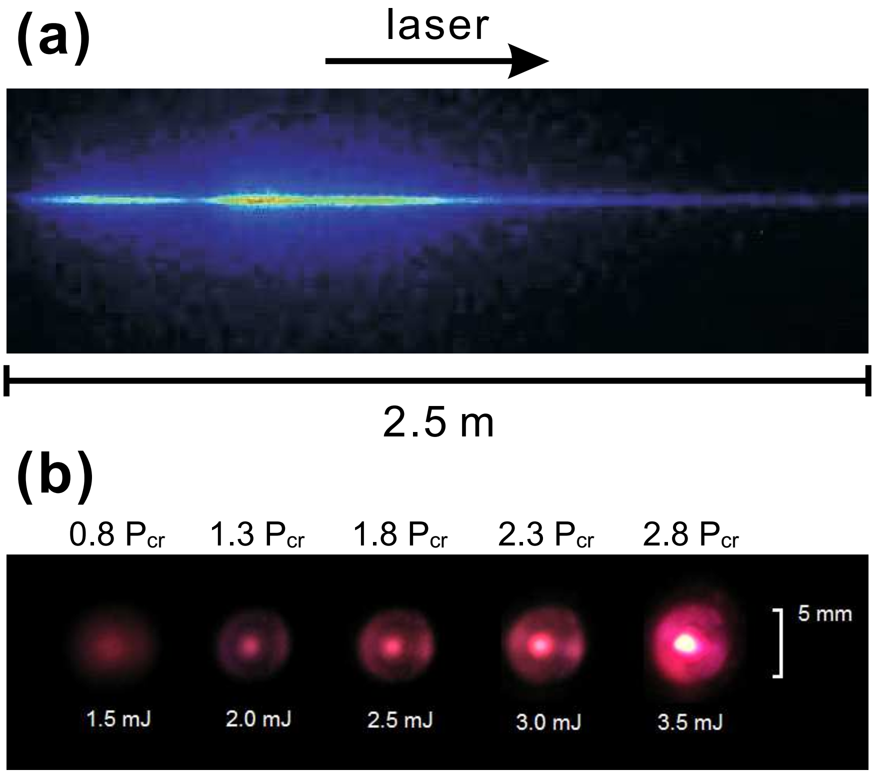

Figure 5.2: (a) Measured nitrogen fluorescence originates from a long-range femtosecond laser filament in air (from Ref. [129]), (b) the transverse beam profiles near the end of the filament in air at various laser pulse energies (peak powers), showing the onset of the filament core when $P > P_{\text{cr}} \sim 10$ GW, with the surrounding background reservoir (from Ref. [112]).

field strength. Moreover, as discussed in Chapter 3, in linear gas molecules, the increase of dipole moment can be also caused by the field-induced molecular alignment. As it will be seen later, for air molecules N_2 and O_2 the response timescale of the orientational effect at room temperature is $\delta t_{\text{rot}} \sim 20$–$40$ fs, therefore for a pulse duration $\leq \delta t_{\text{rot}}$, the majority of the nonlinearity the laser pulse experiences is electronic, while the role of molecular inertia emerges when the pulse duration $> \delta t_{\text{rot}}$. The results of Chapter 4 showed that the N_2 and O_2 molecular alignment contributes much more to the nonlinear index shift than the prompt response $n_2 I$ in the vicinity of the pump pulse at longer pulse duration ($> \delta t_{\text{rot}}$), which contradicts the previous result reported in 1997 [123]. As mentioned in Chapter 4, the authors of Ref. [123] reached a conclusion that the nonlinear index contributions are approximately the same size for prompt and orientational effects, which was measured by the less adequate method of spectral modulation by propagation. The magnitude of the nonlinear contribution from alignment of air molecules has been underestimated since then, in both simulation (for example, Ref. [155]) and interpretation of experimental results (for example, Ref. [154]).

A recent paper reported that the filamentation critical power P_{cr} in air increased with decrease of the laser pulse duration [156], implying the contribution of molecular rotation is not negligible for longer pulses. However, this observation was qualitative, without detailed characterization of the filament nor a quantitative approach to clarify the delayed effect enhancing the nonlinearity. Another two experiments showed pulse duration effect on filaments by measuring the beam profile axial evolution [157] and electrical conductivity [154]. This Chapter presents for the first time direct time-resolved measurements of electron density profiles along and across the path of the filamenting pulse. These measurements allow the identification of the molecular rotational response of nitrogen and oxygen as the dominant contribution to extended atmospheric filament dynamics.

5.2 Experimental setup

Interferometry is a standard tool in experimental plasma physics, and it has been successfully employed in the past to transversely probe, for example, plasma channels generated from the line-focus of the axicon [158] or relativistic self-guiding [159] with electron density $n_e \gtrsim 10^{18}$ cm^{-3}. However in atmospheric filaments the range of electron density $n_e \sim 10^{12}$–10^{17} cm^{-3} (depending on laser and focusing conditions) is too low to register a phase shift distinguishable from the background noise in an optical probe beam. The remedy is to intersect an interferometric probe beam through the filament at a near-grazing angle, which increases the interaction length and phase sensitivity. While maintaining excellent radial spatial resolution as in the conventional method, the price paid for the small probe crossing angle is reduced axial spatial resolution. However, this is of little concern for meter-scale length filaments. This technique allows measurement of plasma density as low as $\sim 10^{15}$ cm^{-3}.

In the experiment described here, the filament is generated by focusing a multi-millijoule pump pulse from a Ti:Sapphire laser in air. To produce a single, long filament, the f number of the focusing system is tuned by an iris immediately after the focusing lens. The experimental setup is shown in Fig. 5.3. A low energy probe beam with ~ 1 ps delay is split from the pump beam, counter-propagated at an angle $\theta = 0.75°$ across the filament. The scheme of counter-propagating pump and probe fully isolates the pump beam from the imaging system, preventing strong pump light from interfering with the probe imaging. The plane central to the crossing region is relayed and imaged to a CCD camera by a pair of relay lenses (L) and a microscope objective (O), with a spatial resolution of 1.55 μm/pixel. During alignment of the imaging system, a fine metal wire mesh with 12.5 μm wire diameter and 215 μm grid spacing is placed at the central crossing plane for determining the

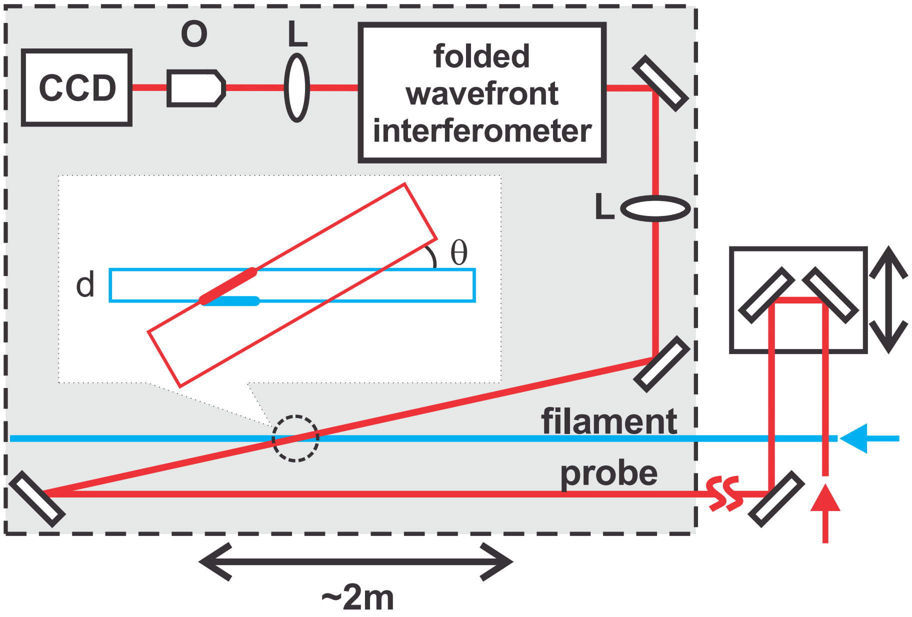

Figure 5.3: Experimental interferometry setup, showing imaging lenses (L) and the microscope objective (O). The inset shows the filament width d and probe crossing angle θ.

spatial resolution and calibration. The variable probe delay allows the filament to be imaged at different times.

A folded wavefront interferometer is installed between the two relay lenses and splits the probe beam into two replicas with variable delays, and nearly-collinearly recombines them so that they partially overlap on the CCD camera with slightly different incident angles, forming an interference fringe pattern on the detector chip. Because the probe beam size is much larger than the transverse dimension of the filament, it is possible to spatially overlap a region of the beam containing the filament-induced phase shift with a region of the replica with no phase shift. The setup is rail-mounted and is translatable along the full filament, which allows sampling of axial locations.

For the typical measured filament diameters of $d_{\text{fil}} \sim 70\ \mu\text{m}$ (shown later), the probe path through the plasma is $d_{\mathrm{probe}} \sim d_{\mathrm{fil}}/\sin(\theta) \sim 5$ mm, the axial spatial resolution along the filament is $\Delta z_{\mathrm{res}} \sim d_{\mathrm{fil}}/c \sim 5$ mm, the temporal resolution is $\Delta t_{\mathrm{res}} = \Delta z_{\mathrm{res}}/c \sim$ 10–15 ps, and the radial resolution is 5 μm. Crucial to the ability to extract the very small optical phase shifts imposed by the low filament electron densities is (i) the extended probe interaction length d_{probe} and (ii) a very high quality probe phase front imposed by a spatial filter. It has been verified that d_{probe} is sufficiently short for the filament densities that negligible refractive distortion of the probe phase front occurs. The resolution limit is set by residual phase front noise $|\delta\Phi_{\mathrm{noise}}| \sim 6$ mrad in the probe which sets the measurable lower bound density to $\sim 5 \times 10^{14}$ cm^{-3}.

The interferograms are analyzed by standard techniques as seen in, for example, Ref. [158]. First the phase shift is retrieved using the Fourier transform method developed by Takeda *et al.* [73]. A sample raw interferogram obtained at $\sim$ 1 ps probe delay and the corresponding retrieved phase shift are shown in Fig. 5.4(a) and Fig. 5.4(b), respectively. Note that the 2-D phase in Fig. 5.4(b) shows a shape corresponding to the left half of a “bow tie”. The narrowest region to the right represents the section of the filament crossing the object plane of the imaging system, and more detail of this feature will be discussed later. The radial electron density profile is extracted from the vertical lineout of the phase shift at this in-focus region using Abel inversion. For fast inversion speed we use an algorithm based on fast Fourier transform proposed by Kalal and Nugent [160]. The retrieved phase shift was averaged over 200 laser shots before Abel inversion.

The fluctuation of pump beam pointing is unavoidable due to ambient air flow

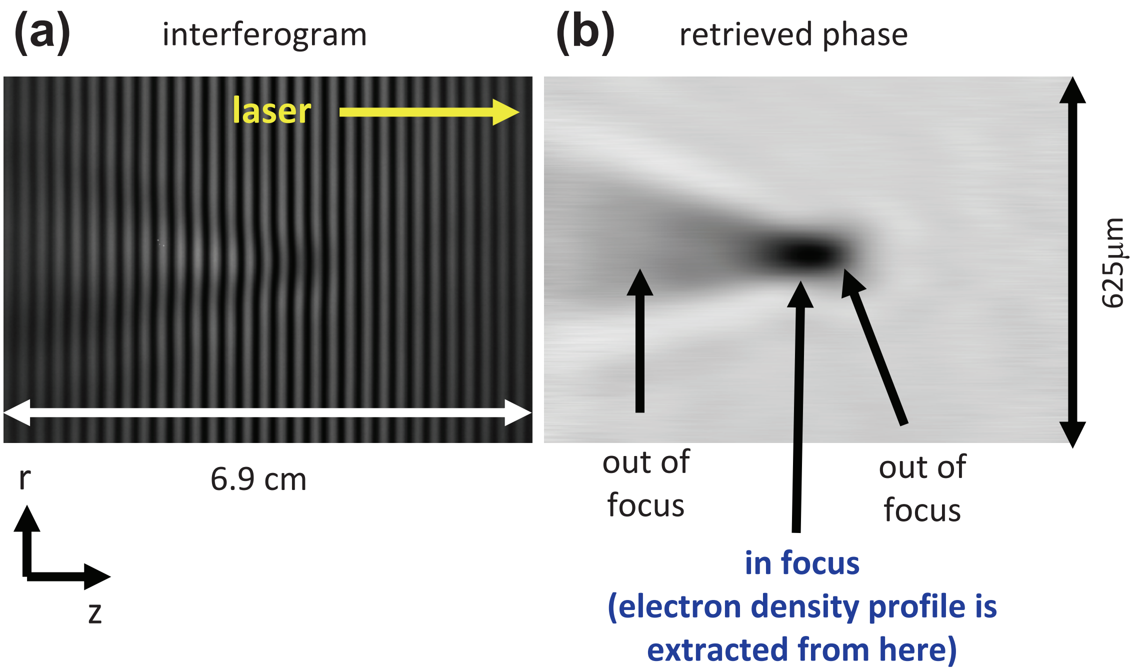

Figure 5.4: (a) A sample interferogram of a single filament, and (b) the retrieved phase.

and mechanical vibration in the laboratory environment, leading to slight shot-to-shot transverse movement of the filament as well as random shift of the "bow tie" on the retrieved 2-D phase images. Therefore prior to averaging, all the "bow-tie" shapes on the phase images were spatially aligned by an algorithm based on 2-D cross-correlation. The procedure is to choose a phase image $\phi_1(x, y)$ as the reference and compute its autocorrelation

$$C_{11}(x, y) = \int_{-\infty}^{\infty}\int_{-\infty}^{\infty} \phi_1^*(x', y')\phi_1(x' + x, y' + y)dx'dy', \tag{5.2}$$

and find out its peak location (x_1, y_1). Also compute the cross-correlations between $\phi_1(x, y)$ and the rest of the $N - 1$ images $\phi_q(x, y)$ $(q \in 2, 3 \cdots N)$:

$$C_{1q}(x, y) = \int_{-\infty}^{\infty}\int_{-\infty}^{\infty} \phi_1^*(x', y')\phi_q(x' + x, y' + y)dx'dy', \tag{5.3}$$

and find out the peak locations (x_q, y_q). Assuming that the "bow-tie" feature on each image is nearly identical and that the background noise is negligible, then the relative shift of the "bow ties" on two images $\phi_q(x, y), \phi_1(x, y)$ is $(\Delta x, \Delta y) = (x_q - x_1, y_q - y_1)$. One can substantially speed up the computation using fast Fourier transform with the cross-correlation theorem $\widetilde{C}_{pq}(k_x, k_y) = \widetilde{\phi}_p{}^*(k_x, k_y)\widetilde{\phi}_q(k_x, k_y)$, where $\widetilde{C}_{pq}$, $\widetilde{\phi}_p$, and $\widetilde{\phi}_q$ are Fourier transforms of C_{pq}, ϕ_p, and ϕ_q, respectively. Moreover, data binning was performed by rejecting those "bow tie" images with in-focus lineout widths and peak phase shifts that fall beyond a standard deviation of the mean.

5.3 Results

As has been well-visualized by simulations [145, 146, 147, 130], a femtosecond filament in gas starts as a result of rapid self-focusing instability arrested by plasma formation and defocusing. This abrupt beam collapse and electron density onset have been observed as shown in Fig. 5.5, for the case of a 2.85 mJ, 72 fs pulse (40 GW) focused at f number $= f_\# = 345$ (lens focal length $f = 224$ cm, beam diameter $= 6.5$ mm) by using a probe delay $\Delta t_{\text{probe}} = 50$ ps. The frames show a sequence of 1-cm-spaced axial positions of the interferometer object plane, (i) $z = -39$ through (vi) -34 cm, where $z = 0$ is the lens focal plane.

It is first worth explaining the characteristic "bow-tie" shape of the phase images. These reflect the short (~ 1 mm) depth of field of the imaging system: the wide sections are out-of-focus regions on either side of the object plane, which is tightly imaged at the bow-tie center. The local filament axial and radial density profile (see Fig. 5.8) is obtained from phase extraction only at the center of the bow tie. In frame (i) of Fig. 5.5(a) , at $z = -39$ cm, only the right side of the bow tie is visible; there is no filament electron density at the object plane and upstream of it. Inspection of the object plane and upstream region in frames (ii) and (iii) shows the abrupt onset of ionization at $z > -38$ cm, while frames (iv)–(vi), looking back along the filament at increasing distances, show the filament's continued upstream development. The terminated right side of the bow tie is the leading temporal edge of the filament; the interferometer probe temporal delay was here adjusted to catch the filament midflight. Both far downstream from the collapse point and at longer probe time delays, the bow tie extends and widens to both the left and right edges of the frame. Note that in this specific measurement shown in Fig. 5.5(a) the probe delay is ~ 50 ps, which is much longer than that in Fig. 5.4 (~ 1 ps), hence the right part of the "bow tie" is more significant on the phase images. Also note that this experimental apparatus is capable of resolving two or multiple filaments, as shown in Fig. 5.5(b).

Although the temporal resolution of this experimental apparatus is limited to ~ 10 ps, it is sufficient to study the plasma density decay which is typically in sub-ns timescale in the filament, due to radiative and non-radiative recombination of electrons and ions [161], and electron attachment to neutral atoms (molecules) such as O_2 [152]. In the radiative recombination an electron is captured by an ion with emission of a photon. The non-radiative recombination is a three-body process in which two electrons and an ion are involved, resulting in an electron and an neutral atom. The measured on-axis electron density decay of a filament at $z = -3.5$ cm in

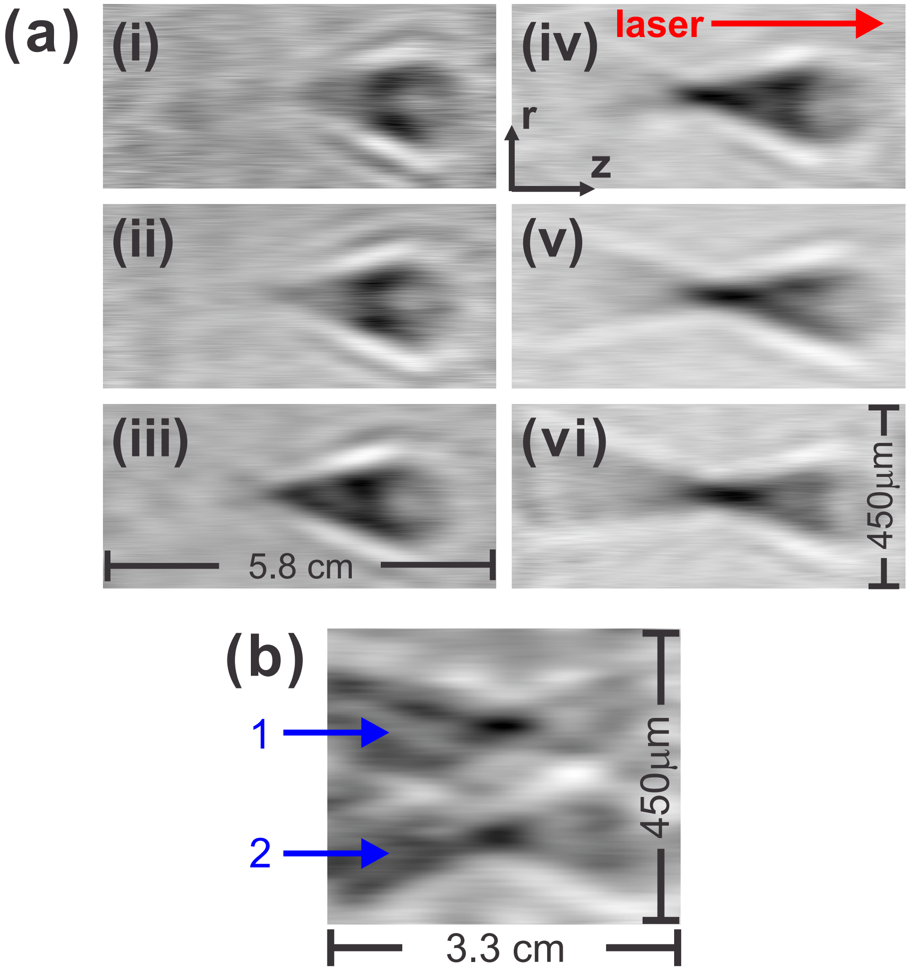

Figure 5.5: (a) Spatial sequence of bow-tie phase images showing filament collapse, for a 2.85 mJ, 72 fs pulse focused at $f_{\#} = 345$. The frames show a sequence of 1-cm-spaced axial positions of the interferometer object plane, (i) $z = -39$ cm through (vi) $z = -34$ cm, (b) two filaments are generated and recorded at the same time, showing the capability of spatially-resolved measurement.

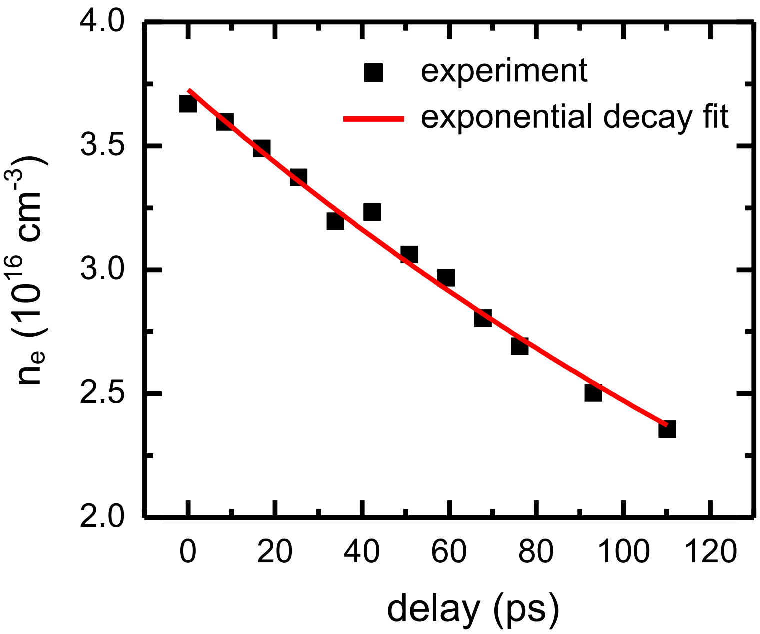

Figure 5.6: On-axis plasma density decay (squares) in a filament at the axial distance $z = -3.5$ cm to the focus, for pulse duration $\tau = 40$ fs, peak power $P = 19$ GW, lens focal length $f = 95$ cm, and $f_{\#} = 240$. An exponential decay time constant 244 ps is obtained by fitting the measured density vs probe delay (solid curve).

the first 100 ps probe delay is shown in Fig. 5.6, and it can be seen that at 110 ps delay the density drops by more than 30%. In this measurement, the laser and the focusing parameters are: pulse duration $\tau = 40$ fs, peak power $P = 19$ GW, lens focal length $f = 95$ cm, and $f_{\#} = 240$. An exponential decay fit gives a $1/e$ time constant 244 ps, which is close to the results given by Ref. [153] using transverse optical diffraction method.

The ability to directly measure the electron density with good axial resolution allows a sensitive test of filament propagation physics. One of the most discussed aspects of filamentation has been the nature of the neutral gas nonlinearity first leading to beam collapse and later contributing to the dynamic stabilization. Part of the air nonlinearity is an instantaneous response owing to electron cloud nonlinear distortion in argon atoms and within N_2 and O_2 air molecules. It has also long been recognized [123] that molecular rotation in the laser field contributes a delayed nonlinearity resulting from the increased dipole moment as the molecular axis is torqued toward the laser polarization. In Chapter 4, it has been suggested that the orientational effect is in fact dominant at the typical $\sim$ 100 fs pulse lengths and $\sim$ mJ energy levels used for a majority of air filamentation experiments. This is because the filamenting pulse, in the intensity range 10^{13}–10^{14} W/cm^2, typically excites $\sim$ 20–30 rotational quantum states in N_2 and O_2, resulting in a refractive index response time due to rotation alone of $\delta t_{\text{rot}} \sim 2\pi/\omega_{j_{\text{high}}} = 2T_{\text{rev}}/j_{\text{high}}(j_{\text{high}} + 1) \sim$ 20–40 fs, where $\omega_{j_{\text{high}}}$ is the angular frequency of the wavefunction associated to the highest rotational eigenstate $|j_{\text{high}}\rangle$ excited by the laser pulse, and T_{rev} is the fundamental molecular rotation period (or alignment revival period) defined in Chapter 3 ($T_{\text{rev},N_2} = 8.3$ ps for nitrogen and $T_{\text{rev},O_2} = 11.6$ ps for oxygen [109]).

To illustrate the profound effect of changes in the laser pulse duration on air filamentation, experiments with two different focusing geometries were performed, keeping the peak laser power fixed for each: (a) $f = 95$ cm, $f_{\#} = 240$, laser peak power $P = 17$ GW, $\tau_{\text{short}} = 40$ fs, and $\tau_{\text{long}} = 120$ fs and (b) $f = 306$ cm, $f_{\#} = 505$, $P = 19$ GW, $\tau_{\text{short}} = 44$ fs, and $\tau_{\text{long}} = 132$ fs. Here, τ refers to the FWHM pulse widths measured immediately after the lens by a field envelope and phase diagnostic [86] and a single-shot autocorrelator. The pulse width was adjusted by translating the laser's compressor grating, and it was verified that this amount of chirp had no effect on the results. In all experiments, the power was carefully adjusted to avoid development of hot spots in the beam prior to the lens or multiple filamentation as

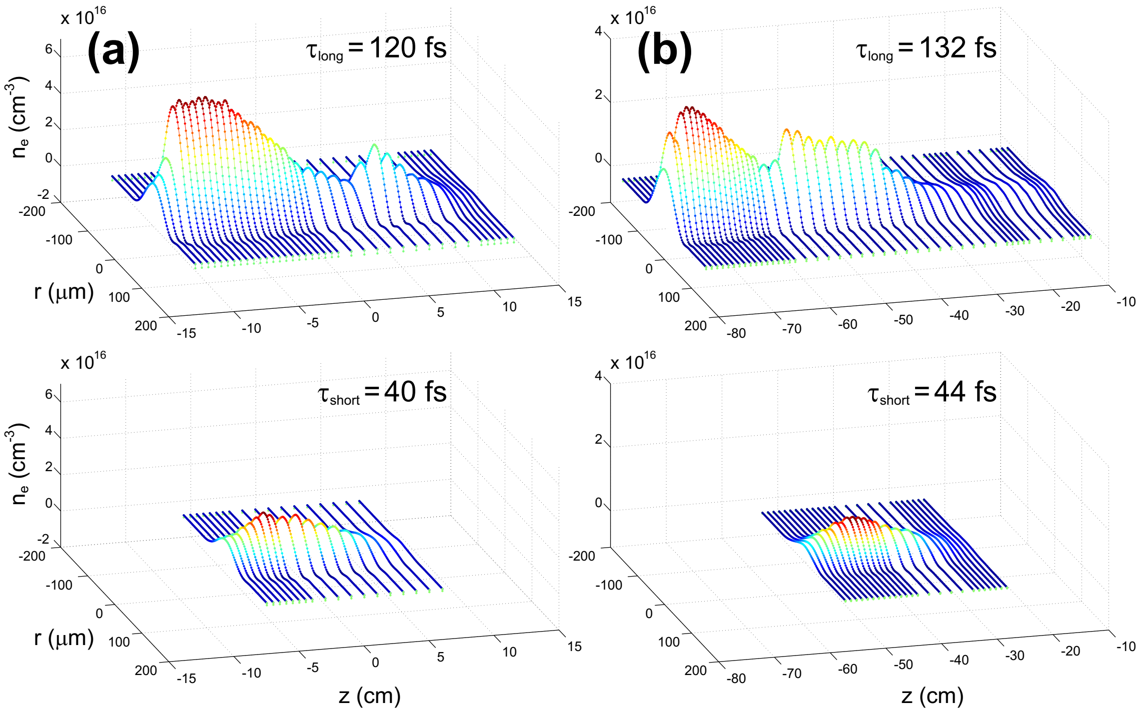

Figure 5.7: 200-shot-averaged radial electron density profiles vs axial distance for (a) lens focal length $f = 95$ cm, $f_{\#} = 240$, laser peak power $P = 17$ GW, $\tau_{\text{long}} = 120$ fs (upper panel), and $\tau_{\text{short}} = 40$ fs (lower panel) and (b) $f = 306$ cm, $f_{\#} = 505$, $P = 19$ GW, $\tau_{\text{long}} = 132$ fs (upper panel), and $\tau_{\text{short}} = 44$ fs (lower panel).

seen by multiple white light spots on a screen in the far field. The interferometer probe delay was set to $t_{\text{probe}} \sim 1$ ps (rapid drop of the density in the first 100 ps was measured as shown earlier). It is observed that the length, structure, and density of measured filaments is quite sensitive to minor distortions in the beam, either from optics or from hot spots due to accumulation of nonlinear phase in air in advance of the lens. A clean beam is essential for comparing experiments to propagation simulations.

The measured radial profiles of the electron density with respect to the axial positions for conditions (a) and (b) mentioned above are shown in Fig. 5.7(a) and Fig. 5.7(b), respectively, with results for τ_{long} in upper panels and τ_{short} in lower panels. Figure 5.8(a) shows the on-axis filament electron density (left panel) n_e and FWHM diameter d_{fil} (right panel) as a function of axial position, corresponding to $f_{\#} \sim 240$ and conditions (a) above. Peak $n_e \sim 6.5 \times 10^{16}$ cm^{-3} (corresponding to fractional ionization $\eta \sim 2.4 \times 10^{-3}$) occurs at $z \sim -9$ cm for τ_{long}, while peak $n_e \sim 2.4 \times 10^{16}$ cm^{-3} ($\eta \sim 10^{-3}$) occurs at $z \sim -3$ cm for τ_{short}, with τ_{long} resulting in stronger self-focusing and more rapid collapse, higher peak density, and longer overall filament length. For both pulses, d_{fil} is quite stable over the filament length, except near the end. A notable difference is a secondary electron density peak at $z \sim 5$ cm for τ_{long}. Both filaments are quite different from the case of propagation in very low air density, where a simulation (described below) for τ_{short} shows an axial density distribution peaking at $\eta = 10^{-5}$, with an axial FWHM of ~ 10 cm centered at $z = 0$. For τ_{long}, the low density simulation shows an even smaller η and axial extent.

For $f_{\#} \sim 505$ and conditions (b) above, Fig. 5.8(b) shows an earlier axial beam collapse and filament onset for τ_{long} than for τ_{short}, with the entire measurable filament located in advance of $z = 0$ in both cases. The peak density for τ_{long} is 3.6×10^{16} cm^{-3} ($\eta \sim 10^{-3}$), while that for τ_{short} is 1.1×10^{16} cm^{-3}. d_{fil} for both pulses is in the range ~ 65–80 μm, with widening near the end of the measurable filament. Here, as in the small $f_{\#}$ case, τ_{long} results in stronger self-focusing, higher peak density, longer overall filament length, and the appearance of a prominent secondary density peak. By contrast, low density simulations for these conditions show $\eta < 10^{-7}$ centered at $z = 0$.

Figure 5.9 compares filament output on-axis spectra for τ_{long} and τ_{short} for

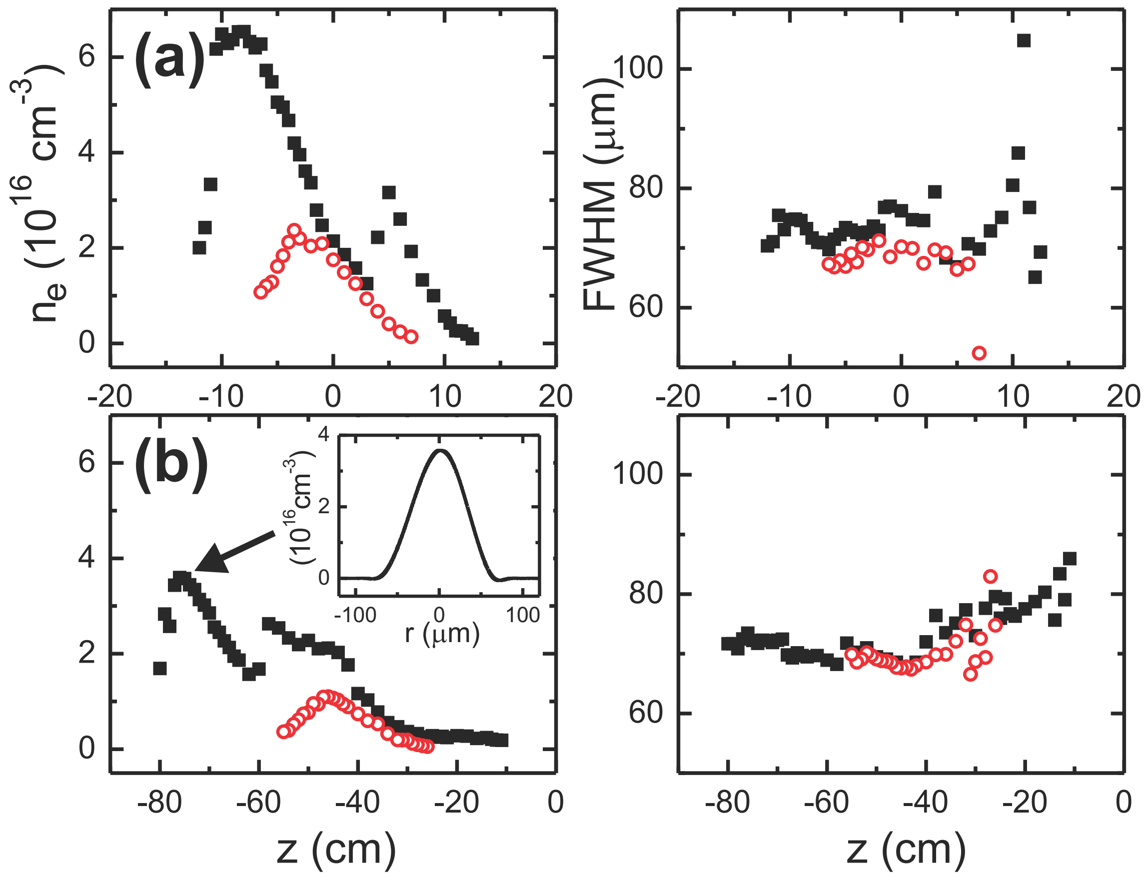

Figure 5.8: On-axis electron density and filament FWHM vs axial distance acquired from Fig. 5.7, for (a) lens focal length $f = 95$ cm, $f_{\#} = 240$, laser peak power $P = 17$ GW, $\tau_{\text{short}} = 40$ fs (red circles), and $\tau_{\text{long}} = 120$ fs (black squares) and (b) $f = 306$ cm, $f_{\#} = 505$, $P = 19$ GW, $\tau_{\text{short}} = 44$ fs (red circles), and $\tau_{\text{long}} = 132$ fs (black squares). Each point is a 200-shot average. The inset in (b) shows a sample electron density profile from $z = -75$ cm. Peak values shown have $\sim 20\%$ uncertainty near the collapse point and $\sim 10\%$ over the rest of the filament.

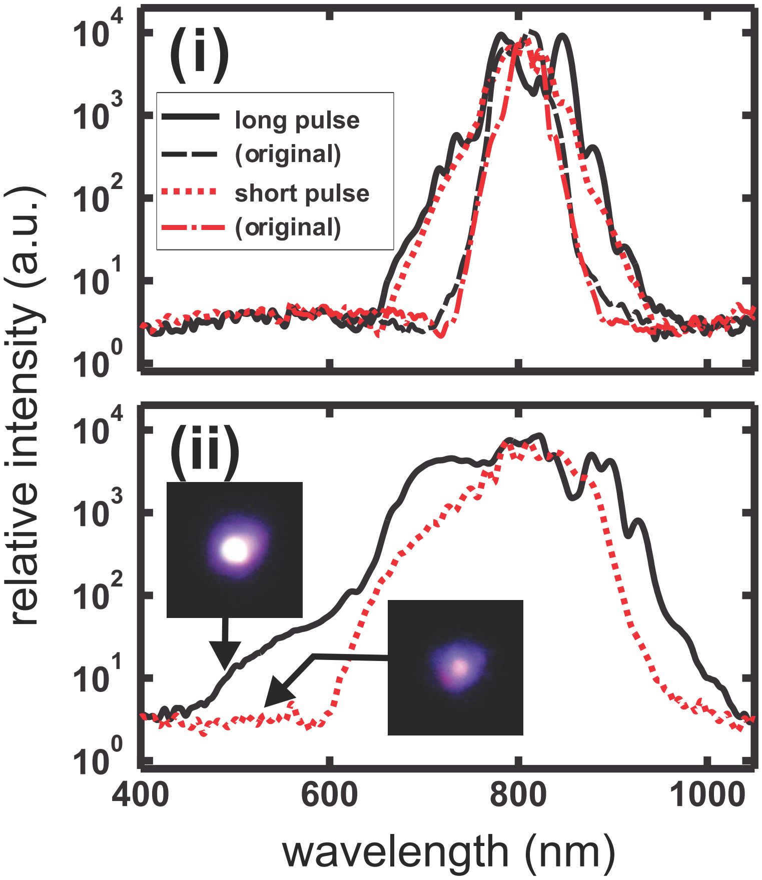

Figure 5.9: On-axis filament spectra corresponding to the conditions of Fig. 5.8, with (i) $f_\#=240$ and (ii) $f_\#=505$. Also shown are the input spectra. The insets in (ii) show the filament spots on a far field screen for τ_{short} and τ_{long}.

the two focusing cases. The input spectra for the long and short pulses are shown as thinner curves. In all cases the output spectrum for τ_{long} is wider and more intense, owing to the greater effective nonlinearity and extended interaction length experienced by that pulse. For the $f_\# \sim 505$ filament of panel (ii), the enhanced spectral broadening for τ_{long} is particularly strong, and images of the filament white light spots are shown as insets.

5.4 Simulation

The intense femtosecond pulse propagation in air is simulated by using the code WAKE [147, 162], assuming a cylindrically symmetric, extended paraxial wave equation for the laser pulse:

$$\frac{2}{c}\frac{\partial}{\partial s}\left(i\omega_0+\frac{\partial}{\partial\tau}\right)a-\beta_2\frac{\partial^2 a}{\partial\tau^2}+\nabla_\perp^2 a=\left(\frac{4\pi q^2 n_e}{mc^2}-k_0^2\delta\varepsilon\right)a. \tag{5.4}$$

Here, $a(\mathbf{x}_\perp,\tau,s)$ is the complex envelope of the laser electric field, k_0 and ω_0 are the central wave number and frequency of the initial pulse, respectively, $\mathbf{x}_\perp$ is the transverse coordinate, $s=z$ is propagation distance, $\tau=t-z/v_g$ is time local to the pulse frame moving at group velocity v_g, $\beta_2=k_0(d^2k/d\omega^2)|_{\omega=\omega_0}$ is the group velocity dispersion of air, $q=-e$ is the electron charge, n_e is the electron density generated by laser ionization, and $\delta\varepsilon(\mathbf{x}_\perp,\tau)=\delta\varepsilon_{\text{rot}}+\delta\varepsilon_{\text{inst}}$ is the nonlinear dielectric response. $\delta\varepsilon_{\text{rot}}$ is modeled as a damped oscillator

$$\left(\frac{d^2}{d\tau^2}+2\gamma_D\frac{d}{d\tau}+\omega_m^2\right)\delta\varepsilon_{\text{rot}}\left(\mathbf{x}_\perp,\tau\right)=2\omega_m^2 n_{20}I\left(\mathbf{x}_\perp,\tau\right) \tag{5.5}$$

with $I(\mathbf{x}_\perp,\tau)\propto|a|^2$, and where $2\pi/\omega_m=400$ fs, $\gamma_D=120$ fs, and $n_{20}=2.6\times10^{19}$ cm^2/W are obtained from fits to the prior ultrafast measurements of weighted N_2 and O_2 rotational response in Chapter 4. Ignored are later-time rotational quantum revivals. In the prior measurements, a comparatively negligible instantaneous response in N_2 and O_2 was observed for $\tau<\delta t_{\text{rot}}$, and here $\delta\varepsilon_{\text{inst}}^{\max}/\delta\varepsilon_{\text{rot}}^{\max}<0.15$ is used as an upper bound setting the value of n_2 in $\delta\varepsilon_{\text{inst}}=2n_2I(\mathbf{x}_\perp,\tau)$. Therefore, at long times $\tau \gg 2\pi/\omega_m$, $\delta\varepsilon(\mathbf{x}_\perp, \tau) \sim 2(n_{20} + n_2)I(\mathbf{x}_\perp, \tau)$, where the value for $n_{20} + n_2 \sim 3.0 \times 10^{19}$ cm^2/W corresponds closely with measured "n_2" values for long pulses [130]. The apertured beam is modeled as a flat top with a smooth intensity transition to zero at 90% radius, while the phase was taken as a quadratic function of radius determined by the lens focal length. A fit to tunneling and multiphoton rates [163] was used to simulate air ionization, as this rate is higher than tunneling alone in the expected intensity range of mid-10^{13} W/cm^2. For the parameters used in the simulation, the paraxial approximation is sufficient.

Simulation results for on-axis filament density and filament diameter vs axial position are shown in Fig. 5.10 for the focusing geometries, peak powers, and pulse widths of Fig. 5.8, plus additional runs at 20% higher power. The additional runs were performed because, for $f_\# \sim 505$ and τ_{short}, experimental filament onset was quite sensitive to energy: For the lower power case for τ_{short}, it is seen that the peak filament density drops by almost half.

The main qualitative features of the simulations are in agreement with the measurements. For the same peak power, the τ_{long} filaments start earlier and more abruptly, have significantly higher density, and are longer than those for τ_{short}. In addition, the τ_{long} filaments have multiple peaks as in the experiments. The absolute density values and filament extents are in good agreement for the $f_\# = 240$ case. For $f_\# = 505$, while the peak densities differ by $\sim 50\%$, the qualitative behavior is well-followed. Note that varying the simulation's ionization model varies the detailed shape of the radial electron density profile (but not the peak density; see further discussion below). A specific measure of width (such as FWHM) can

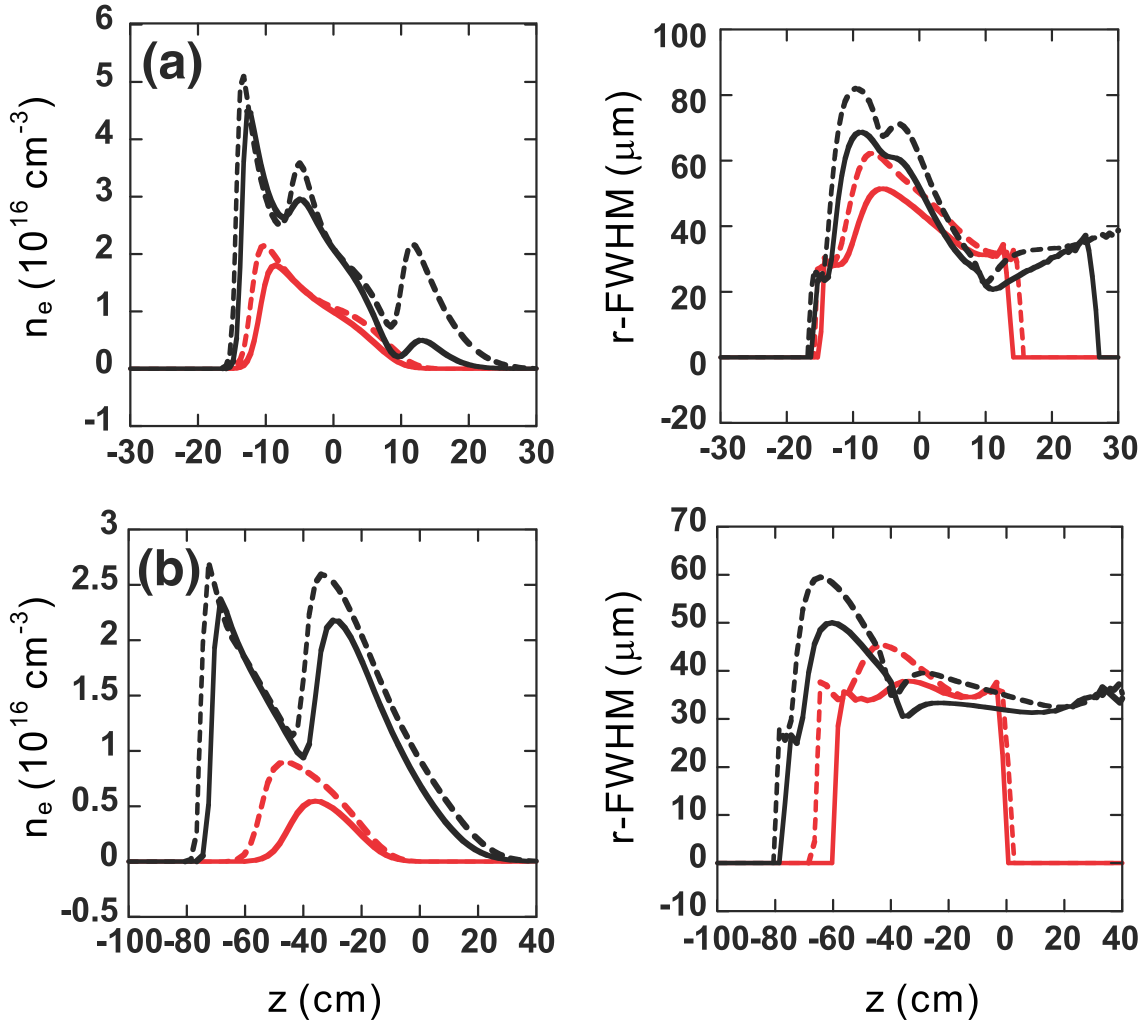

Figure 5.10: Simulation results for the conditions of Fig. 5.8 (solid lines). Additional runs have been performed at 20% higher power (dashed lines). Red, short pulse; black, long pulse.

then show variation for different ionization models used. The need to refine the ionization model may explain the difference between experimental and simulated filament FWHM.

The difference in long and short pulse results is a direct consequence of the dominance of the delayed nonlinear response of the air molecules, which leads to stronger nonlinear focusing and more extended propagation. The double electron density peaks originate from the variation of nonlinear focusing and refraction through the temporal envelope of the pulse: The leading portion loses energy and refracts away from its self-generated plasma, causing a dip in the electron density, while the trailing part accumulates sufficient nonlinear phase in the filament periphery to self-focus and cause a plasma resurgence [145, 146, 147]. In air, this effect is enhanced for longer pulses, since the later slices of the pulse experience increasing molecular rotational nonlinearity. The multiple density peaks are associated with pulse temporal splitting, which we have measured on-axis and will present in a future publication. The higher electron density for τ_{long} is simply the filament's dynamical offset of the stronger nonlinear focus of the excited molecular lens. The simulation's sensitivity to ionization model was tested by multiplying the rate by a factor of 20. This resulted in negligibly increased peak densities, reinforcing the idea that the density and intensity are clamped by a dynamic balance of plasma-induced refraction and self-focusing.

The experiments and simulations presented in this Chapter suggest a method to control density or intensity clamping in atmosphere by controlling the molecular excitation. To estimate the upper limit of the plasma density in molecular alignment-assisted filamentation, assuming that $-\Delta n_{\text{plasma,max}} = \Delta n_{\text{rot,max}}$, where $\Delta n_{\text{rot,max}} = (4\pi N/3)(0.8\Delta\alpha_{\text{N}_2} + 0.2\Delta\alpha_{\text{O}_2}) \approx 10^{-4}$ is the maximum shift of refractive index in air when every molecule is aligned along the laser polarization direction, leading to the electron density $n_{e,\text{max}} \approx 3.5 \times 10^{17}$ cm^{-3}. High degree (nearly 100%) of alignment has been demonstrated in N_2, using excitation of a pulse train spaced by the rotational revival period T_{rev} [164]. This may provide a route toward high-density, long-range filamentation in atmosphere.

Recently, it was claimed that filamentation in atmosphere takes place without plasma stabilization, based on the speculative assumption of negative higher-order Kerr indices [165]. The laser and focusing parameters for τ_{short} in Fig. 5.8(a) correspond closely to parameters simulated in Ref. [165] by that group. Their simulations predict electron densities almost 2 orders of magnitude smaller than experimental and simulation results in Fig. 5.8(a) and Fig. 5.10(a), casting doubt on the importance and perhaps existence of the negative higher-order Kerr indices.

5.5 Conclusion

In conclusion, the first direct space and time-resolved electron density measurements is presented for a nonrelativistic femtosecond laser pulse nonlinearly filamenting in gas, here the atmosphere. This has allowed a detailed elucidation of the nonlinear physics leading to atmospheric filament formation and a route to its enhancement.

Chapter 6

Conclusions and future directions

6.1 Optical nonlinearities of linear gas molecules

An improved, highly stable version of SSSI is developed for single-shot, 1-D-space- and time-resolved measurement of ultrafast evolution of refractive index in the optical medium. The rotational responses of various linear gas molecules to a femtosecond laser pulse are measured, and the results agree well with the calculations using quantum perturbation theory. In particular, the improved sensitivity of SSSI enables the measurement of laser-induced alignment revivals of D_2 and H_2, which are very weak in magnitude, for the first time at room temperature. However the experiments were conducted by focusing the laser pulse into a gas cell much longer than the Rayleigh range, giving rise to the difficulty of determining the interaction length. This problem can be solved by focusing the laser pulse in vacuum onto a gas jet produced by a nozzle with narrow exit orifice. As long as the width of the jet is much shorter than the Rayleigh range, the laser intensity can be regarded as constant when propagating through the gas. This makes direct extraction of refractive index shift Δn from the measured phase shift $\Delta\Phi$ possible, eliminating the calibration process requiring a n_2 value of Ar from other literatures, as shown in Chapter 2.

It is found that for N_2, O_2, and N_2O, the delayed molecular effect dominates the prompt electronic response in nonlinear shift of the refractive index induced by a $\sim$ 100 fs laser pulse. However the magnitude of the prompt response is not determined because the pulse duration used in the experiment is much longer than the characteristic response timescale of the molecule ($\sim$ 40 fs for N_2 and O_2), so that the small prompt index shift $n_{2,\text{inst}}I$ cannot be distinguished from the relatively larger orientational response. Using a very short ($<$ 40 fs) laser pulse, it is possible to identify the contribution of the prompt nonlinearity and extract $n_{2,\text{inst}}$ values of these linear gas molecules from SSSI measurement. Because the prompt and the delayed nonlinearities result in different polarization dependence of the refractive index (birefringence), one can perform two measurements with pump polarization parallel and perpendicular to the probe, which may further help to discriminate both nonlinearities.

6.2 Laser filamentation in atmosphere

This research also presents the first space- and time-resolved electron density measurements for a non-relativistic femtosecond laser pulse nonlinearly filamenting in gas, here the atmosphere, with the lower detection limit of electron density $\sim 5\times10^{14}$ cm^{-3}. This is achieved by using optical interferometry with a nearly-grazing incident probe beam, while maintaining reasonable axial and temporal resolutions. The probe wavelength used here is 800 nm, and a possible improvement is to extend the detection limit by increasing the wavelength. For example, by employing a femtosecond fiber laser at 1.5 μm as the probe, the minimum measurable electron density will be lowered by a factor of ~ 2, enabling better study of extremely weak ionization, which is the case near the end of a long filament in air.

Dramatically different filaments are observed from both experiments and simulations when using the same laser peak power but different pulsewidth, leading to the conclusion that the dominant nonlinearity responsible for extended air filamentation is rotational. This suggests that the properties of a filament in atmosphere, such as density or intensity clamping, can be controlled by manipulating the orientational effect of air molecules. As mentioned in Chapter 5, one may use a train of pulses to excite high degree of molecular alignment, which may be helpful for long-range filamentary propagation with higher electron density.

This work also helps to clarify whether the higher order Kerr effect plays a significant role in the filamentation process [165], as the author noticed that recently there is a debate over this issue [166, 167, 168, 169, 170]. In Chapter 5, the experiment results show satisfactory agreement with the simulations based on the "standard" (plasma refraction with reduced role of instantaneous n_2) model, thus it is found unnecessary to introduce negative high order Kerr indices claimed by Ref. [171].

Appendix A

List of publications by the Candidate

1. Y.-H. Chen, S. Varma, I. Alexeev, and H. M. Milchberg, "Measurement of transient nonlinear refractive index in gases using xenon supercontinuum single-shot spectral interferometry," Opt. Express **15**, 7458 (2007).
2. Y.-H. Chen, S. Varma, A. York, and H. M. Milchberg, "Single-shot, space- and time-resolved measurement of rotational wavepacket revivals in H_2, D_2, N_2, O_2, and N_2O," Opt. Express **15**, 11341 (2007).
3. B. D. Layer, A. York, T. M. Antonsen, S. Varma, Y.-H. Chen, Y. Leng, and H. M. Milchberg, "Ultrahigh-Intensity Optical Slow-Wave Structure," Phys. Rev. Lett. **99**, 035001 (2007).
4. Y.-H. Chen, S. Varma, and H. M. Milchberg, "Space- and time-resolved measurement of rotational wave packet revivals of linear gas molecules using single-shot supercontinuum spectral interferometry," J. Opt. Soc. Am. B **25**, B122 (2008).
5. S. Varma, Y.-H. Chen, and H. M. Milchberg, "Trapping and Destruction of Long-Range High-Intensity Optical Filaments by Molecular Quantum Wakes in Air," Phys. Rev. Lett. **101**, 205001 (2008).
6. B. D. Layer, A. G. York, S. Varma, Y.-H. Chen, and H. M. Milchberg, "Periodic index-modulated plasma waveguide," Opt. Express **17**, 4263 (2009).
7. Z. W. Wilkes, S. Varma, Y.-H. Chen, H. M. Milchberg, T. G. Jones, and A. Ting, "Direct measurements of the nonlinear index of refraction of water at 815 and 407 nm using single-shot supercontinuum spectral interferometry," Appl. Phys. Lett. **94**, 211102 (2009).
8. S. Varma, Y.-H. Chen, and H. M. Milchberg, "Quantum molecular lensing of femtosecond laser optical/plasma filaments," Phys. Plasmas **16**, 056702 (2009).
9. Y.-H. Chen, S. Varma, T. M. Antonsen, and H. M. Milchberg, "Direct Measurement of the Electron Density of Extended Femtosecond Laser Pulse-Induced Filaments," Phys. Rev. Lett. **105**, 215005 (2010).

Bibliography

[1] J. D. Jackson, *Classical Electrodynamics* (John Wiley & Sons, New York, 1998), 3rd ed.

[2] P. N. Butcher and D. Cotter, *The Elements of Nonlinear Optics* (Cambridge University Press, 1990).

[3] H. Bach and N. Neuroth, eds., *The Properties of Optical Glass* (Springer Verlag, 1998).

[4] R. W. Boyd, *Nonlinear Optics* (Academic Press, San Diego, 1992).

[5] T. H. Maiman, "Stimulated Optical Radiation in Ruby," Nature **187**, 493–494 (1960).

[6] P. A. Franken, A. E. Hill, C. W. Peters, and G. Weinreich, "Generation of Optical Harmonics," Phys. Rev. Lett. **7**, 118–119 (1961).

[7] W. Kaiser and C. G. B. Garrett, "Two-Photon Excitation in CaF_2:Eu^{2+}," Phys. Rev. Lett. **7**, 229–231 (1961).

[8] J. Armstrong, N. Bloembergen, J. Ducuing, and P. Pershan, "Interactions between Light Waves in a Nonlinear Dielectric," Phys. Rev. **127**, 1918–1939 (1962).

[9] K. Tominaga and K. Yoshihara, "Fifth Order Optical Response of Liquid CS_2 Observed by Ultrafast Nonresonant Six-Wave Mixing," Phys. Rev. Lett. **74**, 3061–3064 (1995).

[10] J. A. Giordmaine and R. C. Miller, "Tunable Coherent Parametric Oscillation in $LiNbO_3$ at Optical Frequencies," Phys. Rev. Lett. **14**, 973–976 (1965).

[11] C. C. Wang and G. W. Racette, "Measurement of Parametric Gain Accompanying Optical Difference Frequency Generation," Appl. Phys. Lett. **6**, 169–171 (1965).

[12] D. C. Burnham and D. L. Weinberg, "Observation of Simultaneity in Parametric Production of Optical Photon Pairs," Phys. Rev. Lett. **25**, 84–87 (1970).

[13] D. Bouwmeester, J.-W. Pan, K. Mattle, M. Eibl, H. Weinfurter, and A. Zeilinger, "Experimental quantum teleportation," Nature **390**, 575–579 (1997).

[14] M. Bass, P. A. Franken, J. F. Ward, and G. Weinreich, "Optical Rectification," Phys. Rev. Lett. **9**, 446–448 (1962).

[15] L. Xu, X.-C. Zhang, and D. H. Auston, "Terahertz beam generation by femtosecond optical pulses in electro-optic materials," Appl. Phys. Lett. **61**, 1784–1786 (1992).

[16] Y. R. Shen, *The Principles of Nonlinear Optics* (John Wiley & Sons, New York, 1984).

[17] A. Yariv and D. M. Pepper, "Amplified reflection, phase conjugation, and oscillation in degenerate four-wave mixing," Opt. Lett. **1**, 16–18 (1977).

[18] D. E. Spence, P. N. Kean, and W. Sibbett, "60-fsec pulse generation from a self-mode-locked Ti:sapphire laser," Opt. Lett. **16**, 42–44 (1991).

[19] J. H. Marburger, "Self-focusing: Theory," Prog. Quantum Electron. **4**, 35–110 (1975).

[20] R. Y. Chiao, E. Garmire, and C. H. Townes, "Self-Trapping of Optical Beams," Phys. Rev. Lett. **13**, 479–482 (1964).

[21] M. Hercher, "Laser-induced damage in transparent media," J. Opt. Soc. Am. **54**, 563 (1964).

[22] E. Garmire, R. Y. Chiao, and C. H. Townes, "Dynamics and Characteristics of the Self-Trapping of Intense Light Beams," Phys. Rev. Lett. **16**, 347–349 (1966).

[23] A. Braun, G. Korn, X. Liu, D. Du, J. Squier, and G. Mourou, "Self-channeling of high-peak-power femtosecond laser pulses in air," Opt. Lett. **20**, 73–75 (1995).

[24] T. Brabec and F. Krausz, "Intense few-cycle laser fields: Frontiers of nonlinear optics," Rev. Mod. Phys. **72**, 545–591 (2000).

[25] Th. Fennel, K.-H. Meiwes-Broer, J. Tiggesbäumker, P.-G. Reinhard, P. M. Dinh, and E. Suraud, "Laser-driven nonlinear cluster dynamics," Rev. Mod. Phys. **82**, 1793–1842 (2010).

[26] D. L. Matthews, P. L. Hagelstein, M. D. Rosen, M. J. Eckart, N. M. Ceglio, A. U. Hazi, H. Medecki, B. J. MacGowan, J. E. Trebes, B. L. Whitten, E. M. Campbell, C. W. Hatcher, A. M. Hawryluk, R. L. Kauffman, L. D. Pleasance, G. Rambach, J. H. Scofield, G. Stone, and T. A. Weaver, "Demonstration of a Soft X-Ray Amplifier," Phys. Rev. Lett. **54**, 110–113 (1985).

[27] S. Suckewer, C. H. Skinner, H. Milchberg, C. Keane, and D. Voorhees, "Amplification of stimulated soft x-ray emission in a confined plasma column," Phys. Rev. Lett. **55**, 1753–1756 (1985).

[28] B. E. Lemoff, G. Y. Yin, C. L. Gordon, C. P. J. Barty, and S. E. Harris, "Demonstration of a 10-Hz Femtosecond-Pulse-Driven XUV Laser at 41.8 nm in Xe IX," Phys. Rev. Lett. **74**, 1574–1577 (1995).

[29] S. C. Wilks, J. M. Dawson, and W. B. Mori, "Frequency Up-Conversion of Electromagnetic Radiation with Use of an Overdense Plasma," Phys. Rev. Lett. **61**, 337–340 (1988).

[30] R. Rankin, C. E. Capjack, N. H. Burnett, and P. B. Corkum, "Refraction effects associated with multiphoton ionization and ultrashort-pulse laser propagation in plasma waveguides," Opt. Lett. **16**, 835–837 (1991).

[31] T. Ditmire, "Simulations of heating and electron energy distributions in optical field ionized plasmas," Phys. Rev. E **54**, 6735–6740 (1996).

[32] J. D. Huba, "NRL Plasma Formulary," Naval Research Laboratory, Washington, D.C. (2006).

[33] L. V. Keldysh, "Ionization in the field of a strong electromagnetic wave," Sov. Phys. JETP **20**, 1307–1314 (1965).

[34] R. C. Weast, ed., *Handbook of Chemistry and Physics* (CRC Press, 1987).

[35] M. V. Ammosov, N. B. Delone, and V. P. Krainov, "Tunnel ionization of complex atoms and of atomic ions in an alternating electromagnetic field," Sov. Phys. JETP **64**, 1191–1194 (1986).

[36] S. C. Rae and K. Burnett, "Detailed simulations of plasma-induced spectral blueshifting," Phys. Rev. A **46**, 1084–1090 (1992).

[37] M. D. Perry, O. L. Landen, A. Szöke, and E. M. Campbell, "Multiphoton ionization of the noble gases by an intense 10^{14}-W/cm^2 dye laser," Phys. Rev. A **37**, 747–760 (1988).

[38] N. B. Delone and V. P. Krainov, *Multiphoton Processes in Atoms* (Springer-Verlag, Berlin, 1993).

[39] Y.-H. Chuang, L. Zheng, and D. D. Meyerhofer, "Propagation of light pulses in a chirped-pulse-amplification laser," IEEE J. Quantum Electron. **29**, 270–280 (1993).

[40] M. D. Perry, T. Ditmire, and B. C. Stuart, "Self-phase modulation in chirped-pulse amplification," Opt. Lett. **19**, 2149–2151 (1994).

[41] A. Brodeur and S. L. Chin, "Ultrafast white-light continuum generation and self-focusing in transparent condensed media," J. Opt. Soc. Am. B **16**, 637–650 (1999).

[42] M. A. Duguay and J. W. Hansen, "An ultrafast light gate," Appl. Phys. Lett. **15**, 192–194 (1969).

[43] N. J. Halas, D. Krökel, and D. Grischkowsky, "Ultrafast light-controlled optical-fiber modulator," Appl. Phys. Lett. **50**, 886 (1987).

[44] L. Wang, P. P. Ho, C. Liu, G. Zhang, and R. R. Alfano, “Ballistic 2-D Imaging Through Scattering Walls Using an Ultrafast Optical Kerr Gate,” Science **253**, 769–771 (1991).

[45] J. Takeda, K. Nakajima, S. Kurita, S. Tomimoto, S. Saito, and T. Suemoto, “Time-resolved luminescence spectroscopy by the optical Kerr-gate method applicable to ultrafast relaxation processes,” Phys. Rev. B **62**, 10083–10087 (2000).

[46] D. Homoelle, A. L. Gaeta, V. Yanovsky, and G. Mourou, “Pulse contrast enhancement of high-energy pulses by use of a gas-filled hollow waveguide,” Opt. Lett. **27**, 1646–1648 (2002).

[47] L. F. Mollenauer, R. H. Stolen, and J. P. Gordon, “Experimental Observation of Picosecond Pulse Narrowing and Solitons in Optical Fibers,” Phys. Rev. Lett. **45**, 1095–1098 (1980).

[48] T. Tajima and J. M. Dawson, “Laser Electron Accelerator,” Phys. Rev. Lett. **43**, 267–270 (1979).

[49] N. E. Andreev, L. M. Gorbunov, V. I. Kirsanov, A. A. Pogosova, and R. R. Ramazashvili, “Resonant excitation of wakefields by a laser pulse in a plasma,” JETP Lett. **55**, 571–576 (1992).

[50] P. D. Maker, R. W. Terhune, and C. M. Savage, “Intensity-Dependent Changes in the Refractive Index of Liquids,” Phys. Rev. Lett. **12**, 507–509 (1964).

[51] R. W. Hellwarth, A. Owyoung, and N. George, “Origin of the Nonlinear Refractive Index of Liquid CCl_4,” Phys. Rev. A **4**, 2342–2347 (1971).

[52] A. Owyoung, “Ellipse rotation studies in laser host materials,” IEEE J. Quantum Electron. **9**, 1064–1069 (1973).

[53] P. W. Smith, W. J. Tomlinson, D. J. Eilenberger, and P. J. Maloney, “Measurement of electronic optical Kerr coefficients,” Opt. Lett. **6**, 581–583 (1981).

[54] S. Friberg and P. Smith, “Nonlinear optical glasses for ultrafast optical switches,” IEEE J. Quantum Electron. **23**, 2089–2094 (1987).

[55] R. Adair, L. L. Chase, and S. A. Payne, “Nonlinear refractive-index measurements of glasses using three-wave frequency mixing,” J. Opt. Soc. Am. B **4**, 875–881 (1987).

[56] R. Adair, L. L. Chase, and S. A. Payne, “Nonlinear refractive index of optical crystals,” Phys. Rev. B **39**, 3337–3350 (1989).

[57] M. J. Shaw, C. J. Hooker, and D. C. Wilson, “Measurement of the nonlinear refractive index of air and other gases at 248 nm,” Opt. Commun. **103**, 153–160 (1993).

[58] E. T. J. Nibbering, M. A. Franco, B. S. Prade, G. Grillon, C. Le Blanc, and A. Mysyrowicz, "Measurement of the nonlinear refractive index of transparent materials by spectral analysis after nonlinear propagation," Opt. Commun. **119**, 479–484 (1995).

[59] M. Sheik-Bahae, A. A. Said, T.-H. Wei, D. J. Hagan, and E. W. Van Stryland, "Sensitive measurement of optical nonlinearities using a single beam," IEEE J. Quantum Electron. **26**, 760–769 (1990).

[60] D. Cotter, C. N. Ironside, B. J. Ainslie, and H. P. Girdlestone, "Picosecond pump-probe interferometric measurement of optical nonlinearity in semiconductor-doped fibers," Opt. Lett. **14**, 317–319 (1989).

[61] T. Hattori, H. Okawa, T. Wada, and H. Sasabe, "Subpicosecond interferometric measurement of the nonlinear refractive index of poly(3-hexylthiophene)," Opt. Lett. **17**, 1560–1562 (1992).

[62] Cl. Froehly, A. Lacourt, and J. Ch. Vienot, "Time impulse response and time frequency response of optical pupils.: Experimental confirmations and applications," Nouvelle Revue d'Optique **4**, 183–196 (1973).

[63] E. Tokunaga, A. Terasaki, and T. Kobayashi, "Frequency-domain interferometer for femtosecond time-resolved phase spectroscopy," Opt. Lett. **17**, 1131–1133 (1992).

[64] F. Reynaud, F. Salin, and A. Barthelemy, "Measurement of phase shifts introduced by nonlinear optical phenomena on subpicosecond pulses," Opt. Lett. **14**, 275–277 (1989).

[65] C. X. Yu, M. Margalit, E. P. Ippen, and H. A. Haus, "Direct measurement of self-phase shift due to fiber nonlinearity," Opt. Lett. **23**, 679–681 (1998).

[66] J. P. Geindre, P. Audebert, A. Rousse, F. Falliès, J. C. Gauthier, A. Mysyrowicz, A. D. Santos, G. Hamoniaux, and A. Antonetti, "Frequency-domain interferometer for measuring the phase and amplitude of a femtosecond pulse probing a laser-produced plasma," Opt. Lett. **19**, 1997–1999 (1994).

[67] P. Salières, L. Le Déroff, T. Auguste, P. Monot, P. d'Oliveira, D. Campo, J.-F. Hergott, H. Merdji, and B. Carré, "Frequency-Domain Interferometry in the XUV with High-Order Harmonics," Phys. Rev. Lett. **83**, 5483–5486 (1999).

[68] R. Evans, A. D. Badger, F. Falliès, M. Mahdieh, T. A. Hall, P. Audebert, J.-P. Geindre, J.-C. Gauthier, A. Mysyrowicz, G. Grillon, and A. Antonetti, "Time- and Space-Resolved Optical Probing of Femtosecond-Laser-Driven Shock Waves in Aluminum," Phys. Rev. Lett. **77**, 3359–3362 (1996).

[69] K. Y. Kim, I. Alexeev, E. Parra, and H. M. Milchberg, "Time-Resolved Explosion of Intense-Laser-Heated Clusters," Phys. Rev. Lett. **90**, 023401 (2003).

[70] J. R. Marquès, J. P. Geindre, F. Amiranoff, P. Audebert, J. C. Gauthier, A. Antonetti, and G. Grillon, "Temporal and Spatial Measurements of the Electron Density Perturbation Produced in the Wake of an Ultrashort Laser Pulse," Phys. Rev. Lett. **76**, 3566–3569 (1996).

[71] C. W. Siders, S. P. Le Blanc, D. Fisher, T. Tajima, M. C. Downer, A. Babine, A. Stepanov, and A. Sergeev, "Laser Wakefield Excitation and Measurement by Femtosecond Longitudinal Interferometry," Phys. Rev. Lett. **76**, 3570–3573 (1996).

[72] J. R. Marquès, F. Dorchies, F. Amiranoff, P. Audebert, J. C. Gauthier, J. P. Geindre, A. Antonetti, T. M. Antonsen, P. Chessa, and P. Mora, "Laser wakefield: Experimental study of nonlinear radial electron oscillations," Phys. Plasmas **5**, 1162 (1998).

[73] M. Takeda, H. Ina, and S. Kobayashi, "Fourier-transform method of fringe-pattern analysis for computer-based topography and interferometry," J. Opt. Soc. Am. **72**, 156–160 (1982).

[74] A. Benuzzi-Mounaix, M. Koenig, J. M. Boudenne, T. A. Hall, D. Batani, F. Scianitti, A. Masini, and D. Di Santo, "Chirped pulse reflectivity and frequency domain interferometry in laser driven shock experiments," Phys. Rev. E **60**, R2488–R2491 (1999).

[75] C. Y. Chien, B. La Fontaine, A. Desparois, Z. Jiang, T. W. Johnston, J. C. Kieffer, H. Pépin, F. Vidal, and H. P. Mercure, "Single-shot chirped-pulse spectral interferometry used to measure the femtosecond ionization dynamics of air," Opt. Lett. **25**, 578–580 (2000).

[76] J.-P. Geindre, P. Audebert, S. Rebibo, and J.-C. Gauthier, "Single-shot spectral interferometry with chirped pulses," Opt. Lett. **26**, 1612–1614 (2001).

[77] S. P. Le Blanc, E. W. Gaul, N. H. Matlis, A. Rundquist, and M. C. Downer, "Single-shot measurement of temporal phase shifts by frequency-domain holography," Opt. Lett. **25**, 764–766 (2000).

[78] K. Y. Kim, I. Alexeev, and H. M. Milchberg, "Single-shot supercontinuum spectral interferometry," Appl. Phys. Lett. **81**, 4124 (2002).

[79] K. Y. Kim, I. Alexeev, and H. Milchberg, "Single-shot measurement of laser-induced double step ionization of helium," Opt. Express **10**, 1563–1572 (2002).

[80] K. Y. Kim, I. Alexeev, V. Kumarappan, E. Parra, T. Antonsen, T. Taguchi, A. Gupta, and H. M. Milchberg, "Gases of exploding laser-heated cluster nanoplasmas as a nonlinear optical medium," Phys. Plasmas **11**, 2882–2889 (2004).

[81] K. Y. Kim, I. Alexeev, and H. M. Milchberg, "Measurement of ultrafast dynamics in the interaction of intense laser pulses with gases, clusters, and plasma waveguides," Phys. Plasmas **12**, 056712 (2005).

[82] N. H. Matlis, S. Reed, S. S. Bulanov, V. Chvykov, G. Kalintchenko, T. Matsuoka, P. Rousseau, V. Yanovsky, A. Maksimchuk, S. Kalmykov, G. Shvets, and M. C. Downer, "Snapshots of laser wakefields," Nature Phys. **2**, 749–753 (2006).

[83] J. K. Ranka, R. S. Windeler, and A. J. Stentz, "Visible continuum generation in air-silica microstructure optical fibers with anomalous dispersion at 800 nm," Opt. Lett. **25**, 25–27 (2000).

[84] J. M. Dudley, G. Genty, and S. Coen, "Supercontinuum generation in photonic crystal fiber," Rev. Mod. Phys. **78**, 1135–1184 (2006).

[85] P. B. Corkum, C. Rolland, and T. Srinivasan-Rao, "Supercontinuum Generation in Gases," Phys. Rev. Lett. **57**, 2268–2271 (1986).

[86] P. O'Shea, M. Kimmel, X. Gu, and R. Trebino, "Highly simplified device for ultrashort-pulse measurement," Opt. Lett. **26**, 932–934 (2001).

[87] S. Augst, A. Talebpour, S. L. Chin, Y. Beaudoin, and M. Chaker, "Nonsequential triple ionization of argon atoms in a high-intensity laser field," Phys. Rev. A **52**, R917–R919 (1995).

[88] H. Lehmeier, W. Leupacher, and A. Penzkofer, "Nonresonant third order hyperpolarizability of rare gases and N_2 determined by third harmonic generation," Opt. Commun. **56**, 67–72 (1985).

[89] B. Friedrich and D. Herschbach, "Alignment and Trapping of Molecules in Intense Laser Fields," Phys. Rev. Lett. **74**, 4623–4626 (1995).

[90] J.-F. Ripoche, G. Grillon, B. Prade, M. Franco, E. Nibbering, R. Lange, and A. Mysyrowicz, "Determination of the time dependence of n_2 in air," Opt. Commun. **135**, 310–314 (1997).

[91] S. De, I. Znakovskaya, D. Ray, F. Anis, N. G. Johnson, I. A. Bocharova, M. Magrakvelidze, B. D. Esry, C. L. Cocke, I. V. Litvinyuk, and M. F. Kling, "Field-Free Orientation of CO Molecules by Femtosecond Two-Color Laser Fields," Phys. Rev. Lett. **103**, 153002 (2009).

[92] A. Ashkin and J. M. Dziedzic, "Optical trapping and manipulation of viruses and bacteria," Science **235**, 1517–1520 (1987).

[93] E. L. Raab, M. Prentiss, A. Cable, S. Chu, and D. E. Pritchard, "Trapping of Neutral Sodium Atoms with Radiation Pressure," Phys. Rev. Lett. **59**, 2631–2634 (1987).

[94] P. D. Lett, W. D. Phillips, S. L. Rolston, C. E. Tanner, R. N. Watts, and C. I. Westbrook, “Optical molasses,” J. Opt. Soc. Am. B **6**, 2084–2107 (1989).

[95] H. Stapelfeldt and T. Seideman, “Colloquium: Aligning molecules with strong laser pulses,” Rev. Mod. Phys. **75**, 543–557 (2003).

[96] R. N. Zare, “Laser Control of Chemical Reactions,” Science **279**, 1875–1879 (1998).

[97] I. V. Litvinyuk, K. F. Lee, P. W. Dooley, D. M. Rayner, D. M. Villeneuve, and P. B. Corkum, “Alignment-Dependent Strong Field Ionization of Molecules,” Phys. Rev. Lett. **90**, 233003 (2003).

[98] R. Velotta, N. Hay, M. B. Mason, M. Castillejo, and J. P. Marangos, “High-Order Harmonic Generation in Aligned Molecules,” Phys. Rev. Lett. **87**, 183901 (2001).

[99] T. Kanai, S. Minemoto, and H. Sakai, “Quantum interference during high-order harmonic generation from aligned molecules,” Nature **435**, 470–474 (2005).

[100] J. Itatani, J. Levesque, D. Zeidler, H. Niikura, H. Pépin, J. C. Kieffer, P. B. Corkum, and D. M. Villeneuve, “Tomographic imaging of molecular orbitals,” Nature **432**, 867–871 (2004).

[101] G. Sansone, F. Kelkensberg, J. F. Pérez-Torres, F. Morales, M. F. Kling, W. Siu, O. Ghafur, P. Johnsson, M. Swoboda, E. Benedetti, F. Ferrari, F. Lépine, J. L. Sanz-Vicario, S. Zherebtsov, I. Znakovskaya, A. L’Huillier, Ivanov, M. Nisoli, F. Martín, and M. J. J. Vrakking, “Electron localization following attosecond molecular photoionization,” Nature **465**, 763–766 (2010).

[102] J. J. Sakurai, *Modern Quantum Mechanics* (Addison-Wesley, 1994).

[103] E. Merzbacher, *Quantum Mechanics* (John Wiley & Sons, New York, 1998), 3rd ed.

[104] H. Harde and D. Grischkowsky, “Coherent transients excited by subpicosecond pulses of terahertz radiation,” J. Opt. Soc. Am. B **8**, 1642–1651 (1991).

[105] C. H. Townes and A. L. Schawlow, *Microwave Spectroscopy* (McGraw-Hill, New York, 1955).

[106] O. Ghafur, A. Rouzée, A. Gijsbertsen, W. K. Siu, S. Stolte, and M. J. J. Vrakking, “Impulsive orientation and alignment of quantum-state-selected NO molecules,” Nature Phys. **5**, 289–293 (2009).

[107] D. A. McQuarrie, *Statistical Mechanics* (Harper Collins, New York, 1976).

[108] A. J. C. Varandas and Z. R. Xu, “Permutational Symmetry and the Role of Nuclear Spin in the Vibrational Spectra of Molecules in Doubly Degenerate Electronic States: The Trimers of ^{2}S Atoms,” in “The Role of Degenerate States in Chemistry,” , vol. 124, M. Baer and G. D. Billing, eds. (John Wiley & Sons, Inc., 2003), pp. 659–741.

[109] C. H. Lin, J. P. Heritage, T. K. Gustafson, R. Y. Chiao, and J. P. McTague, “Birefringence arising from the reorientation of the polarizability anisotropy of molecules in collisionless gases,” Phys. Rev. A **13**, 813–829 (1976).

[110] R. A. Bartels, T. C. Weinacht, N. Wagner, M. Baertschy, C. H. Greene, M. M. Murnane, and H. C. Kapteyn, “Phase Modulation of Ultrashort Light Pulses using Molecular Rotational Wave Packets,” Phys. Rev. Lett. **88**, 013903 (2001).

[111] F. Calegari, C. Vozzi, S. Gasilov, E. Benedetti, G. Sansone, M. Nisoli, S. De Silvestri, and S. Stagira, “Rotational Raman Effects in the Wake of Optical Filamentation,” Phys. Rev. Lett. **100**, 123006 (2008).

[112] S. Varma, Y.-H. Chen, and H. M. Milchberg, “Trapping and Destruction of Long-Range High-Intensity Optical Filaments by Molecular Quantum Wakes in Air,” Phys. Rev. Lett. **101**, 205001 (2008).

[113] J. Wu, H. Cai, Y. Peng, and H. Zeng, “Controllable supercontinuum generation by the quantum wake of molecular alignment,” Phys. Rev. A **79**, 041404 (2009).

[114] P. W. Dooley, I. V. Litvinyuk, K. F. Lee, D. M. Rayner, M. Spanner, D. M. Villeneuve, and P. B. Corkum, “Direct imaging of rotational wave-packet dynamics of diatomic molecules,” Phys. Rev. A **68**, 023406 (2003).

[115] F. Rosca-Pruna and M. J. J. Vrakking, “Experimental Observation of Revival Structures in Picosecond Laser-Induced Alignment of I_2,” Phys. Rev. Lett. **87**, 153902 (2001).

[116] E. P. Ippen and C. V. Shank, “Picosecond response of a high-repetition-rate CS_2 optical Kerr gate,” Appl. Phys. Lett. **26**, 92–93 (1975).

[117] J. P. Heritage, T. K. Gustafson, and C. H. Lin, “Observation of Coherent Transient Birefringence in CS_2 Vapor,” Phys. Rev. Lett. **34**, 1299–1302 (1975).

[118] R. Righini, “Ultrafast Optical Kerr Effect in Liquids and Solids,” Science **262**, 1386–1390 (1993).

[119] V. Renard, O. Faucher, and B. Lavorel, “Measurement of laser-induced alignment of moleculesby cross defocusing,” Opt. Lett. **30**, 70–72 (2005).

[120] V. Loriot, E. Hertz, A. Rouzée, B. Sinardet, B. Lavorel, and O. Faucher, "Strong-field molecular ionization: determination of ionization probabilities calibrated with field-free alignment," Opt. Lett. **31**, 2897–2899 (2006).

[121] I. V. Fedotov, A. D. Savvin, A. B. Fedotov, and A. M. Zheltikov, "Controlled rotational Raman echo recurrences and modulation of high-intensity ultrashort laser pulses by molecular rotations in the gas phase," Opt. Lett. **32**, 1275–1277 (2007).

[122] S. B. Howell, *Handbook of CCD Astronomy* (Cambridge University Press, 2006), 2nd ed.

[123] E. T. J. Nibbering, G. Grillon, M. A. Franco, B. S. Prade, and A. Mysyrowicz, "Determination of the inertial contribution to the nonlinear refractive index of air, N_2, and O_2 by use of unfocused high-intensity femtosecond laser pulses," J. Opt. Soc. Am. B **14**, 650–660 (1997).

[124] J. R. Peñano, P. Sprangle, P. Serafim, B. Hafizi, and A. Ting, "Stimulated Raman scattering of intense laser pulses in air," Phys. Rev. E **68**, 056502 (2003).

[125] I. Alexeev, A. Ting, D. F. Gordon, E. Briscoe, J. R. Penano, R. F. Hubbard, and P. Sprangle, "Longitudinal compression of short laser pulses in air," Appl. Phys. Lett. **84**, 4080–4082 (2004).

[126] K. F. Lee, F. Légaré, D. M. Villeneuve, and P. B. Corkum, "Measured field-free alignment of deuterium by few-cycle pulses," J. Phys. B: At. Mol. Opt. Phys. **39**, 4081–4086 (2006).

[127] G. N. Steinberg, "Filamentary Tracks Formed in Transparent Optical Glass by Laser Beam Self-Focusing. I. Experimental Investigation," Phys. Rev. A **4**, 1182–1194 (1971).

[128] C. R. Giuliano and J. H. Marburger, "Observations of Moving Self-Foci in Sapphire," Phys. Rev. Lett. **27**, 905–908 (1971).

[129] S. L. Chin, S. A. Hosseini, W. Liu, Q. Luo, F. Théberge, N. Aközbek, A. Becker, V. P. Kandidov, O. G. Kosareva, and H. Schroeder, "The propagation of powerful femtosecond laser pulses in opticalmedia: physics, applications, and new challenges," Can. J. Phys. **83**, 863–905 (2005).

[130] A. Couairon and A. Mysyrowicz, "Femtosecond filamentation in transparent media," Phys. Rep. **441**, 47–189 (2007).

[131] L. Bergé, S. Skupin, R. Nuter, J. Kasparian, and J.-P. Wolf, "Ultrashort filaments of light in weakly ionized, optically transparent media," Rep. Prog. Phys. **70**, 1633–1713 (2007).

[132] J. Kasparian, M. Rodriguez, G. Méjean, J. Yu, E. Salmon, H. Wille, R. Bourayou, S. Frey, Y.-B. André, A. Mysyrowicz, R. Sauerbrey, J.-P. Wolf, and L. Wöste, "White-Light Filaments for Atmospheric Analysis," Science **301**, 61–64 (2003).

[133] V. P. Kandidov, O. G. Kosareva, I. S. Golubtsov, W. Liu, A. Becker, N. Akozbek, C. M. Bowden, and S. L. Chin, "Self-transformation of a powerful femtosecond laser pulse into a white-light laser pulse in bulk optical media (or supercontinuum generation)," Appl. Phys. B **77**, 149–165 (2003).

[134] O. Varela, B. Alonso, I. J. Sola, J. San Román, A. Zaïr, C. Méndez, and L. Roso, "Self-compression controlled by the chirp of the input pulse," Opt. Lett. **35**, 3649–3651 (2010).

[135] S. Tzortzakis, G. Méchain, G. Patalano, Y.-B. André, B. Prade, M. Franco, A. Mysyrowicz, J.-M. Munier, M. Gheudin, G. Beaudin, and P. Encrenaz, "Coherent subterahertz radiation from femtosecond infrared filaments in air," Opt. Lett. **27**, 1944–1946 (2002).

[136] C. D'Amico, A. Houard, M. Franco, B. Prade, A. Mysyrowicz, A. Couairon, and V. T. Tikhonchuk, "Conical Forward THz Emission from Femtosecond-Laser-Beam Filamentation in Air," Phys. Rev. Lett. **98**, 235002 (2007).

[137] X. M. Zhao, J.-C. Diels, C. Y. Wang, and J. M. Elizondo, "Femtosecond ultraviolet laser pulse induced lightning discharges in gases," IEEE J. Quantum Electron. **31**, 599–612 (1995).

[138] M. Rodriguez, R. Sauerbrey, H. Wille, L. Wöste, T. Fujii, Y.-B. André, A. Mysyrowicz, L. Klingbeil, K. Rethmeier, W. Kalkner, J. Kasparian, E. Salmon, J. Yu, and J.-P. Wolf, "Triggering and guiding megavolt discharges by use of laser-induced ionized filaments," Opt. Lett. **27**, 772–774 (2002).

[139] D. Strickland and P. B. Corkum, "Resistance of short pulses to self-focusing," J. Opt. Soc. Am. B **11**, 492–497 (1994).

[140] A. Brodeur, C. Y. Chien, F. A. Ilkov, S. L. Chin, O. G. Kosareva, and V. P. Kandidov, "Moving focus in the propagation of ultrashort laser pulses in air," Opt. Lett. **22**, 304–306 (1997).

[141] E. T. J. Nibbering, P. F. Curley, G. Grillon, B. S. Prade, M. A. Franco, F. Salin, and A. Mysyrowicz, "Conical emission from self-guided femtosecond pulses in air," Opt. Lett. **21**, 62–65 (1996).

[142] A. Becker, N. Aközbek, K. Vijayalakshmi, E. Oral, C. M. Bowden, and S. L. Chin, "Intensity clamping and re-focusing of intense femtosecond laser pulses in nitrogen molecular gas," Appl. Phys. B **73**, 287–290 (2001).

[143] W. Liu, S. Petit, A. Becker, N. Aközbek, C. M. Bowden, and S. L. Chin, "Intensity clamping of a femtosecond laser pulse in condensed matter," Opt. Commun. **202**, 189–197 (2002).

[144] W. Liu, J.-F. Gravel, F. Théberge, A. Becker, and S. L. Chin, "Background reservoir: its crucial role for long-distance propagation of femtosecond laser pulses in air," Appl. Phys. B **80**, 857–860 (2005).

[145] M. Mlejnek, E. M. Wright, and J. V. Moloney, "Dynamic spatial replenishment of femtosecond pulses propagating in air," Opt. Lett. **23**, 382–384 (1998).

[146] A. Couairon and L. Bergé, "Modeling the filamentation of ultra-short pulses in ionizing media," Phys. Plasmas **7**, 193–209 (2000).

[147] J. Wu and T. M. Antonsen, "Laser pulse splitting and trapping in tenuous gases," Phys. Plasmas **10**, 2254–2266 (2003).

[148] F. Théberge, W. Liu, P. Tr. Simard, A. Becker, and S. L. Chin, "Plasma density inside a femtosecond laser filament in air: Strong dependence on external focusing," Phys. Rev. E **74**, 036406 (2006).

[149] S. Eisenmann, A. Pukhov, and A. Zigler, "Fine Structure of a Laser-Plasma Filament in Air," Phys. Rev. Lett. **98**, 155002 (2007).

[150] J. Bernhardt, W. Liu, F. Théberge, H. L. Xu, J. F. Daigle, M. Châteauneuf, J. Dubois, and S. L. Chin, "Spectroscopic analysis of femtosecond laser plasma filament in air," Opt. Commun. **281**, 1268–1274 (2008).

[151] B. La Fontaine, F. Vidal, Z. Jiang, C. Y. Chien, D. Comtois, A. Desparois, T. W. Johnston, J.-C. Kieffer, H. Pépin, and H. P. Mercure, "Filamentation of ultrashort pulse laser beams resulting from their propagation over long distances in air," Phys. Plasmas **6**, 1615–1621 (1999).

[152] S. Tzortzakis, B. Prade, M. Franco, and A. Mysyrowicz, "Time-evolution of the plasma channel at the trail of a self-guided IR femtosecond laser pulse in air," Opt. Commun. **181**, 123–127 (2000).

[153] G. Rodriguez, A. R. Valenzuela, B. Yellampalle, M. J. Schmitt, and K.-Y. Kim, "In-line holographic imaging and electron density extraction of ultrafast ionized air filaments," J. Opt. Soc. Am. B **25**, 1988–1997 (2008).

[154] R. P. Fischer, A. C. Ting, D. F. Gordon, R. F. Fernsler, G. P. DiComo, and P. Sprangle, "Conductivity Measurements of Femtosecond Laser-Plasma Filaments," IEEE Trans. Plasma Sci. **35**, 1430–1436 (2007).

[155] P. Sprangle, J. R. Peñano, and B. Hafizi, "Propagation of intense short laser pulses in the atmosphere," Phys. Rev. E **66**, 046418 (2002).

[156] W. Liu and S. Chin, "Direct measurement of the critical power of femtosecond Ti:sapphire laser pulse in air," Opt. Express **13**, 5750–5755 (2005).

[157] D. F. Gordon, A. C. Ting, I. Alexeev, R. P. Fischer, and P. Sprangle, "Direct measurements of the dynamics of self-guided femtosecond laser filaments in air," IEEE Trans. Plasma Sci. **34**, 249–253 (2006).

[158] T. R. Clark and H. M. Milchberg, "Time- and Space-Resolved Density Evolution of the Plasma Waveguide," Phys. Rev. Lett. **78**, 2373–2376 (1997).

[159] S.-Y. Chen, G. S. Sarkisov, A. Maksimchuk, R. Wagner, and D. Umstadter, "Evolution of a Plasma Waveguide Created during Relativistic-Ponderomotive Self-Channeling of an Intense Laser Pulse," Phys. Rev. Lett. **80**, 2610–2613 (1998).

[160] M. Kalal and K. A. Nugent, "Abel inversion using fast Fourier transforms," Appl. Opt. **27**, 1956–1959 (1988).

[161] R. J. Goldston and P. H. Rutherford, *Introduction to Plasma Physics* (Institute of Physics Publishing, Bristol, 1995).

[162] P. Mora and T. M. Antonsen, "Kinetic modeling of intense, short laser pulses propagating in tenuous plasmas," Phys. Plasmas **4**, 217 (1997).

[163] A. Talebpour, J. Yang, and S. L. Chin, "Semi-empirical model for the rate of tunnel ionization of N_2 and O_2 molecule in an intense Ti:sapphire laser pulse," Opt. Commun. **163**, 29–32 (1999).

[164] J. P. Cryan, P. H. Bucksbaum, and R. N. Coffee, "Field-free alignment in repetitively kicked nitrogen gas," Phys. Rev. A **80**, 063412 (2009).

[165] P. Béjot, J. Kasparian, S. Henin, V. Loriot, T. Vieillard, E. Hertz, O. Faucher, B. Lavorel, and J.-P. Wolf, "Higher-Order Kerr Terms Allow Ionization-Free Filamentation in Gases," Phys. Rev. Lett. **104**, 103903 (2010).

[166] M. Kolesik, D. Mirell, J. C. Diels, and J. V. Moloney, "On the higher-order Kerr effect in femtosecond filaments," Opt. Lett. **35**, 3685 (2010).

[167] M. Kolesik, E. M. Wright, and J. V. Moloney, "Femtosecond filamentation in air and higher-order nonlinearities," Opt. Lett. **35**, 2550 (2010).

[168] A. Teleki, E. M. Wright, and M. Kolesik, "Microscopic model for the higher-order nonlinearity in optical filaments," Phys. Rev. A **82**, 065801 (2010).

[169] O. Kosareva, J.-F. Daigle, N. Panov, T. Wang, S. Hosseini, S. Yuan, G. Roy, V. Makarov, and S. Leang Chin, "Arrest of self-focusing collapse in femtosecond air filaments: higher order Kerr or plasma defocusing?" Opt. Lett. **36**, 1035 (2011).

[170] P. Polynkin, M. Kolesik, E. M. Wright, and J. V. Moloney, "Experimental Tests of the New Paradigm for Laser Filamentation in Gases," Phys. Rev. Lett. **106**, 153902 (2011).

[171] V. Loriot, E. Hertz, O. Faucher, and B. Lavorel, "Measurement of high order Kerr refractive index of major air components," Opt. Express **17**, 13429 (2009).